

Dissertation
submitted to the
Combined Faculties for the Natural Sciences and for Mathematics
of the Ruperto-Carola University of Heidelberg, Germany
for the degree of
Doctor of Natural Sciences

presented by
Diplom-Physiker Jürgen Sawinski
born in Leonberg, Germany
Oral examination: December 21st, 2005

Development of a head-mount fiber scanning system for imaging in vivo

Referees: Prof. Dr. Winfried Denk
Prof. Dr. Josef Bille

In dieser Arbeit werden die grundlegenden Konzepte beschrieben, die für die Messung von Nervensignalen mittels der Zwei-Photon Laser Scanning Mikroskopie und deren Miniaturisierung zur Messung von Nervenfunktionen in freilaufenden Tieren notwendig sind.

Besonders Augenmerk wird dabei auf die Konstruktion eines Lasers mit erhöhter Repetitionsrate und der Entwicklung einer neuartigen, nicht-resonanten Faser-Scan Technik gelegt.

Der Erhöhung der Wiederholrate des Lasers soll dabei unerwünschte Nichtlinearitäten bei der Übertragung mittels einer Einmoden-Faser verringern.

Durch den Einbau des nicht-resonanten Faser-Scanners in den Prototypen eines kopfgebundenen miniaturisierten Mikroskops wird dessen Eignung mittels fluoreszierender Proben demonstriert. Das Einsatzgebiet sollte sich dadurch nicht nur auf die Messung an freilaufenden Tieren beschränken sondern allgemein für mobile abbildende Methoden geeignet sein.

In this thesis I will describe the basic concepts necessary for acquiring functional data from nerve tissue by application of two-photon laser scanning microscopy and its miniaturization for in vivo imaging in freely moving animals.

The construction of a laser with enhanced repetition rate and the design of a novel non-resonant fiber scanning technique is emphasized.

The increased repetition rate of the femtosecond laser source should decrease undesirable non-linear effects when transmitting ultra-short pulses with a single mode fiber.

By implementing the prototype of a head-mounted microscope involving the novel fiber scanner and testing with fluorescent probes I can demonstrate its feasibility - not only for imaging in freely moving animals but for mobile laser scanning microscopy in general.

Development of a head-mount fiber scanning system for imaging in vivo

Jürgen Sawinski

November 7, 2005

ידוה

my
shelter and foothold

/me thanks

Mum, *you're the best*, and Dad, *I won't forget you*

my daughters

Marlene Hannah Stella and Charlotte Theresa Luna
and my wife Steffi

close friends

Alexander Gutleiderer, Maz (aka Mazahir T. Hasan), Robin M. Pankonin

"doctor father"

Winfried Denk

colleagues

Matthias Both, Delphine Débarre, Jens Dübel, Thomas Euler, Horatiu
Fantana, Marcus Feierabend, Rainer Friedrich, Günter Giese, Susanne
Hausselt, Manfred Hauswirth, Christa Hörner-Ehm, Ingo Janke, Marcel
Lauterbach, Heribert Lill, Andrea Migalla, Michael U. Müller, Markus
Rückel, Jürgen Tritthardt, Emre Yaksi, Herbert Zimmermann,

and

Paul French, Dr. Lina Machtoub, Barabara Panella, Bogdan Povh,
Dr. Jutta Steinhausen

as well as

Michael Riedel, Argillon GmbH, Germany
Dr. Michael Graf, Wellomer GmbH, Maxdorf–Germany
Stephan Laaber, CeramOptec, Bonn–Germany
Christine Kurth, Toray Deutschland GmbH, Neu-Isenburg–Germany
Mike Hackett, Industrial Fiber Optics, Tempe, Arizona–USA

and whoever I should have mentioned

Preface

The basic question in neuroscience research is: how does the brain encode sensory information and translate it into complex behavior.

In this thesis, I will describe a refined miniaturized two-photon imaging technique which would help to address questions relating to activity at the level of neuronal circuits in awake mammals. The present technique might also prove useful in applied human medicine where non-invasive detection methods are especially needed.

My thesis is divided into the following parts:

The introduction should give an overview of the developments and methods in the field of brain research and detection methods. I will also highlight new developments in two-photon based imaging, especially suitable for non-invasive imaging of neuronal activity and anatomy at the circuit level in awake mammals.

The first part is devoted to the design of a high-repetition rate Ti:sapphire mode-locked laser for efficient multi-photon excitation. Laser cavity design, dispersion and its compensation, fiber transmission and finally the practical building and results of the laser will be described and discussed in different chapters. The laser achieves high repetition rate (up to 270MHz) and sub-30fs pulses with pure prism based dispersion compensation.

The second part will be devoted to the design of a miniature head-mounted multi-photon laser scanning microscope using a newly developed non-resonant fiber scanner we termed “piezo lever fiber scanner” (PLFS). By multiple folding of the light path inside the microscope we have achieved a small and light-weight microscope that is suitable for imaging in freely moving animals. I will also show that the design has imaging properties similar to the standard two-photon microscope.

In the appendix, I have included additional information and programs, as well as constants used in the models.

Contents

1. Introduction	1
1.1. Technical approaches to brain research	1
1.2. Neurobiological foundations	3
1.3. Goals of this study	4
I. Light source development	6
2. Laser cavity design	7
2.1. ABCD-matrix notation	7
2.1.1. Formalism based on Gaussian beams	7
2.1.2. Cavity stability limits	9
2.2. Small signal mode variation	11
3. Dispersion and compensation	12
3.1. Dispersion in optical media	13
3.2. Ray-tracing fundamentals	14
3.3. Numerical calculation results	16
4. Tunable Ti:sapphire oscillator	19
4.1. Introduction	19
4.2. Design	21
4.2.1. Dispersion compensation	21
4.2.2. Cavity optimization	24
4.3. Cavity construction	24
4.3.1. Alignment	25
4.3.2. Prism sequence alignment	26
4.3.3. Mode locking	27
4.4. Results	28
4.5. Conclusions	29

II. Head-mount microscope	32
5. Piezo lever fiber scanner model	33
5.1. Bending of a beam	33
5.1.1. Bernoulli bending	33
5.1.2. Resonant limitation	36
5.2. Stress limits	37
5.2.1. Bending strength	37
5.2.2. Yield strength	38
5.2.3. Buckling	38
5.3. Piezo bending element	39
5.4. Scanner model	42
5.5. Results	45
6. A random access miniature fiber scanner	49
6.1. Introduction	49
6.2. Theoretical framework	50
6.2.1. Design and limitations of a piezoelectric scanner	50
6.2.2. Optical considerations	53
6.3. Materials and Methods	55
6.4. Results	58
6.5. Discussion	63
6.6. Conclusions	64
III. Appendix	66
A. Supplemental information	67
B. Material constants	71
C. Programs	73
C.1. Dispersion compensation	73
C.2. Cavity construction	82
C.3. Scanner model	102
Bibliography	109

1. Introduction

The research on the nervous system even in lower animals is accompanied with many different technical approaches. A coarse separation in which these techniques attack can be drawn in three groups (Geh [2004]):

(1) Large functionally grouped areas of the brain can be studied with methods like positron-electron tomography (PET), functional magnetic resonance imaging (fMRI), electro- and magnetoencephalography (EEG respective MEG).

(2) In neuronal populations (hundreds of cells), for example whisker-related barrel fields in rats, electrode and multi-electrode recording and optical imaging techniques are suitable methods for functional analysis.

(3) Cellular functions can be observed with single electrode recording and optical imaging (especially non-linear microscopy). In combination with activity sensors (synthetic dyes and genetically encoded sensors) very high spatial and temporal resolution activity signals and responses to sensory experience can be revealed.

The major goal of the present study is to improve miniaturized two-photon imaging methods for studying neuronal populations and single cells in behaving, i.e. unrestrained, mammals.

1.1. Technical approaches to brain research

Earlier studies were mainly focused on electrical signals in the nervous system. Though, the underlying signal transmission is inherently complex, early studies starting in the 17th century could demonstrate electrical signals by detection as well as stimulation.

Today, extracellular electrode recording techniques enables detection of accumulative electrical activity from several neighboring cells in living brain slices and in vivo. It is also possible to perform intracellular recordings from single neurons revealing fundamental insight on mechanisms of action potential initiation and propagation (Yuste and Tank [1996]). The development of the patch clamp technique (Sakmann and Neher [1984]) has further enabled measurements of activity in neuronal compartments or structures (such as soma or dendrites), even single receptors or channels in dendrites. Although the temporal resolution of these techniques is very high (sub-millisecond), they are blind to cellular structures, i.e. they do not provide structural information and commonly imaging techniques are used to identify the target. Furthermore, to target a specific cell or compartment, the risk of disrupting tissue is high, that means these methods are invasive.

Another class of detection methods is based on atomic and molecular properties. These are for example positron-electron tomography (PET) and functional magnetic resonance imaging (fMRI). While these methods are non-invasive their resolution is relatively low (commonly $> 1\text{ mm}$, $> 0.25\text{ s}$) and the measurement relies on secondary effects (magnetic properties of deoxygenated haemoglobin and differential blood flow, Truner and Jones [2003]).

Optical imaging methods basically record absorption, refraction, fluorescence including multi-photon absorption or other non-linear effects. A good example of the first two is the traditional microscope currently used in combination with advanced contrast techniques like differential interference contrast (DIC). These techniques, however, do not provide functional data and are rather used to identify structures in explanted tissue. In contrast, fluorescence and non-linear effects can be used with live cell imaging as various effects allow for functional analysis. It is, for example, possible to exploit endogenous cellular fluorescence (such as flavin proteins) or use external labels (such as fluorescent antibodies, calcium sensors, etc.). Also, illumination of cellular structures can generate complex non-linear effects (such as second-harmonic generation). This means, structural as well as functional information can be revealed.

For structural and functional analysis of brain it is essential to resolve fine anatomy and activity signals with high spatial and temporal resolution at

different depths. Non-linear, especially multi-photon imaging techniques accomplish this goal adequately and are becoming more widely used in biological and medical research. Here it is interesting to note that Maria Göppert-Mayer (Göppert-Mayer [1930]) predicted the multi-photon effect in 1930. It took nearly 30 years until it could be demonstrated experimentally (Kaiser and Garret [1961]) and another 30 years before it was exploited in the development of the multi-photon laser scanning microscope (MPLSM)(Denk et al. [1990]). It is now among the standard tools for analyzing cellular activity and neuronal circuit both in vitro and in vivo. Its increasing success is also due to the advancements in the development of functional activity sensors.

1.2. Neurobiological foundations

While the history of neuroscience dates back several thousand years it is only 140 years ago that Deiters realized neuronal processes in two categories 1865 (now called axons and dendrites). The powerful silver nitrate staining method of Golgi (1873) lead Cajal (1889) to demonstrate neurons as independent elements in the brain. The pioneering work of Cajal allowed for detailed morphological analysis of neuronal circuits with dendrites as input and axons as output.

Thereupon the research on the computation of neuronal signals in nerve cells largely focused on dendrites. Intracellular recording of electrical signals in nerve cells supported the view of a passive computation as explained by cable theory (for a review see Yuste and Tank [1996]).

Today it is clear that the dendritic tree involves passive as well as regenerative and active components and can be regarded as the computational center of a nerve cell. It is speculated that the non-linear properties greatly enhance the nerve cell's computational power (Poirazi and Mel [1999]).

While multi-electrode recording methods allow detection of activity patterns in distributed neuronal circuits and single-electrode recordings allow electrical recording down to small compartments in single nerve cells in the brain, optical imaging, like two-photon laser scanning microscopy, allows

detection of activity signals in populations as well as in fine neuronal compartments such as boutons and spines. Since these compartments are an integral part of neuronal circuits they can reveal fundamental insight on information processing during behavior.

1.3. Goals of this study

To understand how complex sensory information correlates to a specific behavior, which includes learning and memory or generally the formation of, possibly associative, memory, it is necessary to perform measurements that provide structural as well as functional information with high spatial and temporal resolution (compare Mehta et al. [2004]) over a long time period. For these analyses mammalian systems are well suited as models for behavioral paradigms, including mice, rats and cats. Activity sensors (synthetic dyes or genetic indicators) can now be delivered, by for example injection, breeding or viral infection, into different brain substructures for direct examination of cellular morphology and physiology using two-photon microscopy.

The delivery of functional indicators is the most direct way to examine functional changes in fine neuronal circuits and are most likely to reveal the nature of plasticity in response to changes in sensory experience including learning and memory.

The majority of previous studies carried out in anesthetized animals have severe limitations because the brain state is highly altered (Cotillon-Williams and Edeline [2003]). In order to overcome this limitation studies should be conducted in awake animals.

Clearly, in vivo imaging of living animals is the next important step in systems biology, especially brain research. Miniaturized scanning devices are, however, not only limited to a head-mounted microscope but may also become important in human medicine. We envision their utility in a wide range of treatment and detection methods. For example, visualizing cellular morphology and physiology, monitoring and controlling medical treatments including drug delivery or radiation therapies (compare Christie et al. [1999], Gumbleton and Stephens [2005], May et al. [2001]). A specific

example would be, for example, endoscopic optical coherence tomography (Aguirre et al. [2003]) that allows for direct observation of malignant changes in cellular structure.

Part I.

Light source development

2. Laser cavity design

A simple way to describe a laser cavity is the ABCD-matrix formalism which is well described in literature (see e.g. Siegman [1986]). The treatment of Gaussian beams with ABCD matrix formalism dates back to Kogelnik [1965] and has been extensively used, refined and extended (Alda et al. [1991], Bastiaans [1992], Gatz and Hermann [1994], Kane [1994], Kalashnikov et al. [1995], Lu et al. [1993], Nasalski [1995], Onciul [1992], Porras et al. [1993], Salin et al. [1991], Tari and Richter [1992], Zhao et al. [1994]).

An important step in the description of lasers generating short pulses based on mode-locking by means of a Kerr medium was the development of a suitable ABCD-matrix representing the Kerr effect by Magni et al. (Magni et al. [1993a,b]). While the actual dynamics in these lasers are far more involved this simple description is useful as it deals with the starting conditions for optimizing the geometry of the cavity (for program code see App. C.2).

2.1. ABCD-matrix notation

2.1.1. Formalism based on Gaussian beams

The complex radius of curvature $1/q = 1/r - i\lambda/\pi n w^2$ (with the wave front radius r , wavelength λ , refractive material index n and beam waist w) or its vector $\mathbf{q} = (q, 1)^T$ is transformed according to

$$\mathbf{q} \rightarrow \mathbf{M}\mathbf{q} \quad \text{with} \quad \mathbf{M} = \begin{pmatrix} A & B \\ C & D \end{pmatrix}, \mathbf{q} = \begin{pmatrix} q \\ 1 \end{pmatrix} \quad (2.1)$$

which is analogous to the common representation (“ABCD law”)

$$q \rightarrow \frac{Aq + B}{Cq + D}. \quad (2.2)$$

The respective ABCD-matrices describing the optical elements we use in our standard “Z”-type laser cavity (which are free space propagation, lenses respective spherical mirrors and tilted interfaces on the crystal) are given in Tab. 2.1. These are separated into tangential (x) and sagittal (y) plane to account for astigmatism (Lin et al. [1995]).

Table 2.1.: ABCD-matrices used to describe a standard Z-type cavity: the propagation in space or medium over distance l , thin lens respective mirror with focal length f and tilt angle φ as well as the transformation for a tilted interface with incidence angle φ_i and angle of refraction φ_r . To account for astigmatism of the folded cavity, the matrices have been separated in tangential and sagittal plane.

	Propagation \mathbf{M}_l	Thin lens \mathbf{M}_f	Tilted interface \mathbf{M}_t
tangential	$\begin{pmatrix} 1 & l/n \\ 0 & 1 \end{pmatrix}$	$\begin{pmatrix} 1 & 0 \\ -f^{-1}/\cos \varphi & 1 \end{pmatrix}$	$\begin{pmatrix} \frac{\cos \varphi_r}{\cos \varphi_i} & 0 \\ 0 & \frac{\cos \varphi_i}{\cos \varphi_r} \end{pmatrix}$
sagittal	$\begin{pmatrix} 1 & l/n \\ 0 & 1 \end{pmatrix}$	$\begin{pmatrix} 1 & 0 \\ -f^{-1} \cos \varphi & 1 \end{pmatrix}$	$\begin{pmatrix} 1 & 0 \\ 0 & 1 \end{pmatrix}$

The ABCD-matrix of the Kerr medium is given by (adopted from Magni et al. [1993a]):

$$\mathbf{M}_k = \frac{1}{\sqrt{1-\gamma}} \begin{pmatrix} 1-\gamma/2 & -\gamma t/4n_0 \\ -\gamma n_0/t & 1-\gamma/2 \end{pmatrix} \quad (2.3)$$

with

$$\gamma = \left[1 + \frac{1}{4} \left(\frac{2\pi n_0 w_c^2}{\lambda t} - \frac{\lambda t}{2\pi n_0 w_0^2} \right)^2 \right]^{-1} \frac{P}{P_c}, \quad (2.4)$$

where t is the length of the Kerr medium with refractive index n_0 , the spot size in the center w_c and at the beam waist w_0 (for $P = 0$) and the relation of beam power P to critical power for self-focusing P_c .¹

It should come to attention that the Kerr lens matrix is very similar to a combination of the matrices for propagation and a thin lens ($\mathbf{M}_{l/2} \cdot \mathbf{M}_f \cdot \mathbf{M}_{l/2}$) with a negative length and focusing lens (referring to the effects of “self-shortening” and “self-focusing”, respectively, in Kerr media).

2.1.2. Cavity stability limits

The cavity is described by a matrix containing all optical elements starting at an arbitrary reference plane:

$$\mathbf{M} = \mathbf{M}_N \cdot \dots \cdot \mathbf{M}_i \cdot \dots \cdot \mathbf{M}_1, \quad (2.6)$$

where \mathbf{M}_i is the matrix for the i -th optical element (see Tab. 2.1).

Depending on the mode of operation the reference plane is usually chosen at the output coupler if a hard-aperture should be used while the center of the crystal as reference plane yields information for soft-aperture mode-locking and hints for the pump beam geometry. Alternatively, any plane can be calculated by constructing a suitable matrix starting at the reference plane.

¹The critical power P_c gives an order of magnitude of the power required to get a non-vanishing Kerr effect. An approximation in good accordance with experimental data is

$$P_c = \frac{\alpha \lambda^2}{8\pi n_0 n_2}, \quad (2.5)$$

with a corrective factor α of 5.35 (see Huang et al. [1992]).

The cavity is stable if a full cavity traversal (round-trip) yields a solution for the complex radius of curvature. That means, with the round-trip matrix

$$\mathbf{M}_{\text{RT}} = \mathbf{M}\mathbf{M}^{-1} = \begin{pmatrix} AD + BC & 2BD \\ 2AC & AD + BC \end{pmatrix} \quad \text{with} \quad \mathbf{M} = \begin{pmatrix} A & B \\ C & D \end{pmatrix}, \quad (2.7)$$

a stable configuration is reached if the condition $\mathbf{q} = \mathbf{M}_{\text{RT}}\mathbf{q}$ is satisfied. For the Z-type cavity (Fig. 2.1) the result are two ranges, from stability limit 1 to 2 and 3 to 4 with the folding mirror distance z as dependent variable (see 2.2).

Figure 2.1: Schematic drawing of the Z-type laser cavity without dispersion compensation: output coupler (M_1), focusing mirrors (M_2 and M_3) and Ti:sapphire crystal (compare Fig. 4.1, p. 22).

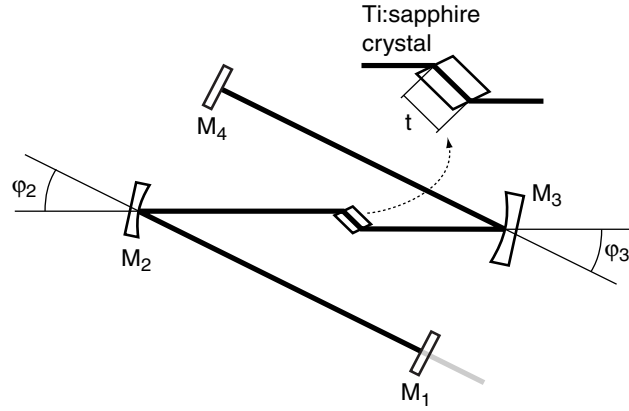
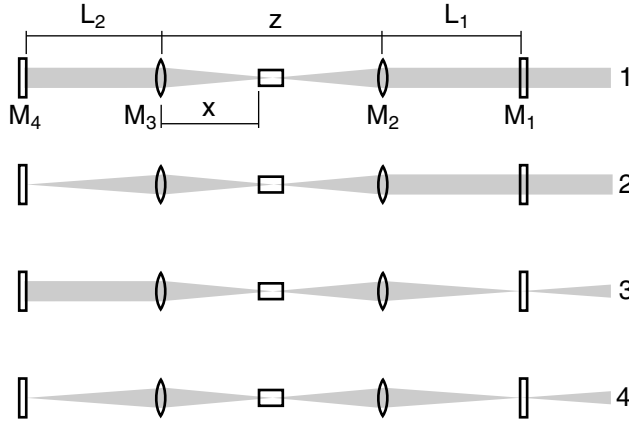


Figure 2.2: Unfolded beam path with the depiction of first to forth stability limit (the order of stability limits is determined by the arm length, here $L_1 < L_2$) of the laser cavity in Fig. 2.1.



A further criterion is the correction of the astigmatism in a cavity containing non-normal interfaces (as is the case for a laser cavity with a crystal cut

at Brewster angle). The stability condition $\mathbf{q} = \mathbf{M}_{\text{RT}}\mathbf{q}$ then applies to both tangential and sagittal axis. This effectively means that the stability limits should be identical for both axes against folding mirror distance z and yields the folding angles φ_2 and φ_3 (see Fig. 2.1).

Due the recursive nature of (2.4) we have refrained of including the matrix for the Kerr medium in the calculation of the stability limits. Qualitatively we can show, however, that a focusing lens in the center of the crystal (which is similar to the self-focusing of the crystal as well as possibly thermal lensing effects) influences the folding towards smaller angles (compare with program code, App. C.2).

2.2. Small signal mode variation

To this point the calculation did not yield any information about the position of the crystal (see Fig. 2.2). To assess its position we follow Magni et al. (Magni et al. [1993a], see also Magni et al. [1995]) by calculating the small-signal mode variation

$$\delta = \frac{1}{w} \frac{\partial w}{\partial p} \Big|_{p=0}, \quad (2.8)$$

with the beam waist w and the factor of beam to critical power $p = P/P_c$.

The mode size variation characterizes the nonlinear losses in a laser cavity and therefore the position of the maximum mode variation is optimal for placing an element with nonlinear loss. Here, this is the placement of a slit near the output coupler (hard-aperturing) or the mode-match with the pump beam inside the crystal (soft-aperturing).

The results of these calculations (see App. C.2 for program code) are used as starting point for the construction and optimization of the cavity (see Sec. 4.2.2 and Fig. 4.3).

3. Dispersion and compensation

Group velocity as well as higher-order dispersion is the major limiting factor when generating or transmitting ultra-short optical pulses. In a mode-locked type laser cavity the generation of ultra-short pulses depends on the compensation of dispersion of the active medium as it leads to pulse spreading which counteracts the phase-locking (commonly referred to as mode-locking).

In the transmission of ultra-short pulses through optical fibers the dispersion can spread the initial pulse severely. For example, a pulse of 100fs doubles its length after about 0.3m while a 10fs doubles after about 3mm.

The cause of dispersion in an optical medium is the wavelength dependent refractive index. In the intended working regime (visible to infrared, far from sharp spectral features) the refractive index can be well approximated by the Sellmeier equation (3.1). The wavelength dependence of the refractive index in the normal dispersion regime generally causes positive group velocity dispersion. Therefore, it is not possible by simply combining different materials to compensate for dispersion and compensation schemes are generally of geometric nature: that is for example the angular dispersion that is used in grating or prism compressors or a specific layer structure with wavelength dependent depth of penetration is used in pre-chirped mirror designs as well as dispersion compensated fibers or Bragg gratings. A totally different possibility is to minimize or avoid dispersion as utilized in hollow core fibers which will, however, not be discussed here.

Prism based dispersion compensation schemes were initially developed by Gordon and Fork (Gordon and Fork [1984]) and later extended to a double prism sequence (Proctor and Wise [1993]). The original formulation by Sherriff (Sherriff [1998]) to describe such prism sequences analytically is insufficient if transmission at non-Brewster angles far from the apex should

be treated and was therefore later extended to a truly arbitrary sequence by Duarte (Duarte [2000a]).

While the analytical description gives valuable insights on relations such as the inverse square dependence of the inter-prism distance on the number of prisms per sequence (Cheng et al. [2002]), numerical ray-tracing provides, in addition, the geometry of the system.

3.1. Dispersion in optical media

Dispersion is ascribed to the wavelength dependent refractive index n which is commonly approximated by the Sellmeier formula (Agrawal [1995])

$$n^2(\omega) = 1 + \sum_i \frac{B_i^2 \omega_i^2}{\omega_i^2 + \omega^2} \quad \text{resp.} \quad n^2(\lambda) = 1 + \sum_i \frac{B_i^2 \lambda^2}{\lambda_i^2 + \lambda^2} \quad (3.1)$$

where ω_i and λ_i are the resonance frequency and wavelength (of the bound electron oscillation), respectively, and B_i is the strength of the i -th resonance. These parameters are usually fitted based on experimental data and extend over all material resonances that contribute to the frequency range of interest (see App. B, tables of Sellmeier coefficients are usually provided by glass manufacturers, see also Han [1995]).

The effect of dispersion is contained in the mode propagation constant β which is expanded in a Taylor series around the carrier frequency ω_0

$$\beta(\omega) = n(\omega)k_0 = \beta_0 + \beta_1(\omega - \omega_0) + \frac{1}{2}\beta_2(\omega - \omega_0)^2 + \dots, \quad (3.2)$$

with the wavenumber $k_0 = \omega/c$ and the speed of light c in vacuum. The first expansion coefficients have the following concrete meaning: β_0 denotes the propagation of the carrier frequency while β_1 is the inverse group velocity and β_2 the group velocity dispersion (GVD). Higher-order derivatives are commonly named after the order of the derivative (e.g. third order dispersion, TOD).

With the used ray-tracing method we obtain the wavelength dependent

optical path length (OPL) with which we obtain the absolute dispersion D_m of order m with

$$D_m = \left(\frac{d^m \text{OPL}}{d\omega^m} \right). \quad (3.3)$$

For group-velocity dispersion compensation with a prism sequence this means that the inter-prism distance has to be chosen so that $D_2 = 0$.

3.2. Ray-tracing fundamentals

The ray-tracing scheme we used effectively contains three steps: 1) the geometric path is calculated based on common ray-tracing techniques including the refraction at an interface, 2) calculation of the optical path length by multiplying each part of the path with the associated refractive index and 3) the differentiation of the OPL to yield the requested order of dispersion. In the following the important formulas used in the model (which basically is the refraction at a flat surface) are described (see App. C.1 for program code).

In mathematical terms this means that we define a ray vector \mathbf{r}_p by its origin \mathbf{P} and its unit direction \mathbf{d}^0

$$\mathbf{r}_p = (\mathbf{P}, \mathbf{d}^0)_p \quad (3.4)$$

for a specified wavelength in section section p (i.e. from a medium interface p to $p + 1$). The vector \mathbf{r}_p is propagated at an optical interface into the next section $p + 1$ defined by the intersection point \mathbf{P}_{p+1} and the new direction \mathbf{d}_{p+1}^0 which is calculated based on the change of the refractive index and orientation of the interface. Then, the OPL is the summation of each section p according to

$$\text{OPL} = \sum_{p < N} n_p \overline{\mathbf{P}_p \mathbf{P}_{p+1}} \quad (3.5)$$

with n_p denoting the refractive index in section p . The indices 0 and N stand for the predefined input and output planes of the optical system.

At a medium interface with refractive index change from n_1 to n_2 the ray is guided according to Snell's law which is in vectorized form

$$\mathbf{d}^0 \rightarrow n^{-1} \mathbf{d}^0 + (\mathbf{s}_p^0 \cdot \mathbf{d}^0 - \sqrt{1 - n^{-2}}) \mathbf{s}_p^0, \quad \text{with} \quad n = \frac{n_1}{n_2}, \quad (3.6)$$

where \mathbf{s}_p is the surface normal of medium interface p at the ray-interface intersection point.

In the program code, however, we will use intermediate steps. With this, a future implementation would allow to model the traversal of interfaces at angles far from the Brewster angle to obtain the attenuation of the beam. This would be necessary, for example, if other materials than fused silica prisms would be used in the dispersion compensation in the laser cavity. According to the Fig. 3.1 we split the incident ray \mathbf{i} into its components parallel and perpendicular to the surface

$$\begin{aligned} \mathbf{i}_\perp &= -(\mathbf{s} \cdot \mathbf{i})\mathbf{s} \\ \mathbf{i}_\parallel &= \mathbf{i} - \mathbf{i}_\perp. \end{aligned}$$

The transmitted beam is refracted according to Snell's law $n_1 \sin \beta = n_2 \sin \alpha$. For the part of the vector parallel to the surface this means that

$$\frac{|\sin \alpha|}{|\sin \beta|} = \frac{|\mathbf{i}_\parallel|}{|\mathbf{t}_\parallel|} = \frac{n_2}{n_1}.$$

If \mathbf{i} is normalized we can write the parallel and orthogonal part of the

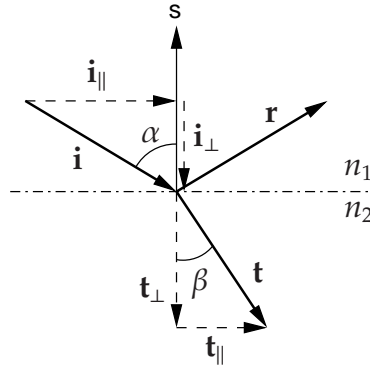


Figure 3.1: Definition of vectorized refraction: incident \mathbf{i} , refracted \mathbf{r} and transmitted direction \mathbf{t} .

transmitted beam vector as

$$\mathbf{t}_{\parallel} = n^{-1} \mathbf{i}_{\parallel} \quad \text{with} \quad n = \frac{n_2}{n_1} \quad \text{and} \\ \mathbf{t}_{\perp} = -\mathbf{s} \sqrt{1 - |\mathbf{t}_{\parallel}|^2}.$$

These vectors would now allow to calculate the attenuation of the beam with the use of the Fresnel formulas.

The only surface type necessary to describe the prism sequence is a (rectangular) planar surface. Such a surface can be defined by its edges \mathbf{A}_{pi} . With the surface vector $\mathbf{s}_p = \mathbf{A}_{pi} \times \mathbf{A}_{pj}$, $i \neq j$ arbitrary, the point of intersection is

$$\mathbf{P}_{p+1} = \mathbf{P}_p + d \mathbf{d}_p^0 \quad \text{with} \quad d = \frac{(\mathbf{A}_{pi} - \mathbf{P}_p) \cdot \mathbf{s}_p}{\mathbf{d}_p^0 \cdot \mathbf{s}_p}, \quad (3.7)$$

where \mathbf{A}_{pi} is an arbitrary point on surface p . Finally we have to verify that the point \mathbf{P}_{p+1} lies on the surface $p + 1$. For a flat surface defined by the polygon $\{\mathbf{A}_i\}_{p+1}$ this means that all sectorial products

$$a_i = \mathbf{n} \cdot (\Delta_i \Delta_{i+1}) \quad (3.8)$$

with $\Delta_i = \mathbf{A}_{pi} - \mathbf{P}_{p+1}$ have identical sign if \mathbf{P}_{p+1} lies inside the polygon. In general ray-tracing schemes it is possible to reduce the number of calculations that need to be done by excluding non-front-facing rays ($\mathbf{d} \cdot \mathbf{n} < 0$), however, as we expect an ordered traversal of the optical elements, a non-intersecting ray counts as clipping.

3.3. Numerical calculation results

The program code for the dispersive ray-tracing only considers two dimensions, that is the beam path on a plane. In the following an overview over the results obtained from numerical calculations is given (see App. C.1 for program code).

In a first example the second and third order dispersion (GVD and TOD)

were calculated for different materials: the Ti:sapphire crystal, fused silica, and glass types BK7, FK5 and SF20 (see Fig. 3.2). As expected, fused silica is the material with lowest GVD as well as TOD. Based on early analytical considerations (Sherriff [1998]) we estimated that a beam traversal of a prism far from the apex would simply add the dispersion of the distance traveled through the prism and therefore assumed that a material with low GVD is optimal which is the case for fused silica prisms (it should be noted that using fused silica as prism material is also preferred due to the small change of refractive index and, therefore, small reflection losses for broad spectra).

Recent numerical simulations of the double-prism sequence, surprisingly,

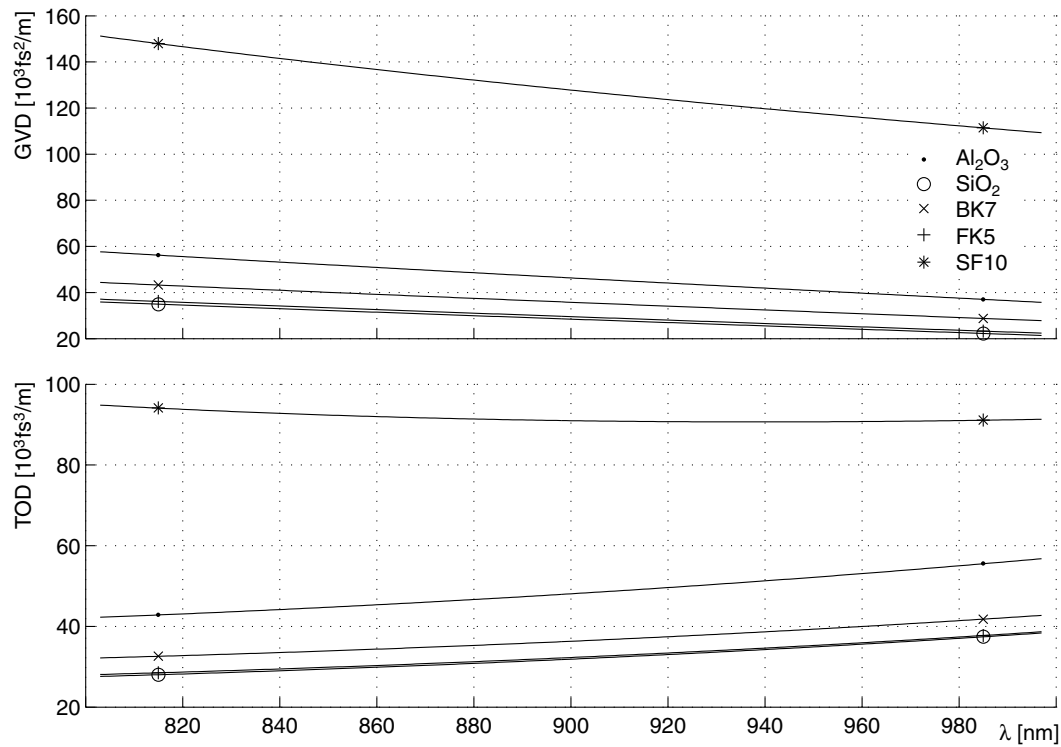


Figure 3.2.: Group velocity dispersion (GVD) and third order dispersion (TOD) as calculated from numerical dispersion compensation model for different materials: Ti:sapphire crystal (Al_2O_3), fused silica (SiO_2) and the glass types BK7, FK5 and SF10.

show that better results could be obtained with BK7 glass (see Fig. 3.3). While we, therefore, assume that an even better compensation can be achieved by proper selection of prism materials and possibly by using a combination of different materials in a single prism ring, the extension of the program code to include the transmission ratio of the intensity will be required, especially if these prism should be used in a laser cavity.

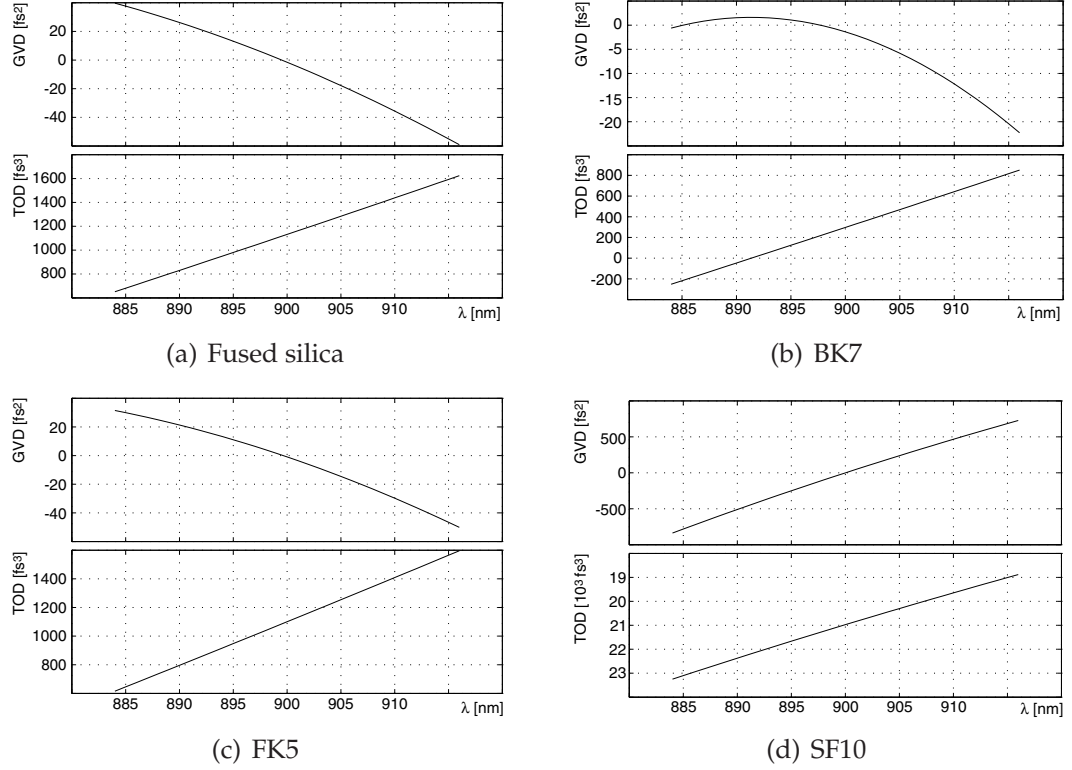


Figure 3.3.: The results of the optimization process of the inter-prism distance for the laser crystal of Chap. 4 for zero-GVD with different prism materials (Fused silica, BK7, FK5 and SF10): Shown are the GVD and residual TOD curves for a design wave length of 900nm (with a band-width of 40nm). The apex angles were chosen at Brewster angle (69.1° , 67.1° , 68.1° and 61.0°) and the inter-prism distances are 190mm, 176.4mm, 189.8mm and 112.3mm.

4. Tunable Ti:sapphire oscillator with pure prism-based dispersion compensation for high-repetition rate and short pulses

A laser was designed and constructed with the goal of producing ultra-short pulses at a high repetition rate as needed for certain applications of multi-photon microscopy. With pure prism based dispersion compensation repetition rates of up to 270MHz were achieved. The laser operates with hard- and soft-aperturing at the third (diverging output) and the first stability limit (parallel output), respectively. At the third stability limit we demonstrate a near Gaussian pulse with an auto-correlation width of 37fs (FWHM) at 800nm central wavelength. At the first stability limit broad tunability of the central wavelength from 780nm to 920nm with auto-correlation pulse width of typically 40–50fs are demonstrated.

4.1. Introduction

Efficient multi-photon laser-scanning microscopy (MPLSM) requires pulsed excitation because the efficiency of non-linear optical processes depends on the averaged n -th power of the instantaneous laser intensity. For 2-photon excitation this means that at constant average power the average excitation rate increases with the reciprocal duty cycle ($I \propto P_{\text{mean}}^2 / f\tau$, with the average fluorescence intensity I , the repetition rate f and the pulse width τ). While the duty cycle can, of course, be reduced by lowering the pulse-repetition rate (Theer et al. [2003]) a high repetition rate is often desirable or even necessary for a number of reasons, e.g. the reduction of the non-linear pulse broadening (see below) (Denk et al. [1995]). The use of femto-second pulses is, therefore, standard in multi-photon microscopy. In fact,

commercially available mode-locked Ti:sapphire lasers are the excitation-light source used for the vast majority of multi-photon microscopes in operation. The repetition rate of such lasers around 100MHz provides a sufficient number of pulses per pixel to avoid the need for synchronization between pulses and acquisition clock. With an easily achievable pulse width of around 100fs the inverse duty cycle (and hence enhancement of 2-photon absorption) is about 10^5 .

While for most applications such pulse parameters are appropriate, sometimes higher repetition rates are desirable or even necessary: (1) when saturation due to ground-state depletion limits the achievable fluorescence intensity (Marcano and Urdaneta [2001]), (2) when super-linear bleaching (Patterson and Piston [2000]) or photodamage need to be minimized but a certain fluorescence intensity is needed, such as in fluorescence correlation spectroscopy (Dittrich and Schwille [2001]), or (3) when excitation through optical fibers is necessary, where lowering the pulse energy by increasing the repetition rate allows a reduction of nonlinear pulse broadening (Agrawal [1995]). To make up for the reduction of the excitation efficiency due to the increased repetition rate shorter pulses can be used. Somewhat surprisingly, shorter pulses may, furthermore, reduce the severity of non-linear effects in fibers as the length of fiber over which high peak powers persist is shorter due to the larger spectral width (Clark et al. [2001]).

A laser suitable for multi-photon optical imaging requires wavelength tunability to allow the excitation of different fluorophores, and, for operation in conjunction with optical fibers, pulses substantially below 100fs and repetition rates substantially above 100MHz. Very high repetition rates (in the GHz regime) can be achieved by using chirped-mirror dispersion compensation (Bartels et al. [1999], Bartels and Kurz [2002]) but usually at the expense of broad tunability. We, therefore, custom designed a laser optimized for high repetition rates and short pulses with pure prism-based dispersion compensation (compare Lytle et al. [2004]).

4.2. Design

A major factor limiting the repetition rate of mode-locked lasers is the optical path length required for prism-based group velocity dispersion (GVD) compensation (Brabec et al. [1991]). This is particularly true for very short pulse durations where fused-silica prisms need to be used since prisms made from high-dispersion materials generate too much third-order dispersion (TOD) (Lemoff and Barty [1992], see also Chap. 3). To reduce the required inter-prism distance we used two pairs of prisms (Proctor and Wise [1992]), resulting in a reduction of the required apex distance by roughly a factor of four (Cheng et al. [2002]). When using a 5mm long Ti:sapphire crystal the required inter-prism distance for GVD compensation is ≈ 200 mm. Mechanical constraints add about 100mm leading to a total length of 300mm of the L_2 arm of the cavity (for a drawing of the cavity layout, see Fig. 4.1).

The L_1 arm also requires a minimum length if beam propagation is not parallel, as is the case for mode-locking near the third stability limit of the cavity using a hard-aperture which needs to be placed near the end of L_1 at the output coupler. The theoretical lower limit for L_1 is then twice the focal length of M_2 , in our case $L_1 = 100$ mm. In practice we could reliably maintain mode-locking only down to about $L_1 = 200$ mm (see below). An alternative is to operate the laser at the first stability limit, necessarily then without a hard aperture (Fig. 4.1, slit S_1 removed and parallel ray propagation in both arms), which places no limit on L_1 . We designed and operated cavity variants for both 3rd and 1st stability limit operation.

4.2.1. Dispersion compensation

The double-prism sequence we used for GVD compensation is often referred to as the Proctor and Wise arrangement (Proctor and Wise [1992]). To calculate the needed inter-prism distance we initially used analytical expressions derived by Sherriff (Sherriff [1998]) for prism sequences that are more complicated than the original Gordon and Fork (Gordon and Fork [1984]) arrangement. Assuming a 5mm long Ti:Al₂O₃ crystal (the GVD introduced by the crystal was calculated using the Sellmeier formula,

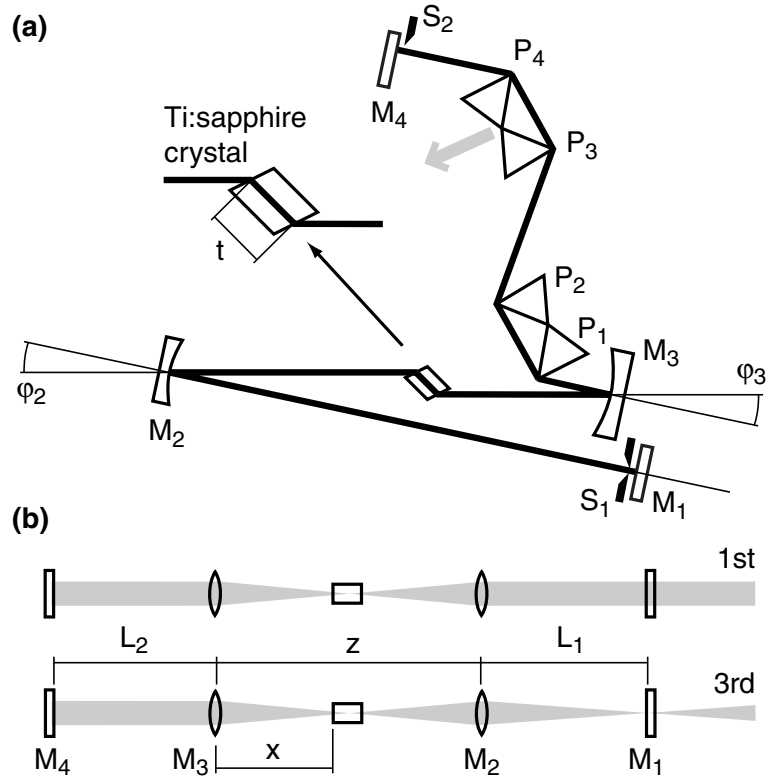


Figure 4.1.: (a) Schematic drawing of the laser cavity: output coupler (M_1), focusing mirrors (M_2 and M_3), Ti:sapphire crystal, dispersion compensation consisting of four prism (P_1 to P_4), end mirror (M_4) and hard aperture slit (S_1) and wavelength controlling vane (S_2). The inter-prism distance is measured from apex to apex (P_2 to P_3). The pump beam (not shown) is focused into the crystal through M_3 . (b) Unfolded beam path at the 1st and 3rd stability limit with the focusing mirrors represented as lenses (see text for further details).

Han [1995]) and a beam that is passing 4mm of glass at each prism at the central wave length we find an inter-prism distance (IPD, apex P_2 to apex P_3) of 187mm is needed to balance the cavity GVD at 850nm, the design wavelength of the prism arrangement. The Sherriff formulas are, however, only valid at minimum deviation (Sherriff [1998], see also Duarte [1995,

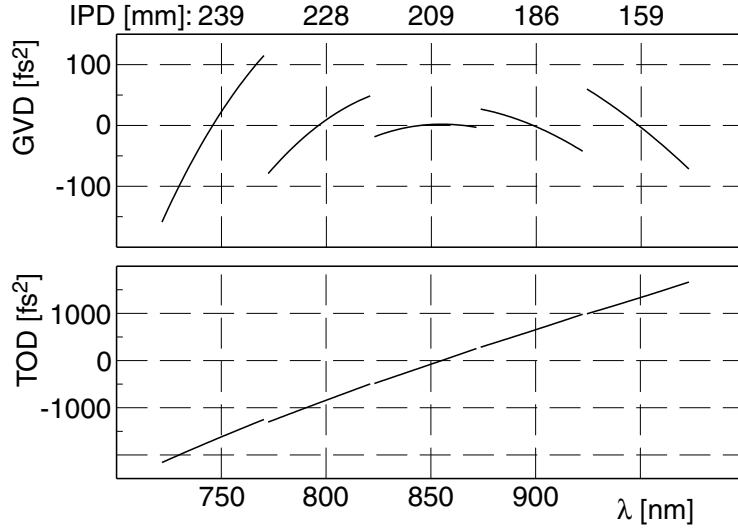


Figure 4.2.: Calculated intra-cavity group-delay (GVD) and third-order dispersion (TOD) for five different wave length ranges. At the central wavelength of each partial trace the inter-prism distance was adjusted (to values of 239, 228, 209, 186 and 159mm, respectively) for zero GVD.

2000b]) and adjusting the prism angles to keep them at minimum deviation while tuning the laser wavelengths is impractical. We, therefore, used a numerical ray-tracing technique instead to calculate the dispersion (for an analytical solution for arbitrary prism sequences see (Duarte [2000a])).

As a side-effect the ray-tracing allowed us to follow rays at the beam edges and check for clipping: For the design of the laser we specified that a beam with 4mm diameter and a bandwidth of $\pm 30\text{nm}$ should just remain inside the prisms apices. In this case the required IPDs become 239, 228, 209, 186 and 159mm for 750, 800, 850, 900, and 950nm, respectively. The corresponding GVD and TOD curves are shown in Fig. 4.2. The residual TOD, which limits the shortest achievable pulse width, is below 1700fs^3 in the range from 750 to 980nm, which allow to get pulses below 30fs (Brabec et al. [1992]).

4.2.2. Cavity optimization

The cavity was modeled using the ABCD matrix ansatz (Kogelnik [1965]) in a two-step approach (see detailed description in Chap. 2 and program code in App. C.2): first we calculated the stability regions as a function of the folding mirror distance (z), with L_1 and L_2 as parameters without, however, taking optical non-linearity into account. Since the crystal faces are traversed and the curved mirrors reflect at non-normal angles we have to treat the tangential and sagittal planes separately. For the first stability limit both folding angles have to be identical if the beam inside the crystal is to be stigmatic ($\varphi_3 = \varphi_2 = 17.1^\circ$) and the folding mirror distance is then $z_1 = 108\text{mm}$. For the third stability limit the folding angle (φ_3) for the arm with the parallel beam (L_2) is unchanged if the beam inside the crystal is to remain stigmatic and we can calculate φ_2 using again the condition that the tangential and sagittal stability limits have to occur at the same z ($z_3 = 125\text{mm}$). We find $\varphi_2 = 13.2^\circ$ for an arm length of $L_1 = 200\text{mm}$ (unlike for the first stability limit, φ_2 does depend on the arm length, with values ranging from 8.5° to 14.2° for $L_1 = 100\text{mm}$ to 300mm).

In a second step we introduced Kerr lensing represented by an additional ABCD matrix. We then calculated for a given z that position (x) of the crystal for which the maximal intensity dependence of the beam diameter at the output coupler occurs (Magni et al. [1993a]). We found $x = 50.45\text{mm}$ both at the first and at the third stability limit: we also found (Fig. 4.3) that the mode variation is dominant in the tangential plane which is essential for a vertically orientated slit aperture.

4.3. Cavity construction

The cavity focusing mirrors have a radius of curvature of 100mm ; the output coupler has a transmission coefficient of 12% (all cavity mirrors used were from a broad-band "X-Wave" mirror set for a Mira 900 Laser, Coherent GmbH, Dieburg, Germany). The prisms are fused silica with an apex angle of 68.7° (IB-10.5-68.7-SS, CVI Laser Corporation, New Mexico, USA). The gain medium was a short (5mm) highly doped ($\alpha = 3.4\text{cm}^{-1}$) $\text{Ti:Al}_2\text{O}_3$ crystal

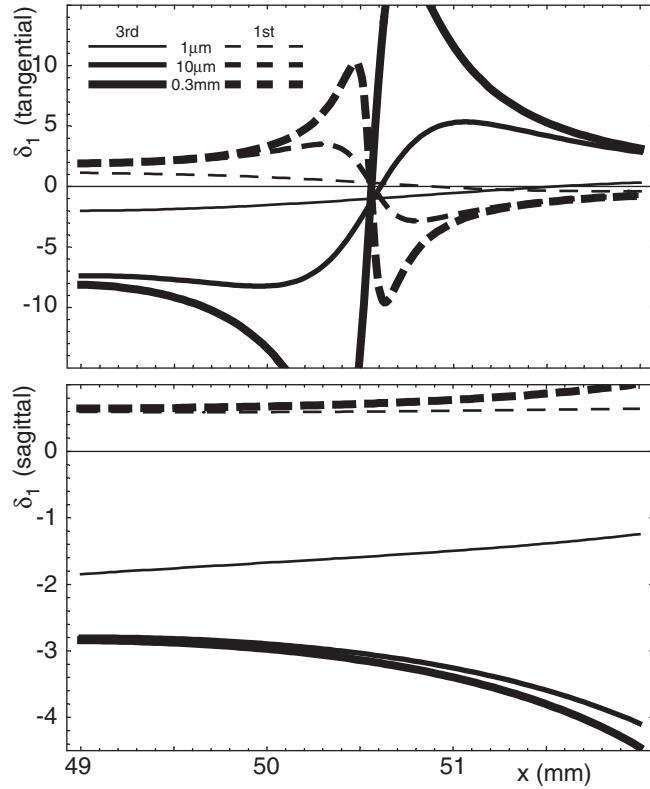


Figure 4.3: First order Kerr-lens induced differential mode size variation on the output coupler in the tangential (*top*) and sagittal (*bottom*) plane plotted as a function on the crystal position x near the first (*dashed*) and the third stability limit (*solid*). Shown are data for three different offsets of z : 0.3, 0.01 and 0.001mm (increasing δ_1 with vanishing z) from the respective limit. Note difference in scales.

cut at Brewster's angle (MolTech GmbH, Berlin, Germany) pumped with up to 10.5W of the 532nm light from a diode-pumped frequency doubled Nd:YVO4 laser (Verdi V-10, Coherent Inc.). The focusing mirror for the pump beam was taken from a Tsunami laser (Spectra Physics).

4.3.1. Alignment

We first optimized the cavity for CW operation without the prism sequence. The arm lengths L_1 and L_2 were first set to be nearly equal, at about 300mm, with L_1 slightly smaller than L_2 to ensure a small spot on the OC at the third stability limit. For operation at the third or first stability limit we started out with z set slightly larger (1–2mm so that z is inside the stability limit) than the theoretical values of $z_3 = 125\text{mm}$ and $z_1 = 108\text{mm}$, respectively. The end mirror tilts, crystal position, and pump focus were then adjusted

for maximum output power.

For third-stability limit operation we then began to reduce L_1 while keeping the CW power maximized by making small adjustments to the end mirrors and to x , z , and φ_2 . While the calculated values for the optimal folding angles are $\varphi_2 = 13.2^\circ$ and $\varphi_3 = 17.1^\circ$ for a $L_1 = 200\text{mm}$ we found that, in practice, the optimal folding angles seem pump power dependent. Better results were obtained by decreasing the folding angles while increasing the pump power, presumably due to astigmatic thermal lensing. For pump powers between 6 and 8W good results were obtained with $\varphi_2 = 12^\circ$, and $\varphi_3 = 13^\circ$. These values are not optimal, especially when L_1 should be shorter than 200mm, but due to mechanical constraints φ_2 could not be reduced below 12° . Residual astigmatism can strongly affect mode-locking because Kerr lensing is dominant in the tangential plane (see Fig. 4.3). This means that to ensure effectiveness of the slit we have to keep the tangential mode variation on the output coupler at least as large as the sagittal mode variation. In practice, this can be tested by observing the size and ellipticity of the output beam as z is decreased towards the third stability limit: with proper astigmatism compensation the beam stays round as its diameter increases with decreasing z .

At the first stability limit the folding angles ($\varphi_2 = \varphi_3$) were varied between 13° and 17° . For a pump power of 10W an angle of 15° appeared to yield the best results for mode-locking operation. As we have parallel ray propagation in the L_1 arm, L_1 can be made quite small, limited only by mechanical constraints, and was initially set to 200mm and later reduced to 95mm. As expected from the calculations we did not observe any relation between L_1 and mode-locking capability experimentally.

4.3.2. Prism sequence alignment

First we inserted only the prism pair P_1/P_2 into the cavity. The end-mirror horizontal tilt was initially set so that the laser operated at the intended wavelength. The angular orientation of prism pair P_1/P_2 was then adjusted to yield the minimal wavelength. These steps were repeated until the minimal wavelength and intended wavelength are equal. This adjustment corresponds to the minimum-deflection orientation for P_1/P_2 . The second

prism pair (P_3/P_4) was then inserted and its angular orientation was adjusted so that tilting the end mirror no longer produced a shift in the operating wavelength.

4.3.3. Mode locking

Before attempting to start mode-locking at the third stability limit we had to adjust the folding-mirror distance z and the crystal position x , which were still set for maximum power in CW-mode ($z = 118 \pm 2\text{mm}$, $x = 51 \pm 1\text{mm}$). Empirically we found that the laser started to mode-lock most easily when (at a pump power $P = 6\text{W}$) z and x were increased by 0.3mm and 0.1mm , respectively. To start mode-locking we first closed the slit in front of the output coupler until the output power was reduced by 25%. The vane S_2 , which controls the wavelength and which is located in front of M_4 , was adjusted so that wavelengths above 805nm were blocked. Mode-locking could now easily be started by briefly and quickly pushing P_3/P_4 away from the beam (less glass, direction denoted by the arrow in Fig. 4.1).

To start mode-locking at the first stability limit we found that, like for the third stability limit, the folding mirror distance z has to be increased with rising pump power. Empirically we found that at a pump power of 10.5W mode-locking could be achieved by increasing z by 0.5 to 1.0mm from the maximum CW power ($z = 105 \pm 2\text{mm}$). The position of the crystal is selected by constantly moving the prism pair P_3/P_4 in and out of the beam and set to a position where mode-locking starts with as small as possible movement.

We observed in practice that the initial alignment of the cavity at the first stability limit is more sensitive to misalignment, as can be expected when operating with soft-aperturing and parallel ray-propagation in both arms, than when working at the third stability limit. This alignment sensitivity appeared mainly as instability of the mode-locking process (breakdown to CW within seconds) as well as sharp frequency peaks (possibly CW). We have, therefore, further optimized the crystal position and the end-mirror tilt while the laser was mode-locking. Alternatively it was possible to reduce sharp frequency components by using the S_2 vane. Interestingly, we found that the cavity is less susceptible to dust at the first stability limit with roughly a doubled cleaning interval time (several month).

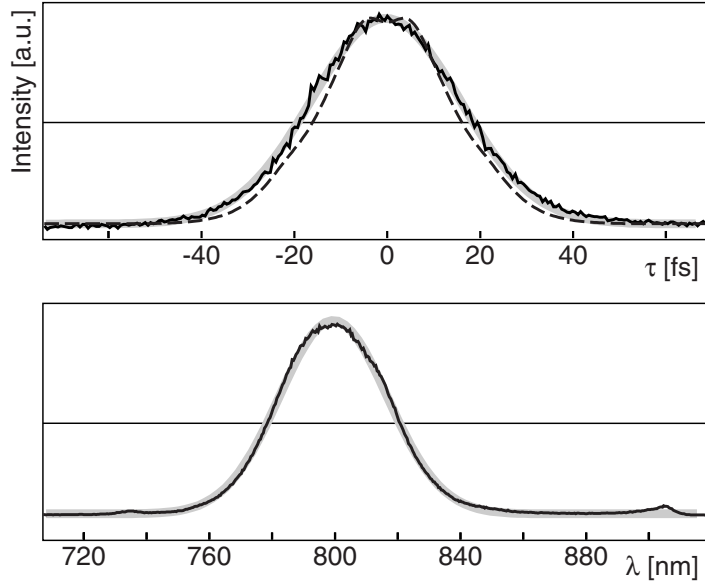
4.4. Results

Near the third stability limit, running CW at a wavelength of 810nm the laser had conversions efficiencies of up to 15% at a pump power of $P_p = 6W$ and 17% at $P_p = 10W$. The lasing-threshold was at $P_p = 2.1W$.

In mode-locked operation at a center wavelength of 800nm the conversion efficiencies were 10% and 12.5% at $P_p = 6W$ and $P_p = 8W$, respectively. A spectral and auto-correlation trace were recorded with GVD compensation (by two SF10 prisms) after the output coupler (Fig. 4.4). Chi-squared fits assuming a Gaussian pulse profile (carried out with ROOT) gave a central wave length of $797.8 \pm 0.2\text{nm}$ ($376.1 \pm 0.1\text{THz}$, mean \pm SEM), a spectral width of $41.4 \pm 0.1\text{nm}$ ($19.5 \pm 0.1\text{THz}$) and a pulse width of $26.5 \pm 0.1\text{fs}$. The time-bandwidth product calculated from these values is 0.52, slightly larger than the transform limit of 0.44. The pulse repetition rate was $\approx 240\text{MHz}$.

For an inter-prism distance of 185mm the tuning range for stable mode-locking (at the third stability limit) was 750nm to 805nm center wavelength. Beyond 805nm the spectrum became distorted and mode-locking broke down completely beyond 810nm. While we have not investigated this in

Figure 4.4: Auto-correlation (*top*) and spectrum (*bottom*) of laser output at the third stability limit, Gaussian fit (*gray*), and Fourier transform of the spectrum (*dashed*), corresponds to the auto-correlation expected for a transform limited pulse.



detail as we switched to the 1st stability limit (where external compensation of the diverging beam is dispensable, reducing the complexity of the adjustment for fiber coupling) we assume that reducing the IPD would allow for long wavelength (it should also be noted, that the crystal at an angle itself adds negative dispersion, Zhang et al. [2004]).

At the first stability limit the conversion efficiencies were similar, reaching a peak of 19% at $P_p = 10\text{W}$ at 810nm but the lasing-threshold was slightly higher at $P_p = 2.2\text{W}$. We achieved stable mode-locked operation of the laser at a pump power of $P_p = 10\text{W}$, over a wider spectral range than when operating at the 3rd stability limit. The center wavelength mainly depended on how far the prism pair P_3/P_4 was inserted (observation of how the beam travels through the prisms seems to suggest that dispersion is the main control mechanism here; this is also supported by the fact, that it is not possible to shift the central frequency by the use of the wavelength controlling vane S_2 without disturbing mode-locking). The spectra typically deviate strongly from the Gaussian shape (Fig. 4.5). The wavelength bandwidth typically reaches 40–50nm between 780 to 910nm. At a central wavelength of 870nm a maximal bandwidth of over 100[nm] is reached (it should be noted that this coincides with the calculated minimal TOD, see Fig. 4.2). The auto-correlation pulse-widths (with external GVD compensation with a pair of fused-silica prisms) were typically between 40–50fs. By comparing the calculated (Fourier-transformed spectrum) and the measured auto-correlation trace we see, however, that the measured pulse width is typically twice (up to four times for the broad spectrum at 870nm central wavelength) that of the transform-limited width. The according pulse width should, therefore, be typically below 30fs (FWHM) based on the comparison with the Fourier-transformed spectra (see Fig. 4.6).

The peak conversion efficiencies varied from 12% to 7% for wavelengths between 800nm and 920nm.

4.5. Conclusions

We have demonstrated stable operation of a high-repetition rate Ti:sapphire oscillator with pure prism based dispersion compensation in different cavity

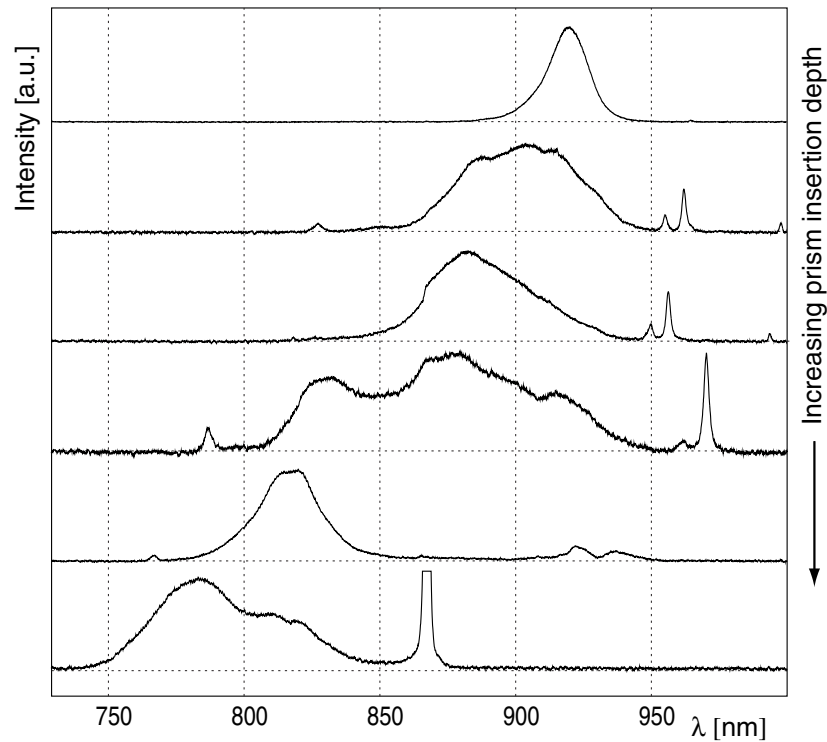


Figure 4.5.: Different spectra taken at different insertion depths of prism pair P_3/P_4 of the laser operating at the first stability limit (compare Fig. 4.1, wavelength increases for moving prisms in the direction of the gray arrow). Depending on the alignment of the laser cavity additional CW parts can be observed (spectrum at bottom).

modes. We can reach sub-30fs pulses for hard-aperture (third-stability limit) as well as soft-aperture (first-stability limit) supported mode-locking with up to 270MHz repetition rate. In comparison to a typical commercial laser (80MHz, 100fs) our laser thus achieves a 3-fold higher repetition rate and a 3-fold shorter pulse length. Most important for us is that stable operation near 930nm is possible since the xanthene dyes Xu and Webb [1996] as well as many fluorescent proteins can be efficiently excited Xu et al. [1996].

Applications envisioned for this laser include situations where pulse energies have to be minimized, for example to reduce superlinear photobleach-

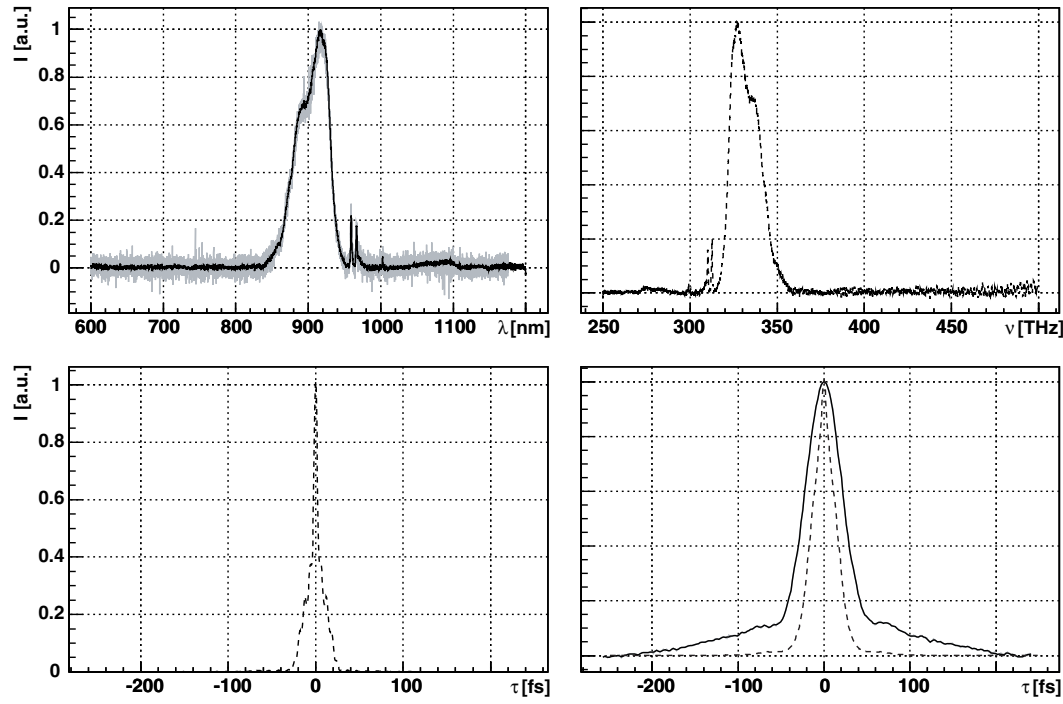


Figure 4.6.: Comparison of the measured spectrum and auto-correlation trace by Fourier analysis (gray: original data, solid: smoothed data and dashed: calculated data): (*top left*) the measured spectrum (50nm FWHM) is transformed from wavelength to frequency (26THz rms width, *top-right*) and Fourier-transformed to yield the pulse (17fs rms width, *bottom left*) and compared with the auto-correlation trace (*bottom right*): the computed auto-correlation width is 29fs (FWHM) compared to the measured FWHM width of 52fs.

ing (Schwille et al. [1999], Dittrich and Schwille [2001], Eggeling et al. [1998], Brand et al. [1997], Patterson and Piston [2000]) or for a multi-photon fiber microscope (Helmchen et al. [2000, 2001, 2002]). Preliminary experiments (Sawinski and Denk, unpublished data) show that when passing the output from this laser with appropriate pre-chirping (prism sequence with 5 fused silica prisms each) through 1m of a standard single-mode fiber we can reach pulse lengths around 100fs for an average output power of up to 300mW at 900nm central wavelength.

Part II.

Head-mount microscope

5. Piezo lever fiber scanner model

In the design of the piezo lever fiber scanner (PLFS) we have to deal with the bending of the fibers, their material limits and the actuators which are piezo bending elements. In the following a short introduction will be given to develop finally the scanner model used to estimate the performance of the scanner.

5.1. Bending of a beam

5.1.1. Bernoulli bending

A beam with constant cross section under bending exhibits a linear transverse tension distribution over its length (see Fig.5.1(a), this simplified examination dates back on Bernoulli, 1700, see Budó [1990]). In equilibrium the integrated tension over the cross section is zero, which means, that if the beam is bent downwards a neutral plane (yz) exists for which the relative elongation (ε_{xx}) is zero (see Fig. 5.1(a)). With the theorem of intersecting lines it is obvious that if the neutral fiber is defined for $z = 0$ the relative elongation scales inversely with the bending radius R with $\varepsilon_{xx} = -z/R$ (sign for counter-clockwise orientation of R). According to Hooke's law the normal strain along the x -axis P_{xx} is thus

$$P_{xx} = E\varepsilon_{xx} = -E\frac{z}{R}, \quad (5.1)$$

with the modulus of elasticity E .

Using (5.1) the inner bending moment M_b at any position x is then

$$M_b = \int_A zP_{xx}dA = -EI R^{-1} \quad (5.2)$$

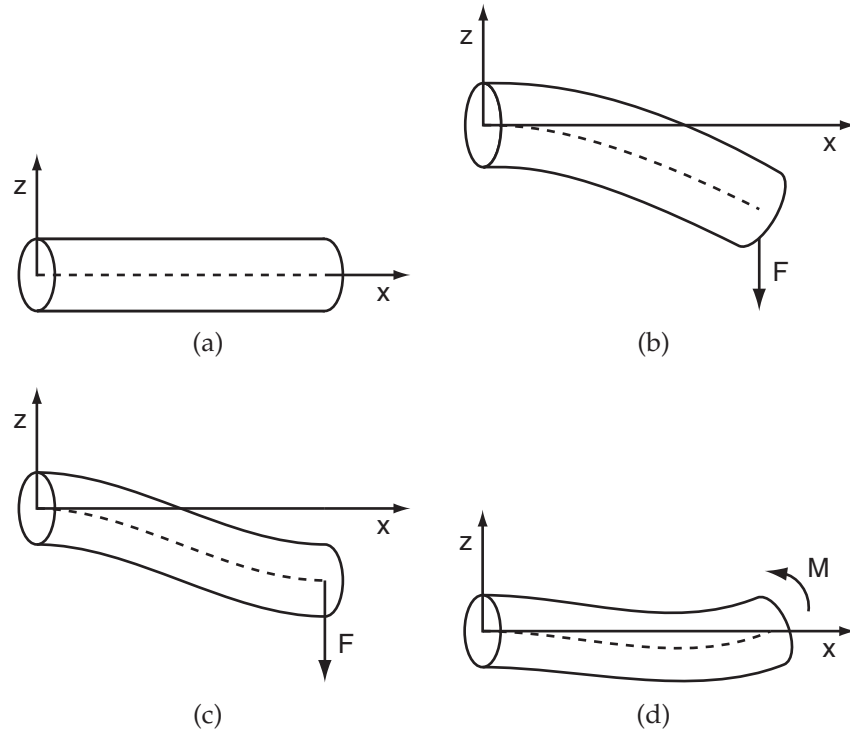


Figure 5.1.: a) Definition of coordinate system (axis y , not shown, is perpendicular to axes z and x). The bending modes involved in the design of the scanner: b) Bending of the scanner fiber, a fixed beam with a free end (the bending moment due to the cross connects, not shown, attacks at the free end, compare 5.6); b) fixed beam with a rotationally free end, and c) beam with parallel ends.

with the area moment of inertia

$$I = \int z^2 dA. \quad (5.3)$$

Assuming small deflections the bending radius can be approximated by $R = z''/(1 + z'^2)^{3/2} \approx z''$ (compare experimental results, Sec. 6) and we get the differential equation for the static (i.e. in equilibrium with an external

bending moment $M(x)$) bending of a beam:

$$EI z''(x) = M(x). \quad (5.4)$$

Following Bernoulli's description the externally applied bending moment can be considered linear for small deflections. By separating each beam into parts so that $z(0) = z'(0) = 0$ (fixed end) and further by describing the bending moment distribution by the bending moments at the ends of each beam part ($M(x) = M_0 \cdot (1 - x/L) + M_1 \cdot x/L$, with the beam length L) the solution of the differential equation can be written in the form of a spring equation with

$$\varphi := z'(L) = \frac{K'^{-1}}{L} (M_0 + M_1) \quad \text{with} \quad K' = 2EI L^{-2} \quad (5.5)$$

$$s := z(L) = \frac{K^{-1}}{L} \left(M_0 + \frac{1}{2} M_1 \right) \quad \text{with} \quad K = 3EI L^{-3}. \quad (5.6)$$

The different bending modes of the beam parts are as follows (compare Fig. 5.6): The force delivering suspension is subject to a central bending moment due to the deflection of the fiber (rotationally free end) while the orthogonally crossing suspension experiences a shear force (parallelly shifted end). The excitation fiber is thus subject to a transverse force as well as to a torque (partially free end).

Rotationally free end: If a bending moment M is applied at the rotationally free end, the additional boundary condition ($z(L) = 0$) relates the moment on the fixed end with (5.6): $M_0 = -M/2$. Thus, with (5.5), the beam is described by

$$M = \varphi \cdot 2K' L. \quad (5.7)$$

Parallelly shifted end: The parallel shift is caused by the force F , with the boundary condition for parallel shift ($z'(L) = 0$) we can express the moments at the end with $M_0 = -M_1 = -F \cdot L$. Thus with (5.6) we get

$$F = s \cdot 2K. \quad (5.8)$$

This beam part also exhibits an axial moment due to twisting (compare Fig. 5.6) which is described by the torque

$$M = \varphi \frac{GI}{L} \quad (5.9)$$

with the modulus of rigidity G .

Partially free end: To describe the excitation fiber, we have to handle the suspension that delivers the actuator force (see “Rotationally free end”) that causes an opposing moment M at the free end of the beam part. Thus the excitation fiber is described by

$$\varphi = -K'^{-1} \left(F + \frac{M}{L} \right) \quad (5.10)$$

$$s = -K^{-1} \left(F + \frac{1}{2} \frac{M}{L} \right), \quad (5.11)$$

where F is the force that deflects the fiber and M the moment caused by the cross connects.

5.1.2. Resonant limitation

An important factor in the description of the scanner is the resonance frequency that limits the speed of operation. The resonance frequency of a uniform beam is according to Búdo (Budó [1990])

$$v_n = \frac{(\alpha_n L_f)^2}{2\pi L_f^2} \sqrt{\frac{EI}{\rho A}} \quad \text{with} \quad I = \int_A z^2 dA \quad (5.12)$$

with the modulus of elasticity E , moment of inertia I , the density ρ and cross-section A . The (αL_f) are derived through a transcendental function (which is the result of the boundary conditions within the solution of the Bernoulli-Euler differential equation for bending waves in solids, see Budó [1990]) and can be approximated by: $\alpha_1 L_f \approx 1.875$, $\alpha_2 L_f \approx 4.694$, $\alpha_3 L_f \approx 7.8550$ and further $\alpha_n L_f \approx (2n - 1)\pi/2$.

5.2. Stress limits

An important part of the design of the piezo scanner is the calculation of critical internal forces of the cross-connects and also the excitation fiber, that is, we need to know the mechanical (elastic) limits of the structure. There are effectively three failure modes involved: (1) bending of all fibers is limited by their bending stress limit and (2) the tension and pressure of the cross-connects are limited by the yield strength and (3) the cross-connects may be subject to buckling under pressure.

5.2.1. Bending strength

The bending strength is the limit where fracture occurs and is related to the inner bending moment M_b and the first moment of area W by

$$\sigma_b = \frac{M_b}{W} \quad \text{with} \quad W = \int_A^* x dA, \quad (5.13)$$

with the cross-sectional area A^* above or below the neutral phase.

Using (5.7) we get a bending stress of the cross-connect parallel to the applied force (with $W = \pi d^3/32$ for a circular cross-section, see Metall [1990])

$$\sigma_b = \varphi \frac{2d}{L} E. \quad (5.14)$$

The bending stress limit yields an upper boundary for a fiber diameter. In the case of fused silica, the maximum diameter of the cross connects would be $308\mu\text{m}$ (assuming a maximum slope of $\varphi = 0.1$ of the excitation fiber and a minimal length l_s of the cross connect of 1mm , see Fig. 5.5). By comparing (5.5) and (5.9), it is obvious that the maximum diameter of the scanner fiber is twice that of the cross connects under the same conditions ($\varphi = 0.1$, $l_f = 1\text{mm}$). For a steel wire the maximum diameter is between $13\mu\text{m}$ and $38\mu\text{m}$. Steel appears, therefore, not suitable as a cross connect material (see also buckling, Sec. 5.2.3).

5.2.2. Yield strength

The yield strength is the limit of the tensile or compressive stress σ defined by

$$\sigma = \frac{F}{A} . \quad (5.15)$$

with applied force F and cross sectional area A . It is a measure for the limit of the elastic regime, that is, before permanent deformation occurs.

The yield strength of fused silica is about $\sigma = 50 \cdot 10^6 \text{N/m}^2$. That means the minimum diameter of such a fiber to support a tension force of 100mN (blocking force of a single piezo bending element in bipolar operation) is $50 \mu\text{m}$.

5.2.3. Buckling

Another factor limiting the stability of the scanner is buckling. The buckling force, i.e. the maximum force at which buckling can occur, is given by (see Metall [1990])

$$F_k = \pi^2 \frac{EI}{l_k^2} \quad (5.16)$$

with the free buckling length l_k (see Fig. 5.2). The buckling length l_k is related to the beam length l by: $l_k = 2l$ for one free end, $l_k = l$ for rotationally free ends, $l_k = 0.7l$ for rotationally free-fixed and $l_k = 0.5l$ for fixed ends. In case of the scanner, the cross-connect point is not completely fixed, therefore, to yield a safe limit in terms of l_k we use the definition for Fig. 5.2c). Then, a force of $F = 100 \text{mN}$ will require a minimal diameter of $33 \mu\text{m}$ for fused silica ($E = 73 \text{N/m}^2$).

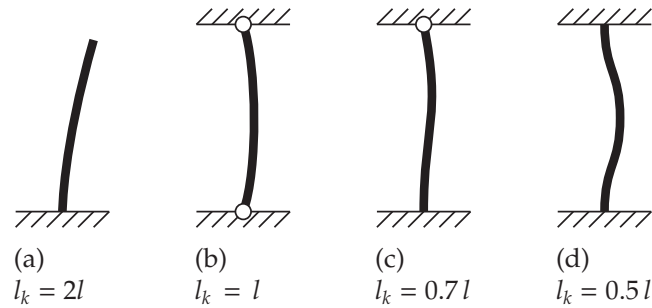


Figure 5.2.: Definition of the free buckling length l_k : The hatched surfaces represent fixed connections to the beam subject to buckling, the circles allows a rotational degree of freedom.

5.3. Piezo bending element

Bending elements are constructed from layers of piezo electric ceramics with electrodes in combination with structural layers, ranging from single to multi-layered actuators. The bending of the actuator tip is achieved by generation of strain along the bending phase which leads to a bending moment, thus, translating the small deformation of the piezo electric material into a large deflection.

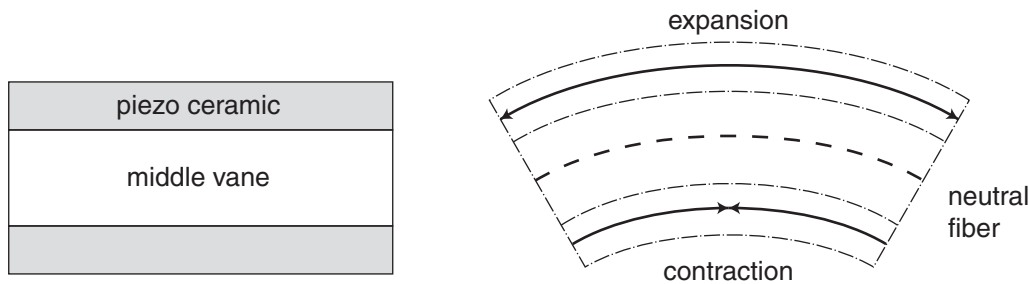


Figure 5.3.: Sketch of a double-layered piezo bending element (*left*) and its mode of operation with applied voltage (*right*).

The common representation for the deflection of a bending element is

(Kroupa and Nejezchleb [1998], Lim et al. [2001])

$$\frac{s}{X} = \frac{U}{U_X} - \frac{F}{F_B}, \quad (5.17)$$

with the blocking force F_B and free deflection X at the maximum voltage U_{\max} , and s is the deflection depending on the applied voltage.

An analogous ad-hoc description (to handle piezo bending elements with a certain layer structure, see program code App. C.3) can be derived if we assume that the piezo ceramic layers are thin in contrast to the overall height of the layer structure. That means the field strength dependent elongation of the piezo ceramic actually causes a constant additional bending moment M_U (where the index U denotes the voltage dependence). With a force F applied on the end of the element the bending moments following (5.4) are $M_0 = M_U + Fl$ and $M_1 = M_U$ and we obtain

$$\frac{3Eh^3w}{4l^3} s = \left(F + \frac{M_U}{l}\right) + \frac{1}{2} \frac{M_U}{l} = F + \frac{3}{2} \frac{M_U}{l}, \quad (5.18)$$

with the width w and height h of the piezo bending element, and tip deflection s . If we further remove any layer structure dependent variable and regard the piezo electric moment as proportional to the applied voltage U we get the representation

$$s(F, U) = c_\varepsilon l^2 \cdot U - c_{EI} \frac{l^3}{w} \cdot F. \quad (5.19)$$

The constants c_{EI} and c_ε are arranged to be constant for a certain layer structure and relate to the free deflection X and blocking force F_B by

$$c_\varepsilon = \frac{1}{U_X} \frac{X}{l^2} \quad \text{and} \quad c_{EI} = \frac{X}{F_B} \frac{w}{l^3}. \quad (5.20)$$

The bending elements we used have a free deflection of 100 μm and a blocking force of 200mN for an element with a free length of 10mm and a width of 2mm in unipolar operation at the applied maximum voltage of 100V. This gives the required parameters for further calculations of $c_\varepsilon = 0.01\text{m}^{-1}\text{V}^{-1}$ and $c_{EI} = 1\text{m}^{-1}\text{N}^{-1}$.

The piezo layers have a specified voltage range of 0–100V. This range can, however, be extended to –24V before depolarization occurs in the piezo ceramic layers (according to the manufacturer). As these piezo bending elements have a parallel ceramic orientation we can reach the full bipolar deflection range by applying a bias voltage of 76V (this is causing an initial tension allowing the bending element to bent into both directions) which is depicted in Fig. 5.4.

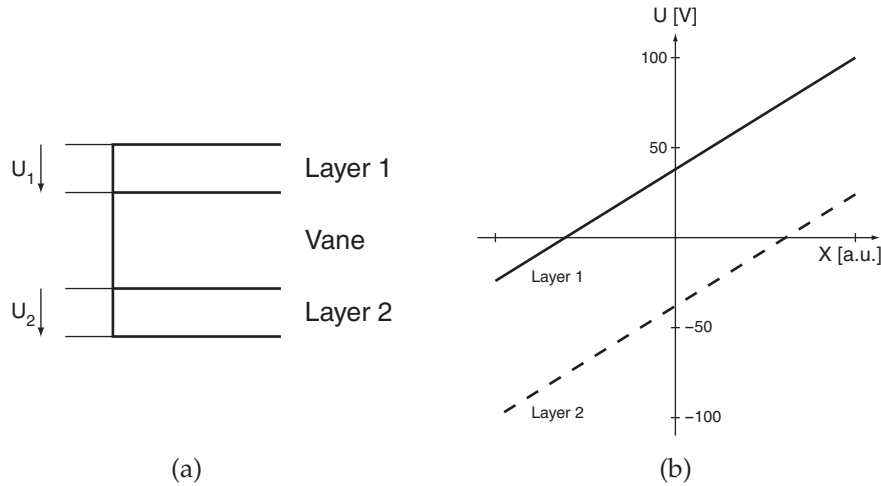


Figure 5.4.: Piezo bending element with a) parallel layer orientation and b) the corresponding potential, utilizing that the voltage range extends partially in the opposite direction before depolarization occurs.

The electronic drive was designed around a integrated high voltage amplifier (PA912, APEX) following the reference design (see App. A) with a symmetric high voltage power supply ($\pm 120\text{V}$, Schuricht, Germany). The bias voltage is generated with conventional Zener diodes. The amplification matches the signal output of the acquisition electronics, translating $\pm 10\text{V}$ into the piezo drive voltage of $\pm 62\text{V}$ with a bandwidth of 30kHz.

5.4. Scanner model

The primary mode of operation of the scanner is non-resonant and thus we developed a simple static model. The scanner itself is, however, not limited to non-resonant operation only, it should be well possible to use the scanner partially (one resonant axis) or completely (Lissajous type scanner Helmchen et al. [2001]) resonant.

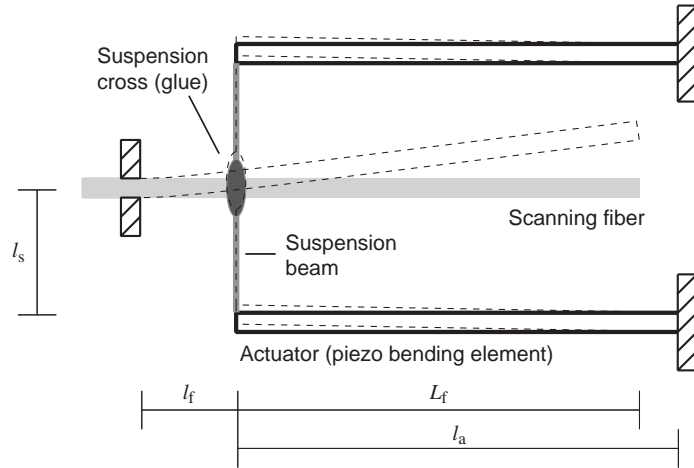
The operational scheme of the scanner is lever action, translating the small movement of the actuator, a piezo bending element, into a large deflection D at the excitation fiber tip:

$$D = \varphi \cdot L_f + s, \quad (5.21)$$

with s and φ the deflection and angle at the suspension and L_f the free fiber length (see Fig. 5.5).

The different modes of bending already formulated in section 5.1 will now be combined to yield a simple static model of the scanner. To differentiate the properties of each element, indices for the excitation fiber (f), the suspension (s) and the actuator (a) are added. In all cases s and φ will refer to the deflection and slope of the excitation fiber at the suspension cross, yielding the fiber tip deflection $D = s + \varphi L_f$ with the free length L_f of the excitation fiber (see Fig. 5.5).

Figure 5.5: Basic operation of the PLFS: a small deflection by the actuators is translated into a large fiber tip deflection. Also shown are lengths used to describe the scanner model.



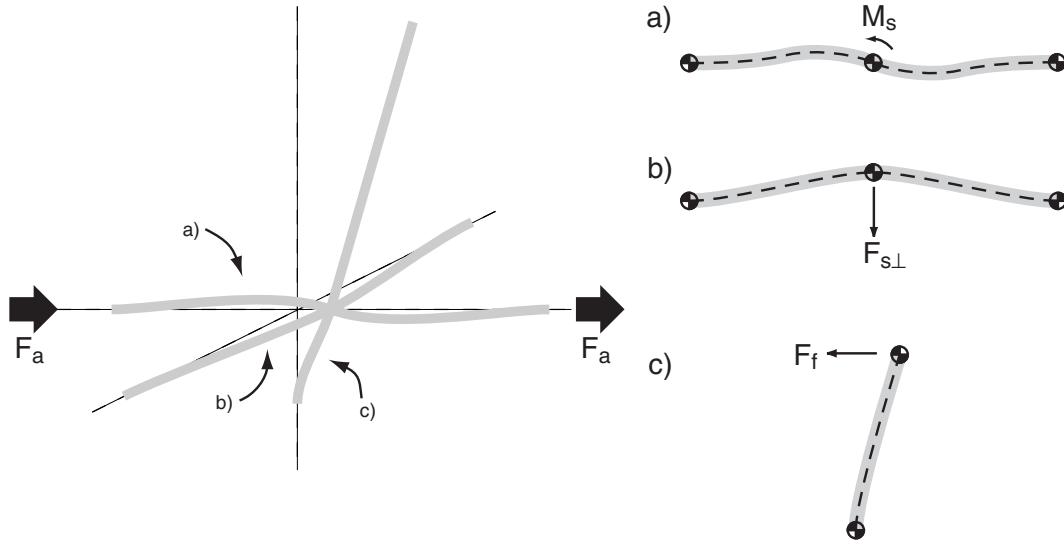


Figure 5.6.: Different types of bending, a) the suspension beam parallel and b) orthogonal to the applied force and c) bending of excitation fiber itself. The indices of forces and momentum stand for a, actuator and s, suspension and f, excitation fiber.

The moment created by the fibers (Fig. 5.6a) and (Fig. 5.6b) can be written as

$$M_s = -\varphi \cdot 4K'_s l_s \quad \text{with} \quad K'_s = \frac{(2E_s + G_s)I_s}{l_s^2} \quad (5.22)$$

with the distance l_s from actuator to the excitation fiber, the elastic and torsion module E_s and G_s and the area moment of inertia I_s . The retracting force created by the perpendicular suspension beam is

$$F_{s\perp} = s \cdot 4K_s \quad \text{with} \quad K_s = \frac{3E_s I_s}{l_s^3}. \quad (5.23)$$

To describe the bending of the excitation fiber we have to handle the effect

of the moments created by the suspension beams and write

$$F - \frac{M}{l_f} = -\varphi \cdot K'_f \quad \text{with} \quad K'_f = \frac{2E_f I_f}{l_f^2} \quad (5.24)$$

and

$$F - \frac{1}{2} \frac{M}{l_f} = -s \cdot K_f \quad \text{with} \quad K_f = \frac{3E_f I_f}{l_f^3}. \quad (5.25)$$

To eliminate the mixed dependency of deflection s and angle φ , we compare (5.22) with (5.24), this yields

$$F_f = \varphi \left(K'_f + 4 \frac{l_s}{l_f} K'_s \right) \quad (5.26)$$

and we get

$$\frac{s}{\varphi} = \frac{K'_f}{K_f} + 2 \frac{l_s}{l_f} \frac{K'_s}{K_f}. \quad (5.27)$$

With the equilibrium condition $F_f + F_{s\perp} + F_a = 0$ and the simple linear description of the piezo bending element (Sec. 5.3)

$$F_a = -s \cdot K_a + U \cdot K_U \quad \text{with} \quad K_a = \frac{1}{c_{EI}} \frac{w_a}{l_a^3}, \quad K_U = \frac{c_\varepsilon}{c_{EI}} \frac{w_a}{l_a}. \quad (5.28)$$

we get the deflection at the suspension cross in dependence of the applied voltage U

$$s = U \cdot \frac{2K_U}{K_f \xi + 4K_s + 2K_a} \quad \text{with} \quad \xi = \frac{K'_f + 4 \frac{l_s}{l_f} K'_s}{K'_f + 2 \frac{l_s}{l_f} K'_s}. \quad (5.29)$$

With (5.27) we can now calculate the deflection of the fiber tip given in (5.21).

This model includes a few assumptions we have to consider for optimizing the scanner properties. First, the connection between the suspension beams

and the excitation fiber is not completely rigid as we use UV-curing epoxy glue. Second, the bending of the beam parallel to the applied force (Fig. 5.6b) does not handle the yielding of the piezo bending actuators. Therefore, we additionally calculate the upper limit by ignoring the elastic properties of the suspension beam ($K_s = K'_s = 0$).

5.5. Results

The results of the model described in the previous sections (for program code see App. C.3) can be seen in Fig. 5.7 to 5.10. In addition, the maximal relation between stress and stress limit (bending, yield and buckling strength) is calculated and given as safety factor.

When comparing the calculations for the default piezo bending elements we used (see Sec. 6.3, $10 \times 2\text{mm}^2$, Fig. 5.7-5.9), it is obvious that reducing the diameter of the cross-connects increases the fiber deflection (here we consider the case of a rigid joint between the scan fiber and the cross-connects). While the change from a cross-connect diameter from $80\mu\text{m}$ to $60\mu\text{m}$ promises an increased deflection of about 30%, another $20\mu\text{m}$ diameter reduction only promises an improvement of about 15%. There, however, at a cross-connect diameter of about $40\mu\text{m}$ the stress limits are reached (compare Fig. 5.9).

From Fig. 5.9 it can be seen, that the maximal expected improvement of the deflection of the current scanner concerning the cross-connects would be 20%. Using different kinds of materials or geometries will require a careful selection and, especially near the stress limits, the fatigue failure will have to be considered.

Another possibility to increase the deflection is to increase the performance of the piezo bending elements, for example by using multi-layer bending actuators, or by simply increasing their size. An increase of 40% in length of the used piezo bending elements could lead to an increased deflection of over 30%. The current implementation of the head-mount microscope, however, would have to be changed (compare Fig. 6.1(a)).

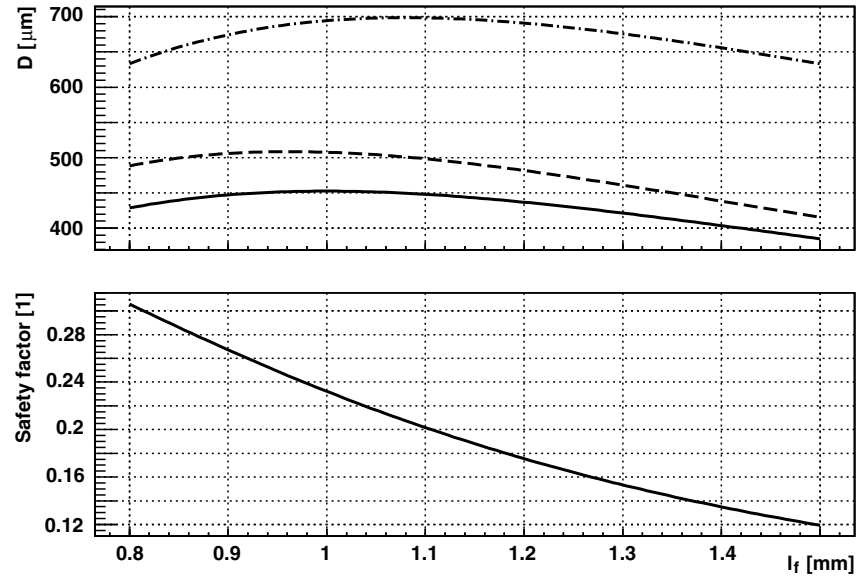


Figure 5.7.: Results of the calculation of the deflection D and the safety factor (see text for further details) versus the attachment point l_f for a default piezo element size ($10 \times 20\text{mm}^2$), scan fiber diameter $125\mu\text{m}$ and overall length 12.7mm , and cross-connect diameter $80\mu\text{m}$: (*dot-dashed*) maximum deflection without considering the cross-connects, (*dashed*) loose and (*solid*) rigid joint between the cross-connects and the scan fiber.

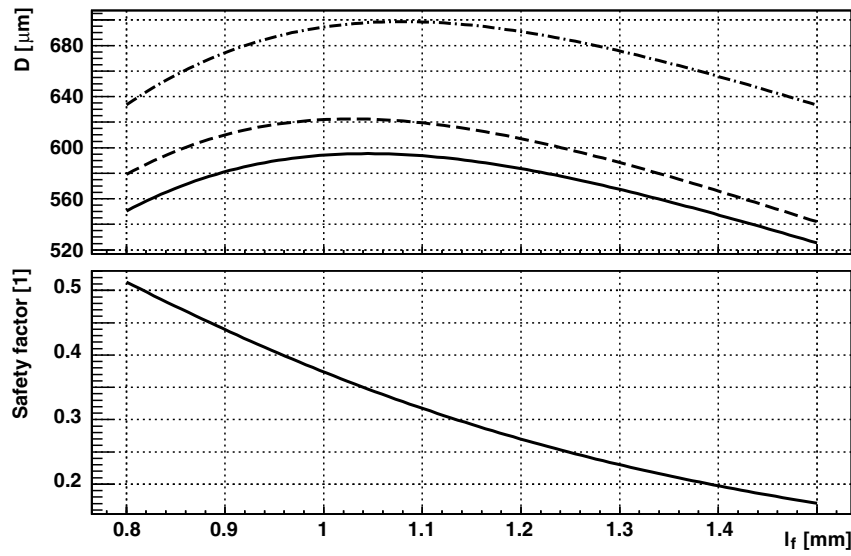


Figure 5.8.: Results for a cross-connect diameter of $60\mu\text{m}$ (compare Fig. 5.7).

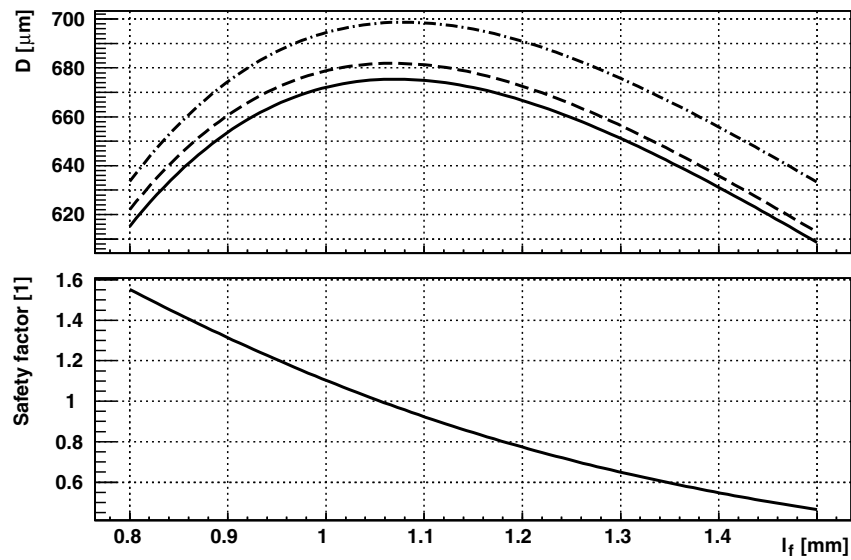


Figure 5.9.: Results for a cross-connect diameter of $40\mu\text{m}$ near the stress limits of the cross-connects.

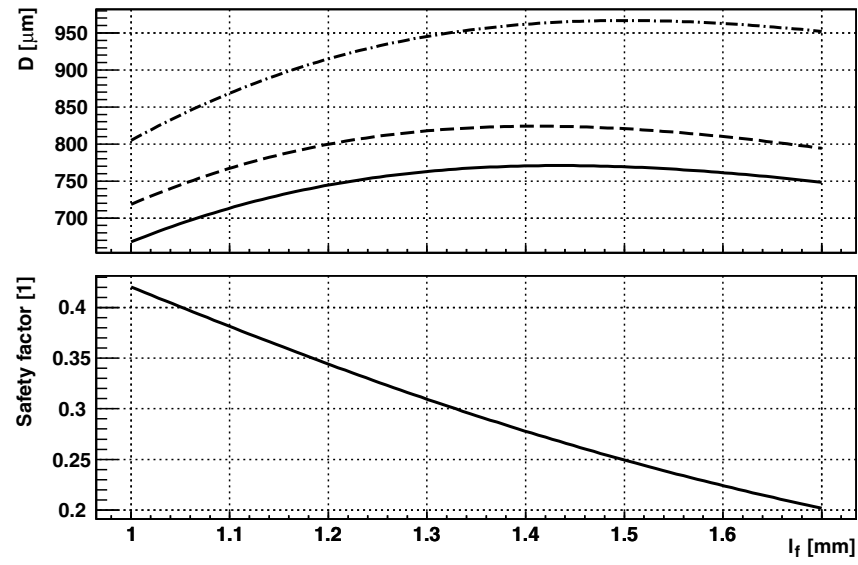


Figure 5.10.: Results for a cross-connect diameter of $60\mu\text{m}$ (compare Fig. 5.8) and a 40% larger piezo bending element.

6. A random access miniature fiber scanner for in vivo optical imaging

Multi-photon imaging allows the real-time analysis in living tissue explants and in vivo, and has become a powerful tool for neural activity analysis. Miniaturized multi-photon laser scanning microscopy promises to extend such measurements to awake, freely moving animals. In this chapter we present and demonstrate the piezo lever fiber scanner (PLFS)—an improved fiber scanning method that, in particular, allows the selection of an image offset and offers the prospect of random access scanning. Applications to intravital microscopy and endoscopy are envisioned.

6.1. Introduction

Multi-photon microscopy (MPM, Denk et al. [1990]) has become an important tool in live-science imaging, especially to acquire high-resolution images deep inside strongly scattering samples, such as neuronal tissue (Svoboda et al. [1997]). MPM is used to measure anatomical features and, in combination with functional dyes, neuronal activity from cell populations (Ohki et al. [2005], Helmchen and Waters [2002]) on the one hand, and down to small compartments of single nerve cells (Denk et al. [1994], Helmchen and Denk [2002], Jung et al. [2004]) on the other hand. Opto-physiological measurements are possible in vivo in anesthetized animals (Waters et al. [2003]); however, anesthetics are known to dramatically alter the functional state of the brain (Cotillon-Williams and Edeline [2003]). In order to examine brain function during natural behavior, it is necessary to image in awake animals. Pioneering experiments in awake animals were performed with in head-restrained animals (Fà et al. [2003]); measurements in awake and freely moving animals by means of optical imaging were carried out

with fiber bundles (Knittel et al. [2001] or fiber tip scanning, such as in the head-mounted resonant fiber scanner (Helmchen et al. [2001]).

High spatial resolution in the sub-micron range (which is essential when connectivity, which plays a major role, for example in consolidation of memory, and, therefore, small compartments such as spines should be detected) is, however, only possible with continuous scan techniques such as micro-mirrors or fiber tip scanning (for a review see Helmchen [2002]).

Using a single-mode fiber directly for scanning is a very simple and elegant solution. The predecessor of the PLFS uses the Lissajous scanning technique (i.e. the fiber tip follows a two-dimensional Lissajou figure pattern, see Helmchen et al. [2001]). As such it lacks control over the x - y -position and thus of the image center (panning) and scan pattern orientation (rotation). Panning capabilities are needed if particular structures, such as dendritic branches, are to be targeted. For a resonant Lissajous scanner this means the incorporation of an additional remotely controllable lateral translation mechanism.

Here we report the design, implementation, and testing of the PLFS. We can show that large deflections of the fiber tip are possible ($\pm 500\mu\text{m}$) far from resonances and, therefore, are able to demonstrate panning as well as rotation of the scan pattern. We also present and describe the integration of the scanner into a lightweight miniaturized head-mount microscope. With this microscope we obtain imaging results, tested on slices, that are practically comparable in all respect with the standard two-photon laser scanning microscopes. This microscope should, therefore, allow measuring in freely moving animals, especially in rats.

6.2. Theoretical framework

6.2.1. Design and limitations of a piezoelectric scanner

For a miniature MPM the scanner needs to: 1) have a sufficient 2-dimensional deflection range (field of view, FOV), 2) sufficient speed of deflection (scan speed) and 3) low weight and size. While simplicity is not a general

requirement we favored the direct fiber scanning technique over more complex designs like micro-electromechanical systems (Xie et al. [2003]). The scan speed and FOV are competing requirements (as with most scanning methods) since a longer fiber, as is needed for larger deflections, will always have a lower scan speed due to its resonance frequency.

The resonance frequency of a fiber of the length L_f (Fig. 6.1(b), free fiber end) is for a circular cross-section with diameter d the resonance frequency is thus approximately $\nu_1 \approx 0.14 \cdot d/L_f^2 \sqrt{E/\rho}$ (the second and third order resonance frequencies are $\nu_2 = 6.27\nu_1$ and $\nu_3 = 17.57\nu_1$, compare Fig. 6.4(a), see Sec. 5.1.2). If we assume a resonant limit on ν_1 of 500Hz allowing a line-scan period of 2ms (1ms for bidirectional scanning) the length of the fiber is limited to 14mm when using a standard 125 μ m single-mode fiber (fused silica: $E = 73 \cdot 10^9 \text{ N/mm}^2$, $\rho = 2.2 \cdot 10^3 \text{ kg/m}^3$, Wang et al. [2001]). Reducing the fiber diameter reduces the resonance frequency but would also allow larger deflections for the same applied force (see below).

To drive deflection we chose piezoelectric bending elements. Other possible types of actuators would include electrostatic and electromagnetic deflection. While electrostatic deflection is problematic due to its high voltage requirements, electromagnetic deflection would possibly require specifically designed coils and magnets or deposition of a highly permeable material on the fiber. Piezoelectric elements, in contrast, are simple and readily available. However, while piezoelectric elements are fast, light, and efficient transducers of electrical into mechanical energy, they do not provide large displacements. To translate the piezoelectric displacement efficiently into fiber deflection we, therefore, used a double lever arrangement (see Fig. 6.1) with the bimorph principle providing the first stage (here, 'bi' refers to two piezo ceramic layers including surface electrodes separated by a vane, see e.g. Kroupa and Nejezchleb [1998], bending elements with single or multiple layers are called unimorph or multi-morph, respectively). The second stage of motion amplification is provided by connecting the moving end of the bimorph to the fiber at a point close to the fibers anchor.

In order to optimize the deflection for a given free fiber length the mechanical impedances must be matched. The mechanical impedances (stiffness) of the fiber, of course, strongly depends on how far the fiber from the anchor point is pushed or pulled. An additional factor, which is considered in Sec. 5, is

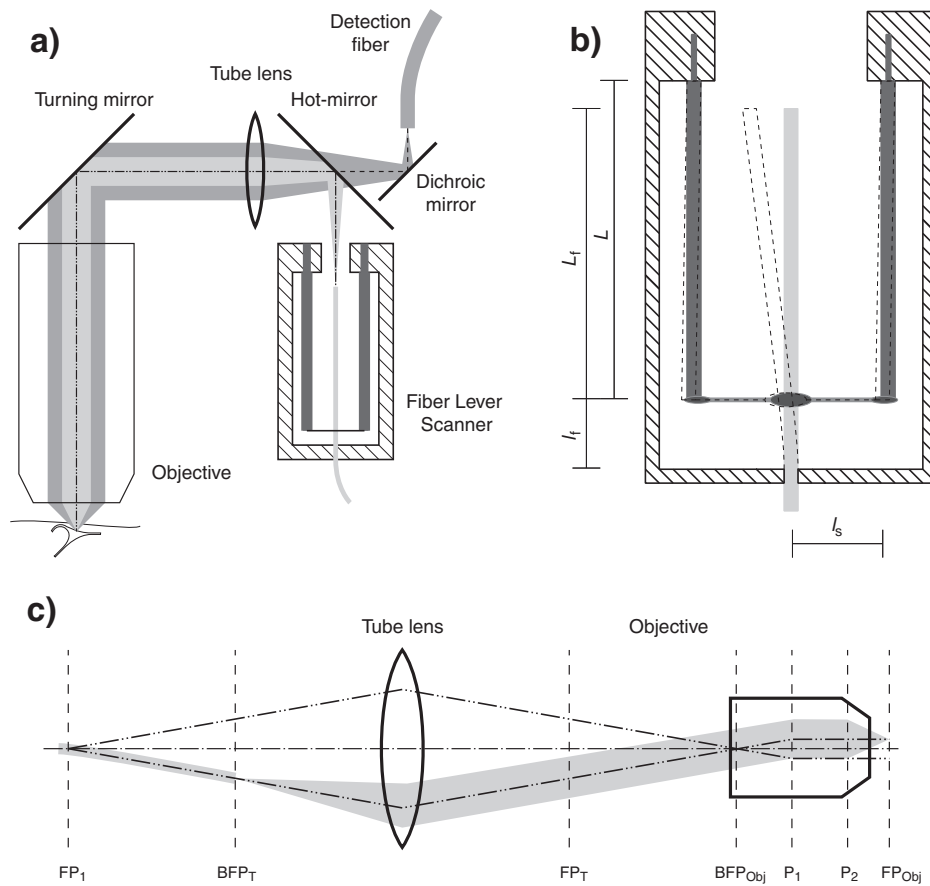


Figure 6.1.: Design overview: a) Sketch of the head-mount microscope with scanner, lenses, mirrors and light path of the excitation (*light gray*) and fluorescence (*dark gray*). b) semi-technical cross-section of the piezo lever fiber scanner (PLFS), showing deflection of the scan respective excitation fiber (*dashed*) and c) view of the flattened excitation path with focal (FB), backfocal (BFP) as well as principle planes (P) of the fiber tip, tube lens and objective (*left to right*).

the stiffness contributed by the elements connecting the bimorph ends to the fiber.

We first note that the deflection D of the fiber tip is maximal if the angle with

which the fiber leaves the attachment point is maximized. Independent of the free fiber length L_f (see Fig 6.1), as long as the lever ratio can be assumed to be large this is:

$$D_{\max} = s + \varphi \cdot L_f \approx \varphi \cdot L_f, \quad (6.1)$$

with the displacement s and angle φ of the fiber at the attachment point.

The maximum deflection is reached for (see Sec. 5):

$$\varphi = \frac{3F_B l_f^2}{3EI + 2(F_B X^{-1}) l_f^3}, \quad (6.2)$$

with the blocking force F_B and free deflection X of the actuator, attachment point distance l_f , and modulus of elasticity E and area moment of inertia I of the excitation fiber. As a function of l_f the deflection will be maximal at $l_f = (3EI/F_B X^{-1})^{-1/3}$. For our typical piezo element (with $F_B = 100\text{mN}$ and $X = 50\mu\text{m}$ in bipolar operation) the optimal attachment point is $l_f = 1.1\text{mm}$, for which we would expect $\pm 0.63\text{mm}$ of tip deflection for a free fiber length of 14mm .

This calculation so far ignores the stiffness due to the necessary connects. The model that includes the cross connect impedances was described in detail in Sec. 5. This model shows that fused silica seems to be a very good choice, both, concerning the material properties as well as the availability. However, a more thorough study of other materials (for example carbon and sapphire fibers) might also have to take fatigue into account.

6.2.2. Optical considerations

The optical design of an head-mount microscope also faces conflicting requirements: for a given fiber-tip deflection the total FOV of the system is inversely related to the resolution (focus size). For small structures, in particular, the signal intensity also depends on the focus size due to dependence of two-photon absorption on the square of the light intensity.

To reach sub-micron resolution the numerical aperture (NA) of the excitation ($\text{NA}_{\text{ex}} \approx 2\lambda/\pi d_0 \cdot p^{-0.5}$, with fluorescence spot diameter d_0 for p -photon

excitation) must be above 0.4 for two-photon excitation around 900nm central wavelength. With the NA of the excitation fiber of 0.12 the demagnification of the system thus should be larger than $m^{-1} = \text{NA}_{\text{ex}}/\text{NA}_{\text{f}} = 3.3$.

The simplest optical design of a microscope with an infinity-corrected objective involves two elements: the objective and the tube lens (Fig. 6.1c). The first, obvious, requirement is that the fiber tip needs to be in the back focal plane (BFP) of the tube lens to ensure that the excitation light enters the objective as a collimated beam (image at infinity). Another requirement is, however, that the beam does not move laterally in the objective's BFP. In a conventional laser scanning microscope this is achieved by imaging the scan mirrors into the objective's BFP. For a fiber scanner the equivalent condition is that the "illumination" aperture be imaged into the BFP. The illumination aperture is a (possibly imaginary) aperture where the beam does tilt but does not move laterally, which for the PLFS is located between the anchor point and the point where the fiber-bending force acts (FP_1 , see Fig. 6.1c). This condition is fulfilled if the distance between the illumination aperture and BFP of the tube lens as well as the distance from the FP of the tube lens to the objective's BFP are equal, which is the focal length f_t of the tube lens. The focal length f_t is determined by the required demagnification factor and the objective's focal length $f_t = f_{\text{Obj}} \cdot m^{-1}$, this in turn determines the fiber length $L_f + l_f \approx f_t$. For a given focal length $f_{\text{Obj}} = 3\text{mm}$ and a fiber length of 14mm we find a demagnification factor of $m^{-1} = 4.7$. The lower limit of $m^{-1} = 3.3$ would require a minimal fiber length of $\approx 10\text{mm}$.

In our actual design we have chosen a smaller distance between tube lens and objective to allow for a more compact mechanical design. As a result the beam moves laterally in the BFP as the fiber is scanned over the full range. Since the objective lens is still underfilled under our conditions this does not lead to a loss of resolution or excitation efficiency at the edges of the FOV but scanning is no longer telecentric in the object space (see Fig. 6.1c).

6.3. Materials and Methods

The scanner was built with piezo bending elements purchased from Argillon GmbH, Germany. We used a standard optics communication single-mode fiber (125 μm , FS-SN-4224, Newport). The suspension fiber (UV 50/60 P) was kindly provided by CeramOptec, Germany and the light curing epoxy glues (UV4601, UV2271) by Wellomer GmbH, Germany. The scanner enclosure (see Fig. 6.2) was built in two parts: the piezo bending element base and a thin metal cylinder holding the excitation fiber. The metal cylinder contained further holes (see also Fig. 6.3) for to glue and cure the cross connects onto the piezo bending element tip as well as the excitation fiber.

The piezo drivers were constructed using a high voltage integrated amplifier (PA912, APEX) and was designed to drive the center electrode of the bimorph with up to $\pm 62\text{V}$ while the outer surface electrodes were held at plus and minus 38V (see App. A, p. 70), respectively, yielding the full bidirectional deflection range.

The scanner was incorporated into a head-mounted microscope that contained (Fig. 6.3, in sequence starting above sample): a water immersion objective that was specifically designed for this purpose ($f' = 3\text{mm}$ in wa-

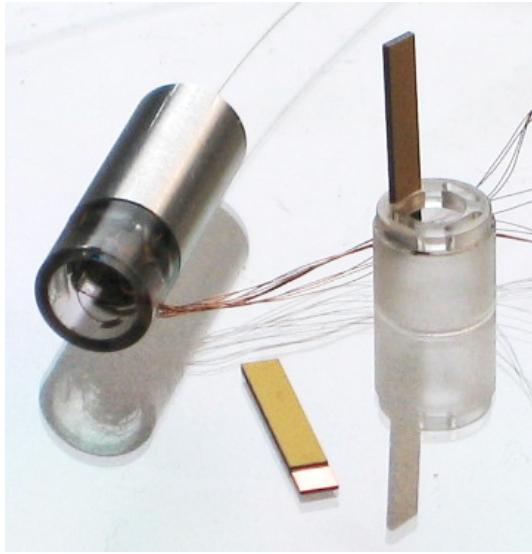
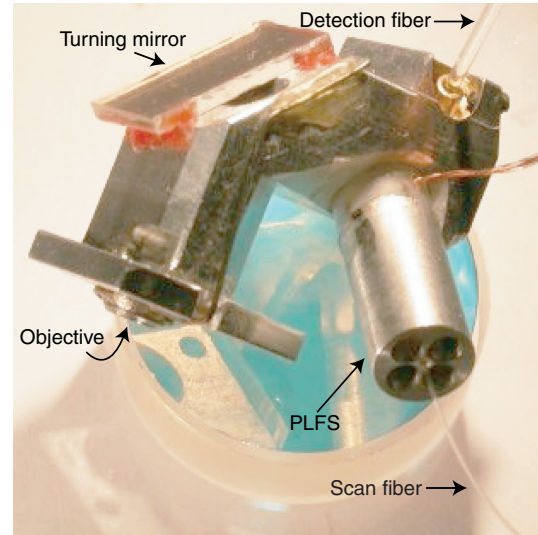


Figure 6.2: The assembled piezo lever fiber scanner (*left*) with the piezo bending element base (*right*) and piezo bending elements ($10 \times 2\text{mm}^2$, see text for further details).

Figure 6.3: Prototype of the assembled head-mount microscope with a 1" (25.4mm) diameter mirror serving as size reference (compare with Fig. 6.1).



ter with $n = 1.33$, Throl Optische Systeme, Germany), a folding mirror (SILFLEXTM, unaxis), an achromat as a tube lens ($f = 12.7\text{mm}$, LAKN22-SFL6, ThorLabs), a hot-mirror (Calflex-X, Linos) to reflect the infrared excitation laser light coming from the fiber scanner and transmit the fluorescence toward a turning mirror used to deflect the fluorescence into the detection fiber (1mm diameter plastic optical fiber, NA 0.63, PJU-FB1000, which was kindly provided by Toray Deutschland GmbH, Germany). The turning mirror was (but does not need to be) a cold-mirror (650DCRXU, Chroma Technology Corp.) that had a very high reflectivity for the fluorescence light.

Test samples contained $1\mu\text{m}$ fluorescent (FluoresBrite, Polysciences) and non-fluorescent beads (PolyBead, Polysciences) embedded in 0.5% and 1% agarose gel yielding a scattering length similar to brain tissue (Feierabend [2004]). To measure the point spread function 175nm diameter fluorescent beads (PS-Spec, Polysciences) were used.

Hippocampal organotypic rat brain slices (postnatal days P6-9) were prepared according to Refs. (Stoppini et al. [1991], Gahwiler et al. [1997]). To stain the slices they were either loaded with Oregon-Green 488 BAPTA-1, AM (Molecular Probes) diluted with culture medium and incubated for one to four hours at 37°C (Stosiek et al. [2003]) or infected with GFP adenovirus

(Michel et al. [2005]) (kindly provided by Mazahir T. Hasan).

The excitation source was the custom-built Ti:Sapphire laser as reported in Chap. 4. To compensate for dispersion in the fiber we used a multi-prism sequence (Duarte [2000a]) consisting of two arrays of 5 fused silica prisms each. After the tube lens we could deliver pulses with a width of 180fs at 200mW average power (currently incomplete GVD compensation, limited by the size of the prisms) measured, respectively, with a auto-correlator (PulseScope, APE, Germany) and a pyro-electric detector (D10MM, Thor-Labs).

To measure the deflection of the focal spot we used a position sensitive detector (PSD) (2L4SP, SiTek) amplified with a custom built logarithmic differential amplifier (OPA2277, BurrBrown with BCM8465, Infineon). The signal was fed into a spectrum analyzer (HP35650A, 51B, 52B, 53A, 56A, Hewlett-Packard) to measure the fiber resonances and an oscilloscope to observe the hysteresis.

The scan generation, fluorescence detection, and data acquisition systems were from a conventional custom-built multi-photon laser scanning microscope. It consists of a control software (CfNT, Müller [2000-2005]) on computers equipped with a frame grabber (XPG1000, Dipix) and a signal processor (Fulcrum DT3801, Data Translation). An external interface electronic (Tritthardt [2005]) synchronizes signals and interfaces with the detection devices (currently either PMTs or APDs) and the galvanometer scanners. The ramp-shaped scan signal was low-pass filtered (Frequency Devices 900) at about 200–400Hz depending on the scan speed (5–10ms per line). Best results were achieved for 7ms line scan period and a filter cut-off frequency of 200Hz.

The optical components (objective, tube lens, scanner and mirrors) weigh approximately 3g. The aluminum housing of the prototype weighs about 7g, however, the complete CAD design involves removal of several edges and thus we expect to reach a weight of the complete microscope below 8g.

6.4. Results

After building the scanner (with a total fiber length of 12.7mm, the attachment distance is currently $l_f = 1.3\text{mm}$, compare Fig. 5.8), we characterize the scanner and compare it with the optimizations discussed above. The deflection could be estimated by directing the beam of the microscope (objective removed) against a screen and driving the scanner with a slow sinusoidal waveform. We found a fiber tip deflection of $\pm 0.55\text{mm}$. The expected values were between $\pm 0.68\text{mm}$ (ignoring the impedance of the cross connects) and $\pm 0.57\text{mm}$ (assuming a completely rigid cross-connection joint). The measured deflection corresponds to a FOV of $260\mu\text{m}$, imaging experiments show a FOV of $245\mu\text{m}$ due to low-pass filtering of the scan signal.

The resonance frequencies along the two axes were 783 and 790Hz (Fig. 6.4) corresponding to a calculated free length of 11.34 and 11.40mm, respectively, with the difference matching the diameter ($60\mu\text{m}$) of the cross-connect fibers.

Because of the high quality factor (> 200) of the fiber resonances (Fig. 6.4), they are easily excited by spurious driving forces near those resonances. Accordingly we found strong resonance effects in the images (Fig. 6.5). Surprisingly, even higher-order low-pass filtering of the ramp-shaped driver signal did not completely suppress excitation of the fiber resonances. A likely explanation is that non-linearities, for example the hysteresis of the piezoelectric material (Fig. 6.6), regenerate frequency components beyond the filter cut-offs. Additional problems may arise also from defects in the piezo bending elements and the connections between the fibers we experienced in earlier prototypes (an overloaded piezo bending elements as well as insufficient adhesion at the glue points lead to jerky movement). By careful selection of filter frequency and scan speed we could minimize resonance effects. In future implementations it might be possible to suppress resonances actively (see Tan et al. [1999]). One side-effect of low-pass filtering the drive signal is, of course, a slow turn-around with the corresponding appearance of “image-stretch effects” (Fig. 6.5).

On the main advantages of the PLFS is the ability to pan and rotate the scan pattern. The pan-capability of the scanner is demonstrated as a small FOV was scanned at different offsets relative to the center position (Fig. 6.7, see

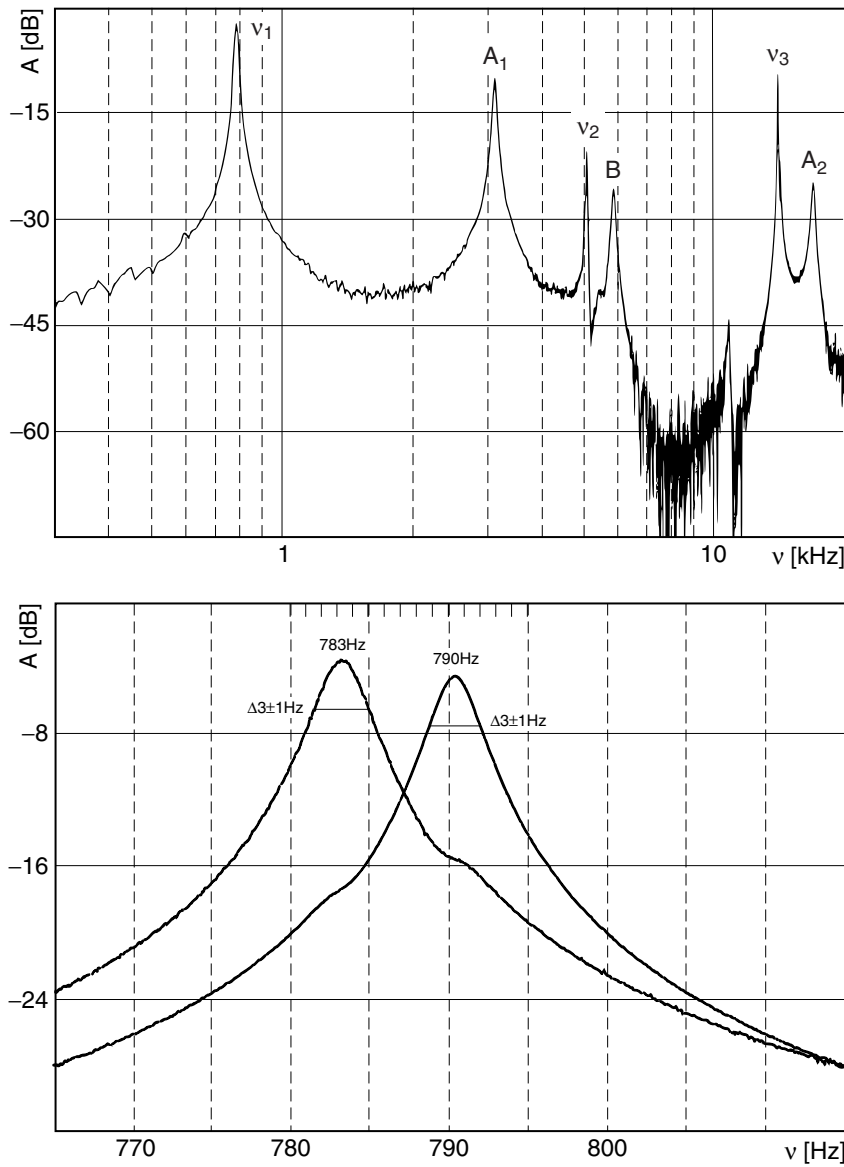


Figure 6.4.: Frequency response of the scanner: (*Top*) spectrum of one axis, the peaks at 800Hz, 5kHz and 14kHz (ν_1 to ν_3) are the resonances of the free fiber end. The resonance A and B possibly relate to piezo and cross-connect resonances, respectively (A_2 fits the second order resonance frequency of A_1). (*Bottom*) superimposed responses to driving the x and y piezo's, respectively. (Image was reproduced from spectrum analyzer hardcopy Selinger [v1.7].)

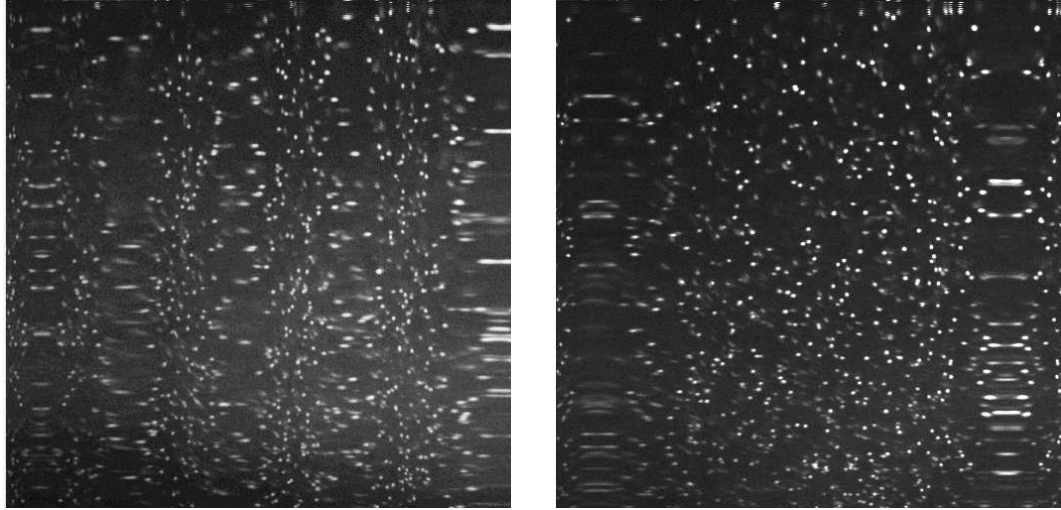


Figure 6.5.: Initial test on fluorescent beads embedded in agarose reveal image distortions: (*Left*) The image shows resonances of the fiber (the central stretches are about 1.2ms apart which is near the resonance frequency of 800Hz). (*Right*) By low-pass filtering of the ramp-shaped driver signal the resonances disappear, however, the turning points of the fiber appear as stretches in the image.

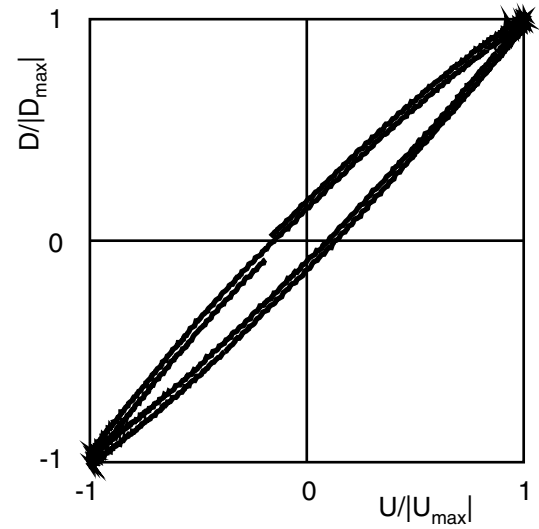


Figure 6.6: Hysteresis of the PLFS recorded with the PSD in the object plane. The small horizontal shift is caused by fluctuations in the laser due to incomplete compensation of the intensity in the custom-built logarithmic differential amplifier.

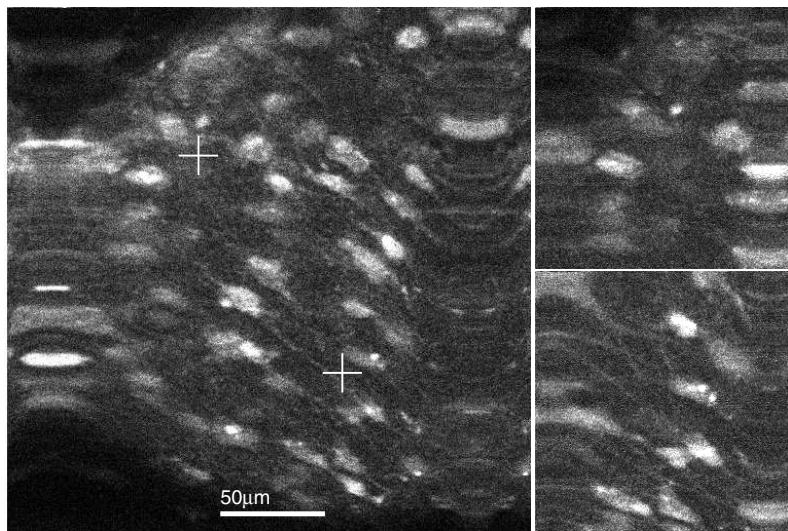


Figure 6.7.: Scanning at an offset position. Shown are neurons at a depth of $40\mu\text{m}$ in cultured brain slices that had been bulk loaded with Oregon Green (AM), imaged with 80mW average laser power after objective and averaging of 5 images. The image (left, 100% scan range, 512 pixels) show two offset positions of an image sequence (right, 50% scan range, 256 pixels) recorded by manually adding an offset voltage to the scanner signal.

also Fig. A.1): At first a reference image was taken at the full FOV. The scan voltage is then reduced to 50% ($\pm 31\text{V}$) and an image sequence was recorded as the offset voltage was manually varied by $\pm 15\text{V}$. The capability to rotate the FOV is demonstrated on a probe of fluorescent beads (Fig. 6.8).

To test the repeatability of offset scan positions we alternated the offset every 5s between points corresponding to $\pm 25\%$ of the FOV while recording an image sequence (25% field of view with 64×64 pixels, 7ms per line) over several minutes. While the offset jump excites resonances that strongly distort a single frame following each jump the respective offset positions appear stable (see Fig. A.2).

We finally determined the resolution of the microscope. From the optical parameters ($\text{NA} = 0.9$, $\lambda = 900\text{nm}$) we expect a resolution ($1/e^2$) of $0.8\mu\text{m}$.

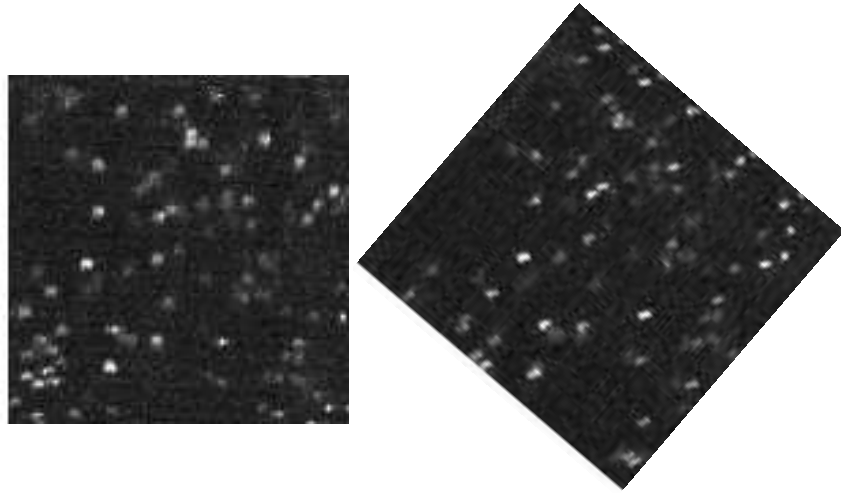


Figure 6.8.: Demonstration of pivoting of the field of view (*left: 0°*, *right: 45°*) with fluorescent beads embedded in agarose.

Experimentally we have measured a spot width of $0.9\mu\text{m}$ with 175nm fluorescent beads (Fig 6.9) which is close to the theoretical value. The practical optical resolution of the PLFS in the head-mount scanner is also nicely demonstrated in Fig. 6.10 which shows spine like protrusions in hippocampal organotypic slices expressing GFP in neurons.

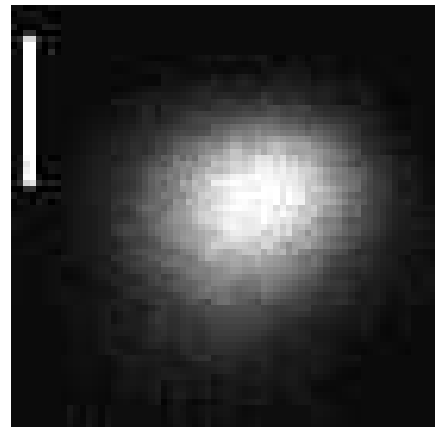


Figure 6.9: Pane of an image of a single 175nm fluorescent bead to measure the resolution (scale bar is $1\mu\text{m}$).

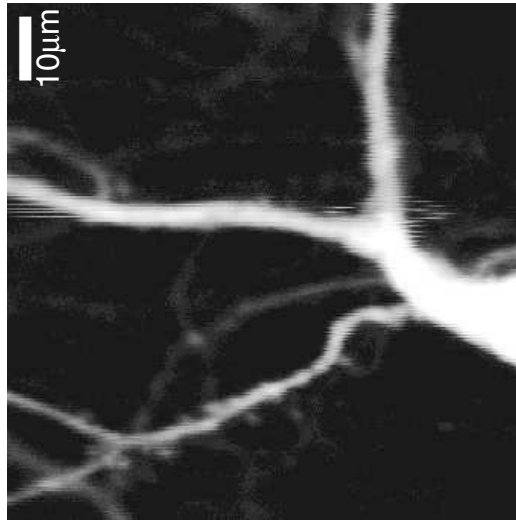


Figure 6.10.: GFP expression in neurons from organotypic hippocampal slices.

6.5. Discussion

We have shown that a piezo-electrically driven fiber scanner, which we call PLFS, can combine compact geometry, high scan speeds, and random access capabilities. We have also shown that in combination with a miniaturized microscope objective high resolution images can be recorded from inside biological tissue. In combination with in vivo loading of neuronal cells with synthetic and genetically-encoded calcium and voltage indicators neural activity measurement in freely-moving mammals will enable the study of brain function while the brain is performing it's genuine purpose: the control of movement.

Improvements of the scanner seem possible, for example by reducing the stiffness of the cross-connection elements, which in the current design contribute about 15% of the total stiffness. From the simulation it appears, however, that this contribution cannot be reduced to below 5% due to the material stress limits.

A different approach to increase the deflection is to use piezo bending

elements with higher deflections. For example when using 40% longer bending elements the deflection could be increased by about 30% (compare Sec. 5). Then, however, it would not be possible to keep the design of the head-mount microscope: the excitation and fluorescence path would have to be split before the tube lens (see Fig. 6.1a, distance from fiber tip to tube lens would decrease with increasing length of the bending elements).

While fiber resonances limit the generation of standard saw-tooth scan patterns to well below the fundamental resonance it might be possible to combine a Lissajou scan pattern, using either the fundamental or even a higher order resonance, with the pan capability of the PLFS. A mixture of static and resonant scanning will, however, require an adaption of the software.

With regard to imaging in freely moving animals, however, further questions have to be addressed. This is mainly the twisting of the fibers due to movement of the animal as well as pulsation, respiration or in general movement artifacts.

While twisting of fibers can be solved externally (either technically with a rotatable fiber mount or by confining the movement of the animal, e.g. Y-maze) compensating movement artifacts will require a far more sophisticated approach which includes image stabilization on hardware and on software side possibly including fast depth control.

6.6. Conclusions

Combining the PLFS with a miniaturized microscope can be used to image in biological tissue. We envision that the scanner can be used also in the wider area of intravital microscopy.

A possible application is for example endoscopic coherence tomography (Aguirre et al. [2003]). Miniaturized scanning instruments are becoming increasingly important in human medicine (Tozer et al. [2005]) as well with applications from visualization of cellular morphology (Lippman and Dunaevsky [2005]) and physiology (Jung et al. [2004]) to monitoring of

therapeutic progress (Gumbleton and Stephens [2005]) and actual laser treatment (May et al. [2001]).

Part III.

Appendix

A. Supplemental information

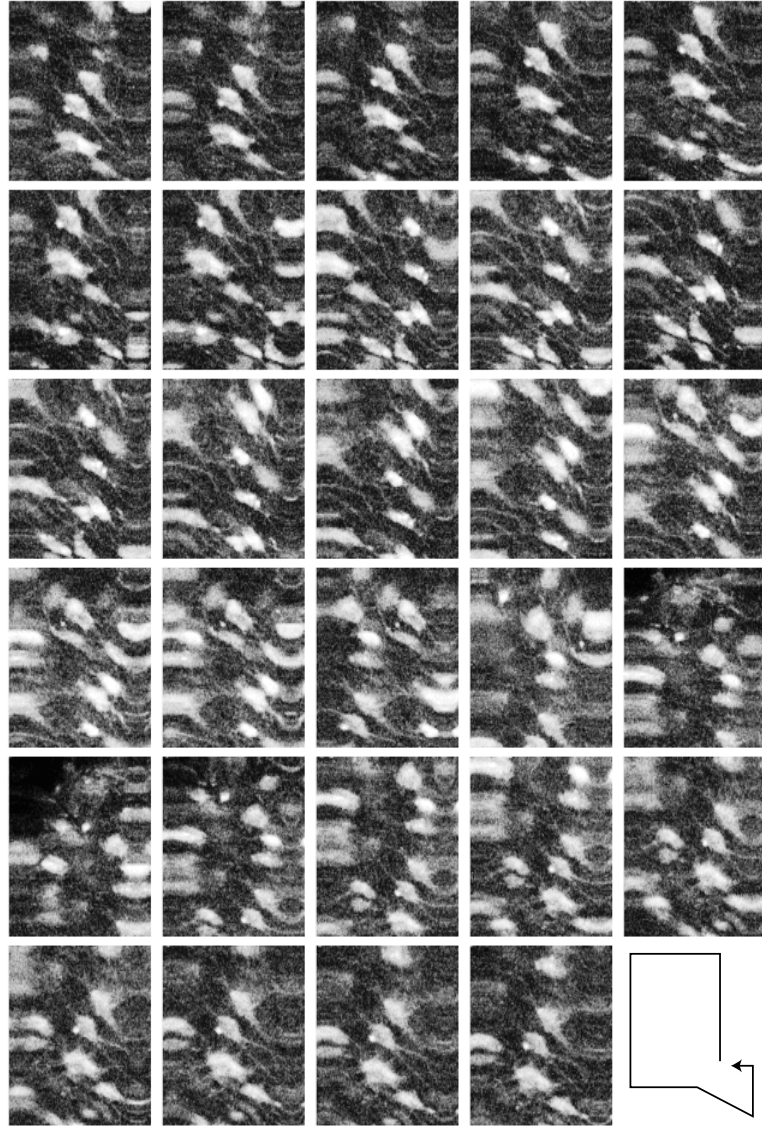


Figure A.1.: Scanning with offset (panning). The graphic shows every 4th image of a movie taken at a resolution of 256×256 pixels (50% scan voltage, 7ms per line) with manually varied offset voltage. In the lower-right corner the path is shown for clarification.

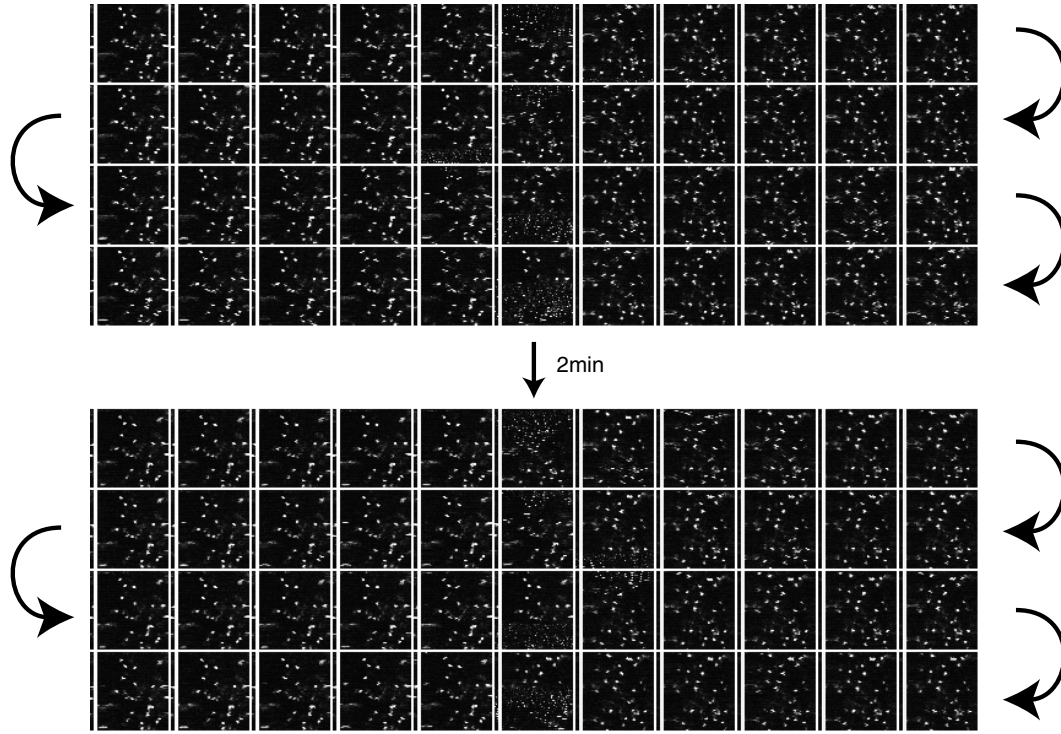


Figure A.2.: Selection of images from a 3.7min image sequence for testing stability of instantaneous offset change. The sequence was recorded at a resolution of 64×64 pixels (7ms per line) with 50% scan voltage. The offset jump (*middle row*) occurs every 10s (about every 23rd image) with 25% of the scan voltage.

B. Material constants

Table B.1.: Material elasticity properties: modulus of elasticity E , modulus of rigidity G , and density ρ .

Material	E [10^9 N/m^2]	G [10^9 N/m^2]	ρ [kg/m^3]
Fused silica	73	32	2,200
Steel	≈ 200		792
Carbon	50–230		1,100–2,200
Sapphire	335	148	3,970

Table B.2.: Material stress limits: yield strength σ_t and bending strength σ_b .

Material	σ_t [10^6 N/m^2]	σ_b [10^6 N/m^2]
Fused silica	50	4 500
Steel	500–1 000	500–1 500
Carbon	100–400	
Sapphire	300	450–690

Sources: (CRC [2003–2004]), (Han [1995]), (Vedam [1950]), (Wang et al. [2001]), (Ventures), (Kurki), SGL Carbon Group, Goodfellow, Meller Optics, Inc.

Table B.3.: Sellmeier coefficients for selected materials.

Material	A	B_i C_i
SiO ₂	1	0.6961663, 0.407942610, 0.8974794 0.00467914825849, 0.01351206307396, 97.934002537921
SF10	1	1.55912923, 0.284246288, 0.968841926 0.0121481001, 0.0534549042, 112.174809
SF14	1	1.69182538, 0.285919934, 1.12595145 0.0133151542, 0.0612647445, 118.405242
Ti:sapphire	1	1.431349, 0.6505471, 5.341402 0.005279926, 0.01423826, 325.0178
BK7	1	1.03961212, 0.231792344, 1.01046945 0.00600069867, 0.0200179144, 103.560653
FK5	1	1.036330719, 0.152107703, 0.913166269 0.0776227030 ² , 0.138959626 ² , 9.93162512 ²

Sources: Schott catalogue, (Han [1995])

C. Programs

C.1. Dispersion compensation

We have implemented two-dimensional ray-tracing with MATLAB (Math-Works) which is described in this section accompanied with parts of the code.

Refractive index: The refractive index is calculated as stated above based on the Sellmeier formula (3.1). Due to speed concerns the refractive index is pre-calculated for a wavelength range from 200 to 1600nm.

```
function n = refr_index_load(mat)
% n = refr_index_load(material_string)
%
% Return a structure containing Sellmeier coefficients and
% an array with precalculated values (refractive indices).
[A,B,C, nl] = load_opt_dat(mat);

n.coeff.A = A;
n.coeff.B = B;
n.coeff.C = C;
n.coeff.n = size(B,2);

n.precompute.bound.lower = 199e-9;
n.precompute.bound.higher = 1600e-9;
n.precompute.bound.step = 1e-9;

n.nonlinear = nl;

lambda = [n.precompute.bound.lower+n.precompute.bound.step:...
    n.precompute.bound.step:...
    n.precompute.bound.higher-n.precompute.bound.step];
nlambda = size(lambda,2);
ncoeff = size(B,2);
l_sqr = lambda.*lambda*1e12;
n_sqr(1:nlambda) = A;
for k = 1:ncoeff,
    n_sqr = n_sqr + (l_sqr * B(1,k))./(l_sqr-C(1,k));
end
n.precompute.values = sqrt(n_sqr);

return

function [a,b,c] = load_opt_dat(mat)
% Sellmeier coefficients for a few materials
if strcmp(mat, 'vacuum'),
    a = 1.0;
    b = [];
    c = [];
elseif strcmp(mat, 'SiO2'),
```

```

        a = 1.0;
        b = [0.6961663,          4.07942610e-1,          0.8974794];
        c = [0.00467914825849,  0.01351206307396,  97.934002537921];
    elseif strcmp(mat, 'SF10'),
        a = 1.0;
        b = [1.55912923,        2.84246288e-1,        9.68841926e-1];
        c = [1.21481001e-2,  5.34549042e-2,  1.12174809e2];
    elseif strcmp(mat, 'SF14'),
        a = 1.0;
        b = [1.69182538,  2.85919934e-1, 1.12595145];
        c = [1.33151542e-2, 6.12647445e-2, 1.18405242e2];
    elseif strcmp(mat, 'Ti:sapphire'),
        a = 1.0;
        b = [1.431349,  0.6505471, 5.341402];
        c = [0.005279926, 0.01423826, 325.0178];
    end
end

```

The actual calculation of the refractive index (`refr_index`) is then a simple matrix lookup. For convenience, the function can also calculate the refractive index for an arbitrary wavelength.

```

function n = refr_index(def, lambda)
% n = refr_index(def, lambda)
%
% Return refractive index from structure def (as returned by refr_index_load):
% Either pre-calculated value or calculate with Sellmeier

idx = floor((lambda-def.precompute.bound.lower)/def.precompute.bound.step);
precomp = 1;

if idx < 1,
    precomp = 0;
end

if lambda-def.precompute.bound.lower ~= idx * def.precompute.bound.step,
    precomp = 0;
end

if precomp,
    n = def.precompute.values(idx);
else
    l_sqr = lambda.*lambda*1e12;
    n_sqr(1:size(lambda,2)) = def.coeff.A;
    for k = 1:def.coeff.n,
        n_sqr = n_sqr + (l_sqr * def.coeff.B(1,k))./(l_sqr-def.coeff.C(1,k));
    end
    n = sqrt(n_sqr);
end
end

```

Tracing geometry: A beam is defined according to (3.4) by the helper function `beam_create` returning a structure containing the origin (`P`) and direction of the ray (`dir`). Additionally, the structure contains the wavelength (`lambda`) and the index of refraction (`index`) for later use with calculation of the optical path length:

```

function b = beam_create(P, dir, lambda, index)
b.P      = P;          % origin
b.dir    = dir/norm(dir); % normalized direction
b.lambda = lambda;      % wavelength

if nargin == 4,

```

```

    b.index = index;      % index of refraction
else
    b.index = 1.0;
end

```

Accordingly a helper function (`surface_create`) creates a structure for a optical surface with its edges A and B, the surface normal pointing to the outside (`normal`) and the material definitions as returned by `refr_index_load`:

```

function s = surface_create(normal, A, B, refr_incident, refr_transmit)
% s = surface_create(normal, A, B, refr_incident, refr_transmit)
s.normal = normal/norm(normal);
s.A      = A;
s.B      = B;
s.refr.incident = refr_incident;
s.refr.transmit = refr_transmit;

```

The central methods for ray-tracing according to previous section are the intersection calculation (`isect_surface_beam`) and the refraction of a beam (`refr_beam`). The latter functions returns a newly created beam. The optical path length can be calculated by summing up all distances between the origins of each beam evolving from a plane.

```

function [P, ecode] = isect_surface_beam(surface, beam)
% [P, ecode] = isect_surface_beam(surface, beam)
%
% Calculate point of intersection between beam and surface.
%
% Returns:
%   P      the intersection point
%   ecode   0 for ok
%           1 for parallel (caller has to check for identity on his own)
%          -1 for outside surface

sdir = surface.B-surface.A;

xy = sdir(1)*beam.dir(2);
yx = sdir(2)*beam.dir(1);

if xy == yx,
    P = [-1e999,-1e999];
    ecode = 1;
    return;
end

D = beam.P - surface.A;
t = (D(1)*beam.dir(2) - D(2)*beam.dir(1)) / (xy-yx);
norm(sdir);

P = surface.A+t*sdir;
if (t<0) | (t>1.0),
    ecode = -1;
else
    ecode = 0;
end

function [b, side, ecode] = refr_beam(beam, surface)
% [beam, side, ecode] = refr_beam(beam, surface)
%
% Calculate refraction of a beam at a surface.
%

```

```

% Returns:
%   b           the returned beam
%   side        1 - beam entered surface from outside
%              -1 - beam entered surface from inside
%   ecode       (see isect_surface_beam)
%              0 for ok
%              1 for parallel (caller has to check for identity on his own)
%              -1 for outside surface
%              -2 total reflection

[P, ecode] = isect_surface_beam(surface, beam);
if ecode == 1,
    % beam parallel to surface... dumped    b = beam_create([0 0], [0 1], 0);
    side = 0;
    return;
end

% which side of the surface are we?
i_perp_len = vecdot(beam.dir, surface.normal);
side = -sign(i_perp_len);

% disect incident beam (PERPpendicular and PARAllel)
i_perp = i_perp_len * surface.normal;
i_para = beam.dir - i_perp;

% calculate refractive index factor
n1 = refr_index(surface.refr.incident, beam.lambda);
n2 = refr_index(surface.refr.transmit, beam.lambda);
if side < 0,
    n = n2/n1;
else
    n = n1/n2;
end

% disect transmitted beam (PERPpendicular and PARAllel)
t_para = i_para * n;
t_para_abssqr = vecdot(t_para, t_para);

if t_para_abssqr > 1.0,
    % total reflection
    b = beam_create(P, [0 1], 0);
    side = 0;
    ecode = -2;
    return;
end

% Return a fresh beam with its origin at previous intersection
b = beam_create(P, t_para - side * surface.normal * sqrt(1-t_para_abssqr), beam.lambda);

```

The only optical element we are interested in is a prism, more precisely a sequence of prisms. The prism sequences are aligned in a way, so that if sequence A has counter clock wise orientation and sequence B vice versa, the output plane of sequence A is parallel to sequence B and the apexes of the last prism of A as well as the first prism of B are located at the coordinate origin (see Fig. C.3). This allows us to simply shift sequence B to align for a certain inter-prism distance.

```

function seq = seq_create(apex_angle_deg, height, ...
    refr_outer, refr_inner, ...
    number_of_prisms, design_wave_length, ...
    turn)
%seq = seq_create(apex_angle_deg, height, ...
%   refr_outer, refr_inner, ...
%   number_of_prisms, design_wave_len, ...
%   turn)

```

```

%
% Create a sequence of prisms with orientation:
%   turn      1 counter clock wise
%             -1 clock wise
%
% Returns
%   seq        The sequence of prisms (see seq_opt, calculation of optical path length)

if size(apex_angle_deg,2) > 1,
    error('Mixing of different prism materials not supported yet');
end

ang = deg2rad(apex_angle_deg);

% the "design wavelength" determines the relative orientation of the prisms,
% each prism is traversed at this wavelength at minimum deviation
seq.design.lambda = design_wave_length;
mdang = mindev(ang, ...
    refr_index(refr_outer, design_wave_length),...
    refr_index(refr_inner, design_wave_length));
seq.design.minimum_deviation_angle = rad2deg(mdang);
seq.design.number = number_of_prisms;

% input/output surface and orientation of the minimum deviation beam from apex.
% (pre-allocate for index access)
seq.input.P = [0 0];
seq.input.dir = [0 0];
seq.input.A = [0 0];
seq.input.B = [0 0];
seq.output.P = [0 0];
seq.output.dir = [0 0];
seq.output.A = [0 0];
seq.output.B = [0 0];
seq.target.P = [0 0];
seq.target.dir = [0 0];

base = 2*height*tan(ang/2); % base width of prism
rinner = base/(2*tan(mdang/2)); % radius around which the prisms are aligned
% given by base width and minimum deviation angle
router = rinner + height; % accordingly the radius to prism apex

C = [0 -turn*router]; % position of the first apex, later shifted to zero

for k = number_of_prisms:-1:1,
    g = turn*(pi/2 - turn*(k-1)*mdang); % minimum deviation plane angle between prisms
    X = C+rinner*[cos(g) sin(g)]; % center base vector
    A = C+router*[cos(g) sin(g)]; % apex vector
    S = base*[sin(-g) cos(-g)]/2; % egde vector

    % calculate index for ordering surfaces
    if turn > 0,
        idx = 2*(number_of_prisms-k);
    else
        idx = 2*k;
    end

    % create prism surface: input
    in = surface_create([sin(ang/2+g) -cos(ang/2+g)],...
        A, X-S,...
        refr_outer, refr_inner);
    if turn < 0,
        seq.surface(idx) = in;
    else
        seq.surface(idx+1) = in;
    end

    % create prism surface: output
    out = surface_create([sin(ang/2-g) cos(ang/2-g)],...
        A, X+S,...
        refr_outer, refr_inner);
    if turn < 0,
        seq.surface(idx-1) = out;
    else
        seq.surface(idx+2) = out;
    end
end

```

```

end

function ang = mindev(apex_angle_rad, n_outer, n_inner)
% Calculate minimum deviation of a single prism
ang = 2*asin(n_inner/n_outer*sin(apex_angle_rad/2.0))-apex_angle_rad;

```

Geometric layout: The validity of previous calculations is verified graphically. The function `seq_optimize` takes two prism sequences and shifts the second ring so that a inter-prism distance for a specified wavelength is reached. The geometry of a double-prism sequence (fused silica prisms with an apex angle of 69.2° and base width of 10mm) with a inter-prism distance for 900nm is shown in Fig. C.3.

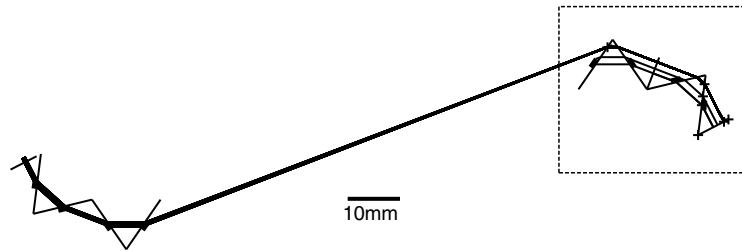


Figure C.1.: The geometrical result of the dispersion compensation calculation for the laser described in Sec. 4. The detailed view and description of the dashed box can be seen in Fig. C.2. The resulting group delay and third order dispersion is depicted in Fig. 3.3.

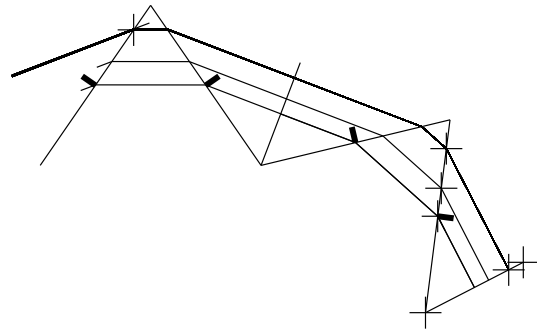


Figure C.2: Detail of the beam width clipping detection.

```

function [seq_first, seq_second] = seq_optimize(seq_1, seq_2, ...
    adj_middev_wave_length, wave_length_range,...
    inter_prism_distance, beam_diameter, center_on_second)
%[seq_first, seq_second] = seq_optimize(seq_1, seq_2, ...
%   adj_middev_wave_length, half_width,...
%   inter_prism_distance, beam_diameter)
%
% Adjust the inter-prism distance of two prism sequences, optionally the beam
% can have a diameter (clipping is avoided) and can be centered on the second ring.
if nargin == 6,
    center_on_second = 0;
end

% show the prism sequence
h = 0;
h = draw_create;
for k=1:seq_1.design.number*2,
    draw_surface(h,seq_1.surface(k));
end

nsurf = seq_1.design.number;

% adjust the input beam
A = (seq_1.surface(nsurf).A + seq_1.surface(nsurf+1).A)/2;
B = (seq_1.surface(nsurf).B + seq_1.surface(nsurf+1).B)/2;

draw_line(h, A, B)

if nsurf/2 == round(nsurf/2),
    dir = seq_1.surface(nsurf).A - seq_1.surface(nsurf+1).A;
else
    dir = seq_1.surface(nsurf).B - seq_1.surface(nsurf+1).B;
end
M = (A+B)/2;
test_beam = beam_create(M, dir, adj_middev_wave_length);

% travell to input surface
[bs_ecode] = beam_travell_seq(test_beam, seq_1, nsurf, -1);
if ecode,
    error('sths wrong here');
end
draw_beams(h, bs);

% calculate input plane (inA, inB, dirin)
Pin = bs(size(bs,2)).P;
dirin = -bs(size(bs,2)).dir;

t = vecdot(seq_1.surface(1).B-Pin, bs(size(bs,2)).dir);

X=Pin+t*bs(size(bs,2)).dir;
inA = seq_1.surface(1).B;
inB = 2*X-inA;
draw_beam(h, bs(size(bs,2)), X);
draw_line(h, inA, inB);

% calculate apex top distance
test_beam = beam_create(X, dirin, wave_length_range(2));
[bs_ecode] = beam_travell_seq(test_beam, seq_1);
draw_beams(h, bs);
test_beam = beam_create(X+0.5*beam_diameter*(X-inA)/norm(X-inA), dirin, wave_length_range(2));
[bs2_ecode] = beam_travell_seq(test_beam, seq_1);
draw_beams(h, bs2);
test_beam = beam_create(seq_1.surface(2*nsurf).A+bs(size(bs,2)).P-bs2(size(bs2,2)).P,...
    -bs(size(bs,2)).dir, wave_length_range(2));
draw_beam(h, test_beam);
[bs3_ecode] = beam_travell_seq(test_beam, seq_1, 2*nsurf, -1);
draw_beams(h, bs3);

draw_cross(h, bs3(size(bs3,2)).P);
draw_cross(h, bs2(2).P);
draw_cross(h, bs(2).P);
fac = norm(bs3(size(bs3,2)).P-bs(2).P)/norm(bs2(2).P-bs(2).P);
Pin = X + fac*0.5*beam_diameter*(X-inA)/norm(X-inA);
draw_cross(h, Pin);

```

```

seq_1.input.P = Pin;
seq_1.input.dir = dirin;

% the output point on last prism on first seq is also target point on
% first prism in second seq (minimum wave length = stronest deviation)
test_beam = beam_create(Pin, dirin, wave_length_range(1));
[bs ecode] = beam_travell_seq(test_beam, seq_1);
seq_1.target.P = bs(size(bs,2)).P;
seq_1.target.dir = bs(size(bs,2)).dir;
seq_2.target.P = -bs(size(bs,2)).P;

draw_beams(h, bs);
draw_cross(h, seq_1.target.P);

% center beam of central wavelength on second prism ring
if center_on_second,
    test_beam = beam_create(Pin, dirin, adj_middev_wave_length);
    [bs ecode] = beam_travell_seq(test_beam, seq_1);
    seq_1.target.P = bs(size(bs,2)).P;
    seq_1.target.dir = bs(size(bs,2)).dir;
    seq_2.target.P = 0.5*(seq_2.surface(1).B - seq_2.surface(1).A);
end

%% output plane
seq_2.output.A = seq_2.surface(nsurf*2).B+0.5*beam_diameter*(inA-inB)/norm(inA-inB);
seq_2.output.B = seq_2.output.A + (inA - inB)-0.5*beam_diameter*(inA-inB)/norm(inA-inB);

draw_cross(h, inA);
draw_cross(h, inB);

[seq_1, seq_2] = seq_distance(seq_1, seq_2, inter_prism_distance);
for k=1:seq_1.design.number*2,
    draw_surface(h,seq_2.surface(k));
end
draw_line(h, seq_2.output.A, seq_2.output.B);

seq_first = seq_1;
seq_second = seq_2;

%% show design points
if h,
    d = 1e-9;
    mirror = surface_create([-1 -1], seq_2.output.A, seq_2.output.B, [], []);
    for k = wave_length_range(1):d:wave_length_range(2),
        test_beam = beam_create(Pin, dirin, k);
        [b_seq_1 ecode] = beam_travell_seq(test_beam, seq_1);
        if ecode,
            continue;
        end
        [b_seq_2 ecode] = beam_travell_seq(b_seq_1(size(b_seq_1,2)), seq_2);
        if ecode,
            continue;
        end
        nbs2 = size(b_seq_2,2);
        [M ecode] = isect_surface_beam(mirror, b_seq_2(nbs2));
        if ecode == 1,
            continue;
        end
        b_seq_2(nbs2+1) = beam_create(M, b_seq_2(nbs2).dir, ...
            b_seq_2(nbs2).lambda, b_seq_2(nbs2).index);

        draw_beams(h, b_seq_1);
        draw_beams(h, b_seq_2);
    end
end

```

To calculate the inter-prism distance for a given group velocity dispersion, `seq_optimize` is called with a simple contracting inter-prism distance interval around the desired dispersion.

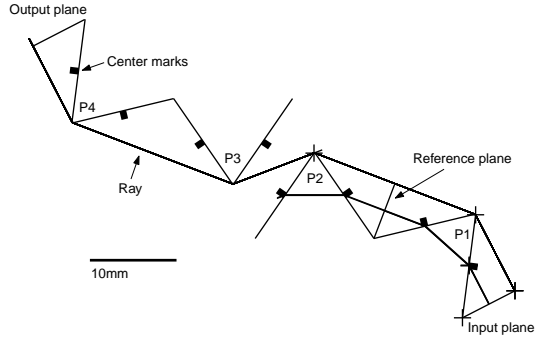


Figure C.3: Result of the algorithm, setting a vanishing beam diameter, a inter prism ring apex distance equal the base height of a prism for a central wavelength of 900nm.

Dispersion calculation: With the previous functions, the optical path length can be calculated per wavelength by summing up all inter-surface beams ($\overline{P_i P_{i+1}}$, see definition of structure of a beam `beam_create`). To calculate the n -th order dispersion ($d^n \text{OPL}/d\omega^n$) the optical path length is transformed into the frequency domain.

```
function [dout, lout] = delay_series(OPL, lambda, order)
%[beta lambda]= delay_series(OPL, lambda, order)
%
% Calculate the differentials up to a certain order.
% OPL and lambda must be matrices > 2*order+1.

nP = size(OPL,2);
const_C = 2.99792458e8; % speed of light

% allocate result matrix
dout(1+order, nP-2*order) = 0.0;

% reorder to differentiate over circular frequency
for k=1:nP,
    P = OPL(k);
    w = 2*pi*const_C/lambda(k);

    b = w*P/const_C;

    ob(nP+1-k) = b;
    ow(nP+1-k) = w;
end

% reorder again output for [1] path length [2] phase
dN = derive(ow, ob);
for k=1:nP-2*order,
    l = nP+1-(k+order);
    dout(1,k) = ob(l);
    dout(2,k) = dN(l);
end

% differentiate order by order (GVD, TOD, ...)
for o=2:order,
    dN = derive(ow, dN);

    for k=1:nP-2*order,
        l = nP+1-(k+order);
        dout(o+1,k) = dN(l);
    end
end

for k=1:nP-2*order,
    l = nP+1-(k+order);
```

```

        lout(k) = lambda(k+order);
    end
    return

function d = derive(x,y)
% derivative
nx = size(x,2);
d(nx) = 0;

for k=2:nx-1,
    d(k) = (y(k+1)-y(k-1))/(x(k+1)-x(k-1));
end

```

C.2. Cavity construction

The calculations for laser cavity were carried out with MATHEMATICA (Wolfram Research). The following Mathematica notebook is partially shortened for readability. The Sellmeier coefficients and formula were kindly provided in a notebook from Winfried Denk.

Optic formulas

(Introduction)

Basic formulas

Constants

```

In[1]:= kilo = 103;
In[2]:= milli = 10-3;
In[3]:= micro = 10-6;
In[4]:= nano = 10-9;
In[5]:= femto = 10-15;
In[6]:= Clight = 2.99792 108
In[7]:= deg =  $\frac{\pi}{180}$ ;

```

Conversions

```

In[8]:= Rad2Deg[α_] = α  $\frac{180}{\pi}$ ;
In[9]:= Deg2Rad[α_] = α  $\frac{\pi}{180}$ ;

```

Sellmeier coefficients from Schott catalog

$In[10] := \text{scSiO2} = \{0.696166, 4.07943 \cdot 10^{-1}, 0.897479, 0.0684043^2,$
 $0.116241^2, 9.89616^2\};$
 $In[11] := \text{scAl2O3o} = \{1.43135, 0.650547, 5.3414, 0.0726631^2,$
 $0.119324^2, 18.0283^2\};$

Optics relations

Refraction

Angle of refraction at an interface:

$In[12] := \text{Refracted}[i_ , ni_ , nr_] = \text{ArcSin}\left[\frac{ni}{nr} \text{Sin}[i]\right];$

Brewster angle

Brewster angles (incident and refracted):

$In[13] := \text{BrewsterI}[ni_ , nr_] = \text{ArcSin}[nr / \text{Sqrt}[nr^2 + ni^2]];$

$In[14] := \text{BrewsterR}[ni_ , nr_] = \text{ArcSin}[ni / \text{Sqrt}[nr^2 + ni^2]];$

Seilmeier formula

$In[15] := \text{nSellmeier}[\text{lambda_}, \text{coeff_}] := \text{Sqrt}[$
 $1 + \text{coeff}[[1]](\lambda/\text{micro})^2/((\lambda/\text{micro})^2 - \text{coeff}[[4]]) +$
 $\text{coeff}[[2]](\lambda/\text{micro})^2/((\lambda/\text{micro})^2 - \text{coeff}[[5]]) +$
 $\text{coeff}[[3]](\lambda/\text{micro})^2/((\lambda/\text{micro})^2 - \text{coeff}[[6]])];$

Gaussian approximation

Classical Gaussian approximation

Connection between complex curvature q and the beam waist w resp. radius of curvature R

$In[16] := \text{GRadius}[q_ , \lambda_] = \left(\text{Re}\left[\frac{1}{q}\right]\right)^{-1};$

$In[17] := \text{GWaist}[q_ , \lambda_] = \text{Sqrt}\left[\frac{\lambda}{\pi} \left(\text{Im}\left[\frac{1}{q}\right]\right)^{-1}\right];$

$In[18] := \text{CCq}[w_ , R_ , \lambda_] = \left(\frac{1}{R} + \frac{\lambda}{\pi} \frac{1}{w^2}\right)^{-1};$

Determination of a Beam with given width and curvature...

$In[19] := \text{GBeamWaistDistance}[q_ , \lambda_] := -\frac{\text{GRadius}[q, \lambda]}{1 + \left(\frac{\lambda \text{GRadius}[q, \lambda]}{\pi (\text{GWaist}[q, \lambda])^2}\right)^2}$

$$In[20] := \text{GBeamWaist}[q, \lambda] := \frac{\text{GWaist}[q, \lambda]}{\sqrt{1 + \left(\frac{\pi(\text{GWaist}[q, \lambda])^2}{\lambda \text{GRadius}[q, \lambda]} \right)^2}}$$

Gaussian approximation in ABCD matrix representation

Transformation of the complex curvature $q \rightarrow M \cdot q$

$$In[21] := \text{GTransCCq}[q, M] := \frac{M[[1, 1]] q + M[[1, 2]]}{M[[2, 1]] q + M[[2, 2]]},$$

Matrix descriptions

In the following GMx and GMy refer to the tangential resp. sagittal plane

Free propagation

$$In[22] := \text{GMFree}[l, n] = \begin{pmatrix} 1 & \frac{1}{n} \\ 0 & 1 \end{pmatrix};$$

Lens defined by focal length or radius of curvature

$$In[23] := \text{GMLens}[f] = \begin{pmatrix} 1 & 0 \\ -\frac{1}{f} & 1 \end{pmatrix};$$

Lens, tilted in the tangential (x-z) plane

$$In[24] := \text{GMxLens}[f, \alpha] = \begin{pmatrix} 1 & 0 \\ -\frac{1}{f \cos[\alpha]} & 1 \end{pmatrix};$$

$$In[25] := \text{GMyLens}[f, \alpha] = \begin{pmatrix} 1 & 0 \\ -\frac{\cos[\alpha]}{f} & 1 \end{pmatrix};$$

Refractive interface (incident, refracted), tilted in the tangential plane

$$In[26] := \text{GMxInterface}[i, r] = \begin{pmatrix} \frac{\cos[r]}{\cos[i]} & 0 \\ 0 & \frac{\cos[i]}{\cos[r]} \end{pmatrix};$$

$$\text{GMyInterface}[i, r] = \begin{pmatrix} 1 & 0 \\ 0 & 1 \end{pmatrix};$$

Refractive interface at Brewster angle, tilted in the tangential plane

```
In[27] := GMxBrewster[ni_, nr_] =
  GMxInterface[BrewsterI[ni, nr], BrewsterR[ni, nr]];
```

```
GMyBrewster[ni_, nr_] =
  GMyInterface[BrewsterI[ni, nr], BrewsterR[ni, nr]];
```

Roundtrip matrix

```
In[28] := GMRoundTrip[M_] := M.  $\begin{pmatrix} M[[2, 2]] & M[[1, 2]] \\ M[[2, 1]] & M[[1, 1]] \end{pmatrix}$ 
```

```
In[29] :=
```

Laser design

Cavity design

Parameters

The CAVITY parameters are stored in a list the following way (from output, lines in *italic* denote values, that are not known at design start):

- 1 L_1 length of first arm
- 2 f/M_2 focal length of first focusing mirror
- 3 α/M_2 *folding angle of M_2*
- 4 $d/M_2 \rightarrow$ *Cr distance from M_2 to crystal*
- 5 α/Cr *tilt angle (brewster angle in respect to wave length of pump laser)*
- 6 t/Cr Crystal rod length (geometric)
- 7 n/Cr Sellmeier coefficients of the crystal
- 8 $d/Cr \rightarrow$ *M_3 distance from crystal to M_3*
- 9 L_2 length of second arm
- 10 f/M_3 focal length of the second focusing mirror
- 11 α/M_3 *folding angle of M_3*
- 12 $\lambda/$ Cavity central operation wave length
- 13 l/Cr The assumed position of the focal spot inside the crystal

measured from the pump beam input side (here M_3)

14 P/Cavity Assumed intracavity CW power

15 hRth/Crystal Assumed radius of curvature of thermal lense at the crystal surface directed towards M_3 (tangential)

16 vRth/Crystal Assumed radius of curvature of thermal lense at the crystal surface directed towards M_3 (horizontal)

The PUMP parameters:

1 f/M_p focal length of pump beam focusing mirror

2 α/M_p tilt angle

3 $d/M_p \rightarrow M_3$ distance to mirror M_3

4 l/M_3 width of input coupler M_3

5 n/M_3 Sellmeier coefficients of M_3

6 λ /Pump Pump wave length

7 d/Pump Pump beam diameter

To account for astigmatism, the calculations are split in tangential and sagittal plan, thus the matrices/calculations are prefixed with a **t** or **s** respectively.

Additionally, there may be the suffix "reverse".

Helper methods

The following methods modify some single entries in the cavity or pump property list. All methods return the {cavity, pump} list.

```
In[30] := cavitySetNothing[cavity_, pump_] :=  
  {{cavity[[1]], cavity[[2]], cavity[[3]], cavity[[4]],  
    cavity[[5]], cavity[[6]], cavity[[7]], cavity[[8]],  
    cavity[[9]], cavity[[10]], cavity[[11]], cavity[[12]],  
    cavity[[13]], cavity[[14]], cavity[[15]], cavity[[16]]},  
  pump}
```

```

In[31] := cavitySetCrystalTilt[cavity_, pump_, α_] :=
  {{cavity[[1]], cavity[[2]], cavity[[3]], cavity[[4]],
    α, cavity[[6]], cavity[[7]], cavity[[8]],
    cavity[[9]], cavity[[10]], cavity[[11]], cavity[[12]],
    cavity[[13]], cavity[[14]], cavity[[15]], cavity[[16]]},
  pump}
In[32] := cavitySetM2Tilt[cavity_, pump_, α_] :=
  {{cavity[[1]], cavity[[2]], α, cavity[[4]],
    cavity[[5]], cavity[[6]], cavity[[7]], cavity[[8]],
    cavity[[9]], cavity[[10]], cavity[[11]], cavity[[12]],
    cavity[[13]], cavity[[14]], cavity[[15]], cavity[[16]]},
  pump}
In[33] := cavitySetM3Tilt[cavity_, pump_, α_] :=
  {{cavity[[1]], cavity[[2]], cavity[[3]], cavity[[4]],
    cavity[[5]], cavity[[6]], cavity[[7]], cavity[[8]],
    cavity[[9]], cavity[[10]], α, cavity[[12]],
    cavity[[13]], cavity[[14]], cavity[[15]], cavity[[16]]},
  pump}

```

The wave length of the pump beam is used to calculate the orientation of the crystal

```

In[34] := orientCrystal[cavity_, pump_] := cavitySetCrystalTilt[cavity, pump,
  Rad2Deg[BrewsterI[1, nSellmeier[pump[[6]], cavity[[7]]]]]]

```

Misc properties

The critical power

```

In[35] := criticalPowerTiAl2O3[cavity_] :=
  
$$\frac{\alpha (\text{cavity}[[12]])^2}{8\pi \text{nSellmeier}[\text{cavity}[[12]], \text{cavity}[[7]]] \text{n2}}$$

  /. {α = 5.35, n2 = 3 10-2}

```

The repetition rate of the cavity

```

In[36] := repetitionRate[cavity_] :=
  Clight/(2(cavity[[1]] + cavity[[4]] + cavity[[6]])/
    Cos[Refracted[Deg2Rad[cavity[[5]]], 1, nSellmeier[
      cavity[[12]], cavity[[7]]]] + cavity[[8]] + cavity[[9]])

```

Calculation of partial ABCD matrices

The first matrix goes from M_1 to inside the crystal (directly behind the surface, crystal orientation is always at Brewster angle), see (Magni et al. [1993a])

```
In[37] := tM1ToCrystal[cavity_, pump_] :=  
  GMxInterface[Deg2Rad[cavity[[5]]], Refracted[Deg2Rad[cavity[[5]]],  
    1, nSellmeier[cavity[[12]], cavity[[7]]]].  
  GMFree[cavity[[4]], 1].  
  GMxLens[cavity[[2]], Deg2Rad[cavity[[3]]]].  
  GMFree[cavity[[1]], 1]  
  
sM1ToCrystal[cavity_, pump_] :=  
  GMyInterface[Deg2Rad[cavity[[5]]], Refracted[  
    Deg2Rad[cavity[[5]]], 1, nSellmeier[cavity[[12]], cavity[[7]]]].  
  GMFree[cavity[[4]], 1].  
  GMyLens[cavity[[2]], Deg2Rad[cavity[[3]]].  
  GMFree[cavity[[1]], 1]
```

and the same in reverse direction

```
In[38] := tM1ToCrystalReverse[cavity_, pump_] :=  
  GMFree[cavity[[1]], 1].  
  GMxLens[cavity[[2]], Deg2Rad[cavity[[3]]]].  
  GMFree[cavity[[4]], 1].  
  GMxInterface[Refracted[Deg2Rad[cavity[[5]]], 1,  
    nSellmeier[cavity[[12]], cavity[[7]]], Deg2Rad[cavity[[5]]]]  
  
sM1ToCrystalReverse[cavity_, pump_] :=  
  GMFree[cavity[[1]], 1].  
  GMyLens[cavity[[2]], Deg2Rad[cavity[[3]]]].  
  GMFree[cavity[[4]], 1].  
  GMyInterface[Refracted[Deg2Rad[cavity[[5]]], 1,  
    nSellmeier[cavity[[12]], cavity[[7]]], Deg2Rad[cavity[[5]]]]
```

The geometric path length inside the crystal for a given λ at Brewster angle orientation

```
In[39] := GPLofCrystal[cavity_] :=  
  cavity[[6]]/ Cos[Refracted[Deg2Rad[cavity[[5]]],  
    1, nSellmeier[cavity[[12]], cavity[[7]]]]
```


The crystal

```
In[40] := tCrystalHalf[cavity_, pump_] :=
  GMFree[GPLofCrystal[cavity]/2,
    nSellmeier[cavity[[12]], cavity[[7]]];
```

```
sCrystalHalf[cavity_, pump_] :=
  GMFree[GPLofCrystal[cavity]/2,
    nSellmeier[cavity[[12]], cavity[[7]]];
```

and its matrix, representing the Kerr lens

```
In[41] := CrystalMk[cavity_, pump_, γ_] :=  $\frac{1}{\sqrt{1-\gamma}}$ 
  (  $-\frac{1-\gamma/2}{n_{\text{Sellmeier}}[cavity[[12]], cavity[[7]]]}$ 
     $-\frac{\gamma \text{cavity}[[6]]/\text{Cos}[\text{Refracted}[\text{Deg2Rad}[cavity[[5]]], 1, n_{\text{Sellmeier}}[cavity[[12]], cavity[[7]]]]}{4n_{\text{Sellmeier}}[cavity[[12]], cavity[[7]]]}$ 
     $-\frac{\gamma \text{cavity}[[6]]/\text{Cos}[\text{Refracted}[\text{Deg2Rad}[cavity[[5]]], 1, n_{\text{Sellmeier}}[cavity[[12]], cavity[[7]]]]}{1-\gamma/2}$ 
  );
```

Now the matrices from the crystal to the end mirror:

```
In[42] := tCrystalToM4[cavity_, pump_] :=
  GMFree[cavity[[9]], 1].
  GMxLens[cavity[[10]], Deg2Rad[cavity[[11]]]].
  GMFree[cavity[[8]], 1].
  GMLens[cavity[[15]]].
  GMxInterface[Refracted[Deg2Rad[cavity[[5]]], 1,
    nSellmeier[cavity[[12]], cavity[[7]]], Deg2Rad[cavity[[5]]]]

sCrystalToM4[cavity_, pump_] :=
  GMFree[cavity[[9]], 1].
  GMyLens[cavity[[10]], Deg2Rad[cavity[[11]]]].
  GMFree[cavity[[8]], 1].
  GMLens[cavity[[16]]].
  GMyInterface[Refracted[Deg2Rad[cavity[[5]]], 1,
    nSellmeier[cavity[[12]], cavity[[7]]], Deg2Rad[cavity[[5]]]]
```

and reverse

```

In[43] := tCrystalToM4Reverse[cavity_, pump_] :=
  GMxInterface[Deg2Rad[cavity[[5]]], Refracted[
    Deg2Rad[cavity[[5]]], 1, nSellmeier[cavity[[12]], cavity[[7]]]] .
  GMFree[cavity[[4]], 1].
  GMLens[cavity[[15]]].
  GMFree[cavity[[8]], 1].
  GMxLens[cavity[[10]], Deg2Rad[cavity[[11]]]].
  GMFree[cavity[[9]], 1]

sCrystalToM4Reverse[cavity_, pump_] :=
  GMyInterface[Deg2Rad[cavity[[5]]], Refracted[
    Deg2Rad[cavity[[5]]], 1, nSellmeier[cavity[[12]], cavity[[7]]]] .
  GMFree[cavity[[4]], 1].
  GMLens[cavity[[16]]].
  GMFree[cavity[[8]], 1].
  GMyLens[cavity[[10]], Deg2Rad[cavity[[11]]]].
  GMFree[cavity[[9]], 1]

```

Stability limits

The tangential and sagittal single trip matrices starting at the output coupler are

```

In[44] := tSTOutputCoupler[cavity_, pump_,  $\gamma$ _] :=
  tCrystalToM4[cavity, pump].
  tCrystalHalf[cavity, pump].
  CrystalMk[cavity, pump,  $\gamma$ ].
  tCrystalHalf[cavity, pump].
  tM1ToCrystal[cavity, pump];

sSTOutputCoupler[cavity_, pump_,  $\gamma$ _] :=
  sCrystalToM4[cavity, pump].
  sCrystalHalf[cavity, pump].
  CrystalMk[cavity, pump,  $\gamma$ ].
  sCrystalHalf[cavity, pump].
  sM1ToCrystal[cavity, pump];

```

The respective stability limits may be solved as follows:

The solution of $q = M_{RT}q$, with q Gaussian beam, M_{RT} round-trip matrix can be simplified to solve

$\{A=0, B=0, C=0, D=0\}$, where A, B, C, D are the matrix elements of the single-trip matrix.

Application to the setup

Cavity parameters

$In[45] := \text{mypump} = \{\text{fp}, \delta, \text{xp}, 10 \text{ milli}, \text{scSiO2}, 532 \text{ nano}, 2.25 \text{ milli}\}$

$\text{mycavity} = \{200 \text{ milli}, 50 \text{ milli}, \alpha,$
 $\text{d},$
 $0, \text{t}, \text{scAl2O3o},$
 $\text{x},$
 $290 \text{ milli}, 50 \text{ milli}, \beta,$
 $\lambda, 1 \text{ milli},$
 $1/0.12,$
 $\text{fthh}, \text{fthv}\} /. \{\text{t} \rightarrow 5 \text{ milli}, \lambda \rightarrow 850 \text{ nano}\}$

Stability limits of the unfolded, astigmatism free cavity:

The stability limits in z (folding mirror distance) are

(it should be noted, that the solution is actually independent of the position of the crystal)

`In[46] := {tmpcavity, tmppump} = cavitySetCrystalTilt[mycavity, mypump, 0];`

`(z/.Solve[Sim`

```
{(z/.Solve[Simplify[tSTOutputCoupler[tmpcavity, tmppump, 0][[2, 1]]
/. {d → z - x - tmpcavity[[6]]/ Cos[Deg2Rad[tmpcavity[[5]]]],
fthh → ∞, fthv → ∞, α → 0, β → 0}
/. {x → 0milli} == 0, z]),
(z/.Solve[Simplify[tSTOutputCoupler[tmpcavity, tmppump, 0][[1, 1]]
/. {d → z - x - tmpcavity[[6]]/ Cos[Deg2Rad[tmpcavity[[5]]]],
fthh → ∞, fthv → ∞, α → 0, β → 0}
/. {x → 0milli} == 0, z]),
(z/.Solve[Simplify[tSTOutputCoupler[mycavity, mypump, 0][[2, 2]]
/. {d → z - x - tmpcavity[[6]]/ Cos[Deg2Rad[tmpcavity[[5]]]],
fthh → ∞, fthv → ∞, α → 0, β → 0}
/. {x → 0milli} == 0, z]),
Out[46]= {{0.102157}, {0.112574}, {0.118824}, {0.129241}}
```

Astigmatism correction

Adjust the crystal, so that the pump beam is at Brewster angle:

`In[47] := {mycavity, mypump} = orientCrystal[mycavity, mypump]`

```
Out[47]= {{1/5, 1/20, α, d, 60.5583, 1/200,
{1.43135, 0.650547, 5.3414, 0.00527993, 0.0142383, 325.018},
x, 29/100, 1/20, β, 17/20000000, 1/1000, 8.33333, fthh, fthv},
{fp, δ, xp, 1/100, {0.696166, 0.407943, 0.897479,
0.00467915, 0.0135121, 97.934}, 133/250000000, 0.00225}}
```

1. Stability limit

First, we will calculate the folding angles for the first stability limit. The resulting angle will then be used, to solve the third stability limit.

```

In[48]:= stla1[a_, b_, fth_,  $\gamma$ _] :=
  (z/.Solve[Simplify[tSTOutputCoupler[mycavity, mypump,  $\gamma$ ][[2, 1]]
    /. {d  $\rightarrow$  z - x - mycavity[[6]]/ Cos[Deg2Rad[mycavity[[5]]]],
      fthh  $\rightarrow$  fth,  $\alpha \rightarrow$  a,  $\beta \rightarrow$  b}
    /. {x  $\rightarrow$  0milli}] == 0, z)][[1]]

stlb1[a_, b_, fth_,  $\gamma$ _] :=
  (z/.Solve[Simplify[sSTOutputCoupler[mycavity, mypump,  $\gamma$ ][[2, 1]]
    /. {d  $\rightarrow$  z - x - mycavity[[6]]/ Cos[Deg2Rad[mycavity[[5]]]],
      fthv  $\rightarrow$  fth,  $\alpha \rightarrow$  a,  $\beta \rightarrow$  b}
    /. {x  $\rightarrow$  0milli}] == 0, z)][[1]]

 $\phi_1 = \alpha$ /.Solve[Simplify[stla1[ $\alpha$ ,  $\alpha$ ,  $\infty$ , 0] == stlb1[ $\alpha$ ,  $\alpha$ ,  $\infty$ , 0],  $\alpha$ ][[3]]
Out[48]= 8.52995

```

The folding mirror distance z is then

```

In[49]:= {tmpcavity, tmppump} = cavitySetM2Tilt[mycavity, mypump,  $\phi_1$ ];

{tmpcavity, tmppump} = cavitySetM3Tilt[tmpcavity, tmppump,  $\phi_1$ ];

z1 =
  (z/.Solve[Simplify[tSTOutputCoupler[tmpcavity, tmppump, 0][[2, 1]]
    /. {d  $\rightarrow$  z - x - tmpcavity[[6]]/ Cos[Deg2Rad[tmpcavity[[5]]]],
      fthh  $\rightarrow$   $\infty$ , fthv  $\rightarrow$   $\infty$ ,  $\alpha \rightarrow$  0,  $\beta \rightarrow$  0}
    /. {x  $\rightarrow$  0milli}] == 0, z)][[1]]

Out[49]= 0.108019

```

3. Stability limit

From the previous calculation of the 1. stability limit, we know, what the folding angle of the mirror near the dispersion compensation (parallel beam propagation) has to be:

```

In[50]:= stla3[a_, b_, fth_,  $\gamma$ _] :=
  (z/.Solve[Simplify[tSTOutputCoupler[mycavity, mypump,  $\gamma$ ][[2, 2]]
    /. {d  $\rightarrow$  z - x - mycavity[[6]]/ Cos[Deg2Rad[mycavity[[5]]]],
      fthh  $\rightarrow$  fth,  $\alpha \rightarrow$  a,  $\beta \rightarrow$  b}
    /. {x  $\rightarrow$  0milli}] == 0, z)][[1]]

stlb3[a_, b_, fth_,  $\gamma$ _] :=
  (z/.Solve[Simplify[sSTOutputCoupler[mycavity, mypump,  $\gamma$ ][[2, 2]]
    /. {d  $\rightarrow$  z - x - mycavity[[6]]/ Cos[Deg2Rad[mycavity[[5]]]],
      fthv  $\rightarrow$  fth,  $\alpha \rightarrow$  a,  $\beta \rightarrow$  b}
    /. {x  $\rightarrow$  0milli}] == 0, z)][[1]]

 $\phi_3 = \alpha$ /.Solve[stla3[ $\alpha$ ,  $\phi_1$ ,  $\infty$ , 0] == stlb3[ $\alpha$ ,  $\phi_1$ ,  $\infty$ , 0],  $\alpha$ ][[3]]
Out[50]= 6.40264

```

The folding mirror distance z is then

```

In[51]:= {tmpcavity, tmppump} = cavitySetM2Tilt[mycavity, mypump,  $\phi_3$ ];

{tmpcavity, tmppump} = cavitySetM3Tilt[tmpcavity, tmppump,  $\phi_1$ ];

z3 =
  (z/.Solve[Simplify[tSTOutputCoupler[tmpcavity, tmppump, 0][[2, 2]]
    /. {d  $\rightarrow$  z - x - tmpcavity[[6]]/ Cos[Deg2Rad[tmpcavity[[5]]]],
      fthh  $\rightarrow$   $\infty$ , fthv  $\rightarrow$   $\infty$ ,  $\alpha \rightarrow$  0,  $\beta \rightarrow$  0}
    /. {x  $\rightarrow$  0milli}] == 0, z)][[1]]

Out[51]= 0.124685

In[52]:= {tmpcavity, tmppump} = cavitySetM2Tilt[mycavity, mypump, 6];

{tmpcavity, tmppump} = cavitySetM3Tilt[tmpcavity, tmppump, 6.5];

(z/.Solve[Simplify[tSTOutputCoupler[tmpcavity, tmppump, 0][[2, 2]]
  /. {d  $\rightarrow$  z - x - tmpcavity[[6]]/ Cos[Deg2Rad[tmpcavity[[5]]]],
    fthh  $\rightarrow$   $\infty$ , fthv  $\rightarrow$   $\infty$ ,  $\alpha \rightarrow$  0,  $\beta \rightarrow$  0}
  /. {x  $\rightarrow$  0milli}] == 0, z)][[1]]

Out[52]= 0.124984

```

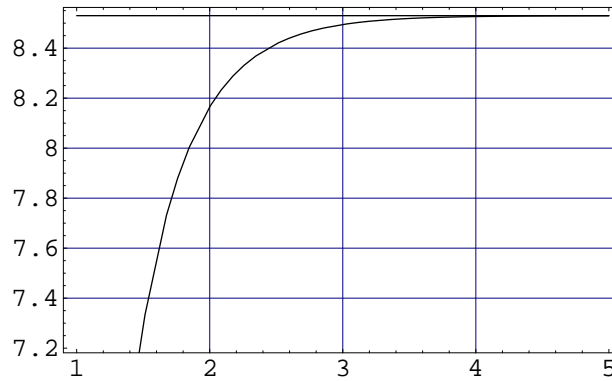
Thermal considerations

We express the folding angle of the 1. stability limit in the relation to the

focal length of mirror M_3 (R) and the assymetry between horizontal versus vertical focal length of the thermal lens (a):

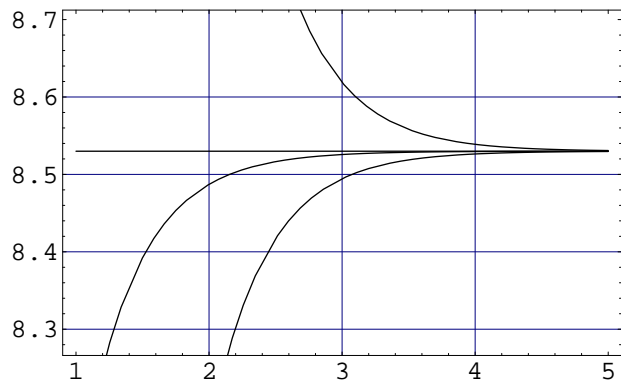
```
In[53]:= thermalFoldingAngle1[R_, a_] :=  
       $\alpha$ /.Solve[Simplify[stla1[ $\alpha$ ,  $\alpha$ , -a * R * mycavity[[10]], 0] ==  
      stlb1[ $\alpha$ ,  $\alpha$ , -R * mycavity[[10]], 0]],  $\alpha$ ][[6]]
```

```
In[54]:= Plot[  
  {  
    thermalFoldingAngle1[10x, 1.5],  
     $\phi_1$   
  }, {x, 1, 5}, AxesLabel → {10R/f, Foldingangle[deg]},  
  Frame → True, GridLines → Automatic]
```



Out[54]= -Graphics-

```
In[55]:= Plot[  
  {  
    thermalFoldingAngle1[10x, 0.5],  
    thermalFoldingAngle1[10x, 1],  
    thermalFoldingAngle1[10x, 1.5],  
     $\phi_1$   
  }, {x, 1, 5}, AxesLabel → {10R/f, Foldingangle[deg]},  
  Frame → True, GridLines → Automatic]
```

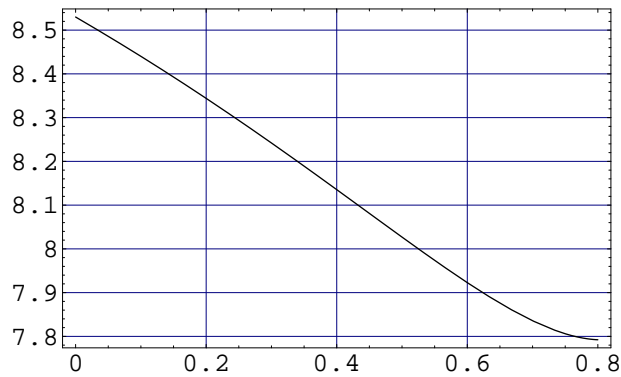


Out[55]= -Graphics-

Kerr lens considerations

```
In[56]:= kerrlensFoldingAngle1[γ_, a_] :=
α/.Solve[Simplify[stla1[α, α, ∞, a * γ] == stlb1[α, α, ∞, γ]], α][[5]]
```

```
In[57]:= Plot[
{
kerrlensFoldingAngle1[x, 1.5]
}, {x, 0, 0.8}, AxesLabel → {γ, Folding angle [deg]},
Frame → True, GridLines → Automatic]
```

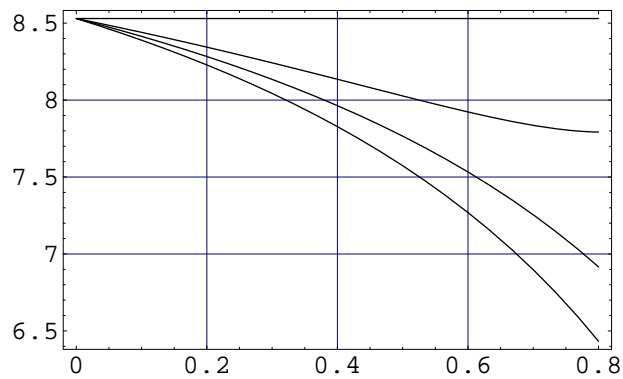


Out[57]= -Graphics-


```

In[58]:= Plot[
  {
    kerrlensFoldingAngle1[x, 0.5],
    kerrlensFoldingAngle1[x, 1],
    kerrlensFoldingAngle1[x, 1.5],
     $\phi_1$ 
  }, {x, 0, 0.8}, AxesLabel → { $\gamma$ , Folding angle [deg]},
  Frame → True, GridLines → Automatic]

```



Out[58]= -Graphics-

Small signal mode variation

```

In[59]:= tMKtoM1[cavity_, pump_] :=
  tM1ToCrystalReverse[cavity, pump].
  tCrystalHalf[cavity, pump]

sMKtoM1[cavity_, pump_] :=
  sM1ToCrystalReverse[cavity, pump].
  sCrystalHalf[cavity, pump]

```

```

In[60] := tMKtoM4[cavity_, pump_] :=
    tCrystalToM4[cavity, pump].
    tCrystalHalf[cavity, pump]

sMKtoM4[cavity_, pump_] :=
    sCrystalToM4[cavity, pump].
    sCrystalHalf[cavity, pump]
In[61] := tM1toM4[cavity_, pump_] :=
    tCrystalToM4[cavity, pump].
    tCrystalHalf[cavity, pump].
    tCrystalHalf[cavity, pump].
    tM1ToCrystal[cavity, pump]

sM1toM4[cavity_, pump_] :=
    sCrystalToM4[cavity, pump].
    sCrystalHalf[cavity, pump].
    sCrystalHalf[cavity, pump].
    sM1ToCrystal[cavity, pump]

```

```

In[62] := tAlpha1[cavity_, pump_] :=
  2 tMKtoM1[cavity, pump][[1, 2]] tMKtoM1[cavity, pump][[2, 2]]/
  (mycavity[[6]]/ Cos[Deg2Rad[mycavity[[5]]]]) -
  tMKtoM1[cavity, pump][[1, 1]] tMKtoM1[cavity, pump][[2, 1]]
  (mycavity[[6]]/ Cos[Deg2Rad[mycavity[[5]]]])/2

tAlpha2[cavity_, pump_] :=
  2 tMKtoM4[cavity, pump][[1, 2]] tMKtoM4[cavity, pump][[2, 2]]/
  (mycavity[[6]]/ Cos[Deg2Rad[mycavity[[5]]]]) -
  tMKtoM4[cavity, pump][[1, 1]] tMKtoM4[cavity, pump][[2, 1]]
  (mycavity[[6]]/ Cos[Deg2Rad[mycavity[[5]]]])/2

tS[cavity_, pump_] := tM1toM4[cavity, pump][[1, 1]]
  tM1toM4[cavity, pump][[2, 2]] +
  tM1toM4[cavity, pump][[1, 2]] tM1toM4[cavity, pump][[2, 1]]

sAlpha1[cavity_, pump_] :=
  2 * sMKtoM1[cavity, pump][[1, 2]] sMKtoM1[cavity, pump][[2, 2]]/
  (mycavity[[6]]/ Cos[Deg2Rad[mycavity[[5]]]]) -
  sMKtoM1[cavity, pump][[1, 1]] sMKtoM1[cavity, pump][[2, 1]]
  (mycavity[[6]]/ Cos[Deg2Rad[mycavity[[5]]]])/2

sAlpha2[cavity_, pump_] :=
  2 * sMKtoM4[cavity, pump][[1, 2]] sMKtoM4[cavity, pump][[2, 2]]/
  (mycavity[[6]]/ Cos[Deg2Rad[mycavity[[5]]]]) -
  sMKtoM4[cavity, pump][[1, 1]] sMKtoM4[cavity, pump][[2, 1]]
  (mycavity[[6]]/ Cos[Deg2Rad[mycavity[[5]]]])/2

sS[cavity_, pump_] := sM1toM4[cavity, pump][[1, 1]]
  sM1toM4[cavity, pump][[2, 2]] +
  sM1toM4[cavity, pump][[1, 2]] sM1toM4[cavity, pump][[2, 1]]

tSmallSignal1[cavity_, pump_] :=
  -1/2 (tAlpha1[cavity, pump] + tAlpha2[cavity, pump] tS[cavity, pump])/
  (tAlpha1[cavity, pump])^2 + (tAlpha2[cavity, pump])^2 +
  2 tAlpha1[cavity, pump] tAlpha2[cavity, pump] tS[cavity, pump]

sSmallSignal1[cavity_, pump_] :=
  -1/2 (sAlpha1[cavity, pump] + sAlpha2[cavity, pump] sS[cavity, pump])/
  ((sAlpha1[cavity, pump])^2 + (sAlpha2[cavity, pump])^2 +
  2 sAlpha1[cavity, pump] sAlpha2[cavity, pump] sS[cavity, pump])

```

```

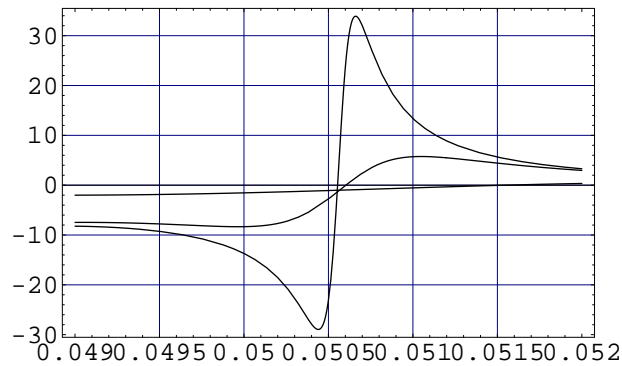
In[63]:= {tmpcavity, tmppump} = cavitySetM2Tilt[mycavity, mypump,  $\phi_3$ ];

{tmpcavity, tmppump} = cavitySetM3Tilt[tmpcavity, tmppump,  $\phi_1$ ]/.
  {d  $\rightarrow$  z - x - tmpcavity[[6]]/ Cos[Deg2Rad[tmpcavity[[5]]]],
   fthh  $\rightarrow$  -1.12, fthv  $\rightarrow$  -2.};

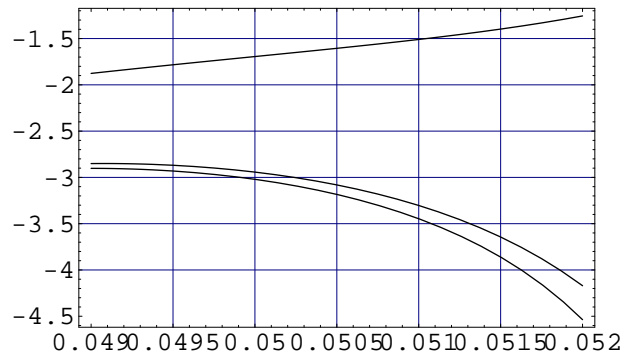
Plot[
  {
    tSmallSignal1[tmpcavity, tmppump] /. z  $\rightarrow$  z3 + 0.001milli,
    tSmallSignal1[tmpcavity, tmppump] /. z  $\rightarrow$  z3 + 0.01milli,
    tSmallSignal1[tmpcavity, tmppump] /. z  $\rightarrow$  z3 + 0.3milli
  }, {x, 49milli, 52milli}, Frame  $\rightarrow$  True, GridLines  $\rightarrow$  Automatic]

Plot[
  {
    sSmallSignal1[tmpcavity, tmppump] /. z  $\rightarrow$  z3 + 0.001milli,
    sSmallSignal1[tmpcavity, tmppump] /. z  $\rightarrow$  z3 + 0.01milli,
    sSmallSignal1[tmpcavity, tmppump] /. z  $\rightarrow$  z3 + 0.3milli
  }, {x, 49milli, 52milli}, Frame  $\rightarrow$  True, GridLines  $\rightarrow$  Automatic]

```



Out[63]= -Graphics-



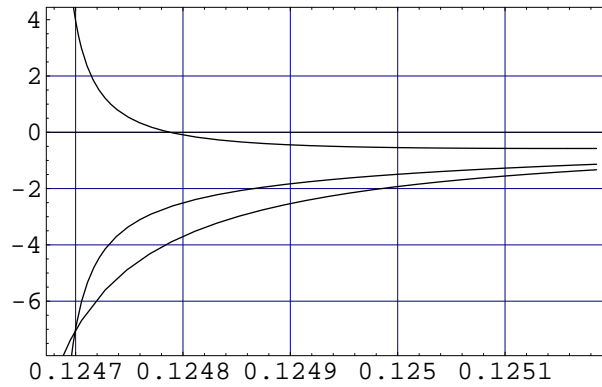
Out[63]= -Graphics-

In[64]:= {tmpcavity, tmppump} = cavitySetM2Tilt[mycavity, mypump, ϕ_3];

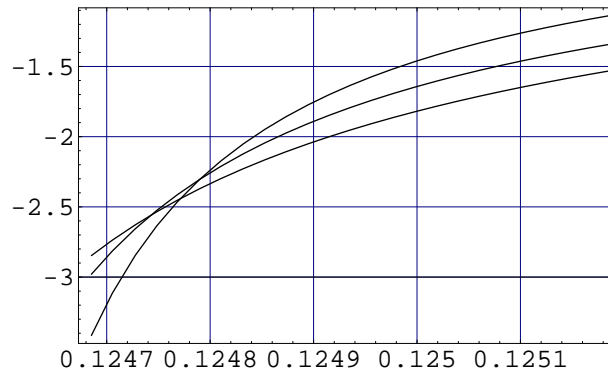
{tmpcavity, tmppump} = cavitySetM3Tilt[tmpcavity, tmppump, ϕ_1]/.
 {d \rightarrow z - x - tmpcavity[[6]]/ Cos[Deg2Rad[tmpcavity[[5]]]],
 fthh \rightarrow ∞ , fthv \rightarrow ∞ };

Plot[
 {
 tSmallSignal1[tmpcavity, tmppump] /. x \rightarrow 49 milli,
 tSmallSignal1[tmpcavity, tmppump] /. x \rightarrow 50 milli,
 tSmallSignal1[tmpcavity, tmppump] /. x \rightarrow 51 milli
 }, {z, z₃, z₃ + 0.5milli}, Frame \rightarrow True, GridLines \rightarrow Automatic]

Plot[
 {
 sSmallSignal1[tmpcavity, tmppump] /. x \rightarrow 49 milli,
 sSmallSignal1[tmpcavity, tmppump] /. x \rightarrow 50 milli,
 sSmallSignal1[tmpcavity, tmppump] /. x \rightarrow 51 milli
 }, {z, z₃, z₃ + 0.5milli}, Frame \rightarrow True, GridLines \rightarrow Automatic]



Out[64]= -Graphics-



Out[64]= -Graphics-

C.3. Scanner model

The scanner model (App. 5) was implemented with the object oriented framework ROOT in C++ (ROOT).

Properties.hh : A header file defining class for calculation of material properties.

```
#ifndef THESIS_PROPERTIES_HH
#define THESIS_PROPERTIES_HH

// Material properties
```

```

class Material
{
public:
    Double_t E;          // Young's modulus
    Double_t G;          // torsion module FIXME NAME
    Double_t kappa;      // compressibility

    Double_t rho;        // density

    Double_t sigma_t;    // tensile stress
    Double_t sigma_c;    // compressive stress
    Double_t tau;        // shear stress
    Double_t sigma_b;    // bending stress

public:
    //
    Material(Double_t p1, Double_t p2, Double_t p3,
             Double_t p4,
             Double_t p5, Double_t p6, Double_t p7, Double_t p8) {
        E = p1; G = p2; kappa = p3;
        rho = p4;
        sigma_t = p5; sigma_c = p6; tau = p7; sigma_b = p8;
    }

    Material(const class Material &m) {
        E = m.E; G = m.G; kappa = m.kappa;
        rho = m.rho;
        sigma_t = m.sigma_t; sigma_c = m.sigma_c; tau = m.tau; sigma_b = m.sigma_b;
    }

public:
    Double_t PoissonRatio();
};

extern const class Material MFusedSilica;
extern const class Material MSteelLow;

// Beam properties (base class)
class Beam
{
public:
    // Types of stress (used to calculate the safety factor, see deflection.cc)
    enum StressType {
        UNDEFINED = 0,
        FIRST = 1,

        BUCKLING = 1,
        TENSILE,
        COMPRESSIVE,
        SHEAR,
        BENDING,

        LAST,
    };
};

public:
    Beam(const Material &mat, Double_t length) : sMaterial(mat), fLength(length) {}
    virtual ~Beam() {}

protected:
    Material sMaterial; // Material definition
    Double_t fLength;   // Beam length

public:
    Material &GetMaterial() { return sMaterial; }
    Double_t GetLength() { return fLength; }
    void SetLength(Double_t l) { fLength = l; }

    virtual Double_t Area(); // Cross section area
    virtual Double_t AreaOfMoment(); // area moment of inertia
    virtual Double_t PolarAreaOfMoment(); // and the respective polar moment of inertia

    virtual Double_t SectionMoment();
    virtual Double_t PolarSectionMoment();

```

```

Double_t GetK(); // "K" (see model)
Double_t GetKprime(); // "K'" (without torque)

Double_t GetTprime(); // "K'" (only torque)

// Material stress factor (see deflection.cc)
Double_t StressFactor(StressType type, Double_t F_or_M);
};

// Implementation for a circular beam
class BeamCircular : public Beam
{
public:
    BeamCircular(const Material &mat, Double_t length) : Beam(mat, length) {}
    BeamCircular(const Material &mat, Double_t length, Double_t r) : Beam(mat,length), fRadius(r) {}
    BeamCircular(const Material &mat, Double_t length, const Double_t r) : Beam(mat,length), fRadius(r) {}
    virtual ~BeamCircular() {}

protected:
    Double_t fRadius;

public:
    void SetRadius(Double_t r) { fRadius = r; }
    Double_t GetRadius() { return fRadius; }

    virtual Double_t Area();

    virtual Double_t AreaOfMoment();
    virtual Double_t PolarAreaOfMoment();

    virtual Double_t SectionMoment();
    virtual Double_t PolarSectionMoment();

    Double_t GetK();
    Double_t GetKprime();

    Double_t GetTprime();

    Double_t StressFactor(StressType type, Double_t F_or_M);
};

#endif // THESIS_PROPERTIES_HH

```

Properties.cc : The source file implementing the interface from Properties.hh.

```

#include "Properties.hh"

Double_t
Material::PoissonRatio()
{
    return E/(2.0*G) - 1.0;
}

const class Material MFusedSilica(
    73e9 /* avg. */, 32e9 /* avg */, 33e-12 /* avg */,
    2205 /* avg */,
    50e6 /* [sci] */, 1100e6 /* [sci] */, 0.0 /* unused */, 4.5e9 /* [Kur] */);

const class Material MSteelLow(
    200e9 /* [Goodfellow] */, 77e9 /* derived w 0.3 poisson ratio */, 0.0 /* unused */,
    792 /* avg */,
    500e6 /* [met90] */, 0.0 /* unused */, 300e6 /* [met90] */, 500e6 /* [met90] */);

/*-----*/
Double_t Beam::Area()
{
    std::cerr << "Wrongly called virtual method (class Beam)" << std::endl;
    return 0.0;
}

```



```

}

Double_t Beam::AreaOfMoment()
{
    std::cerr << "Wrongly called virtual method (class Beam)" << std::endl;
    return 0.0;
}

Double_t Beam::PolarAreaOfMoment()
{
    std::cerr << "Wrongly called virtual method (class Beam)" << std::endl;
    return 0.0;
}

Double_t Beam::SectionMoment()
{
    std::cerr << "Wrongly called virtual method (class Beam)" << std::endl;
    return 0.0;
}

Double_t Beam::PolarSectionMoment()
{
    std::cerr << "Wrongly called virtual method (class Beam)" << std::endl;
    return 0.0;
}

Double_t Beam::GetK()
{
    return 3*sMaterial.E*AreaOfMoment()/TMath::Power(fLength, 3);
}

Double_t Beam::GetKprime()
{
    return 2*sMaterial.E*AreaOfMoment()/TMath::Power(fLength, 2);
}

Double_t Beam::GetTprime()
{
    return sMaterial.G*AreaOfMoment()/TMath::Power(fLength, 2);
}

Double_t Beam::StressFactor(StressType type, Double_t F_or_M)
{
    Double_t EI = sMaterial.E*AreaOfMoment();
    Double_t Lim;

    switch (type) {
    case BUCKLING:
        Lim = 2*TMath::Pi()*TMath::Pi()*EI/TMath::Power(fLength, 2.0);
        std::cerr << "LIMIT=" << 1000*Lim << "mN"
            << std::endl;
        break;
    case TENSILE:
        Lim = sMaterial.sigma_t * Area();
        std::cerr << "LIMIT=" << 1000*Lim << "mN"
            << std::endl;
        break;
    case COMPRESSIVE:
        Lim = sMaterial.sigma_c * Area();
        std::cerr << "LIMIT=" << 1000*Lim << "mN"
            << std::endl;
        break;
    case SHEAR:
        Lim = sMaterial.tau * PolarSectionMoment(); /* FIXME check */
        std::cerr << "LIMIT=" << 1000*Lim << "mNm"
            << std::endl;
        break;
    case BENDING:
        Lim = sMaterial.sigma_b * SectionMoment();
        std::cerr << "LIMIT=" << 1000*Lim << "mNm"
            << std::endl;
        break;
    }
}

```

```

        if (Lim)
            return TMath::Abs(F_or_M)/Lim;
        else
            return -1.0;
    }

    /*-----*/
    Double_t BeamCircular::Area()
    {
        return TMath::Pi()*TMath::Power(fRadius,2);
    }

    Double_t BeamCircular::AreaOfMoment()
    {
        return TMath::Pi()*TMath::Power(fRadius,4)/4;
    }

    Double_t BeamCircular::PolarAreaOfMoment()
    {
        return 2*AreaOfMoment();
    }

    Double_t BeamCircular::SectionMoment()
    {
        return 2*AreaOfMoment()/fRadius;
    }

    Double_t BeamCircular::PolarSectionMoment()
    {
        return 2*PolarAreaOfMoment()/fRadius;
    }

    Double_t BeamCircular::GetK()
    {
        return 3*sMaterial.E*AreaOfMoment()/TMath::Power(fLength, 3);
    }

    Double_t BeamCircular::GetKprime()
    {
        return 2*sMaterial.E*AreaOfMoment()/TMath::Power(fLength, 2);
    }

    Double_t BeamCircular::GetTprime()
    {
        return sMaterial.G*AreaOfMoment()/TMath::Power(fLength, 2);
    }

    Double_t BeamCircular::StressFactor(StressType type, Double_t F_or_M)
    {
        Double_t EI = sMaterial.E*AreaOfMoment();
        Double_t Lim;

        switch (type) {
            case BUCKLING:
                Lim = 2*TMath::Pi()*TMath::Pi()*EI/TMath::Power(fLength, 2.0);
                break;
            case TENSILE:
                Lim = sMaterial.sigma_t * Area();
                break;
            case COMPRESSIVE:
                Lim = sMaterial.sigma_c * Area();
                break;
            case SHEAR:
                Lim = sMaterial.tau * PolarSectionMoment(); /* FIXME check */
                break;
            case BENDING:
                Lim = sMaterial.sigma_b * SectionMoment();
                break;
        }

        if (Lim)
            return TMath::Abs(F_or_M)/Lim;
        else
            return -1.0;
    }

```

```
}
```

deflection.cc : The implementation of the model of the scanner.

```
#include "Properties.hh"
#include "Properties.cc"

// Definition of the piezo bending element by its properties
class Piezo
{
public:
    static Double_t c_e;
    static Double_t c_EI;

    Double_t W;
    Double_t L;

public:
    Piezo(Double_t width, Double_t length) : W(width), L(length) {}
};

// We only have a single type of piezo bending elements, therefore it's static
Double_t Piezo::c_e = 0.01;
Double_t Piezo::c_EI = 1.0;

// Calculation of the deflection of the fiber
// Additionally, the safety factor (which is the relation of the stress
// to the minimal material strength (either tensile, bending or buckling strength)
Double_t Deflection(Double_t &safety,           // Return value of the safety factor
                    Double_t L_f,              // Free fiber length
                    BeamCircular &exc,         // Excitation fiber properties
                    Double_t coupling,         // Coupling (of the glue point connecting
                                                // the fibers
                    BeamCircular &sus,         // Suspension
                    Double_t ignore,          // Flag to ignore properties of suspension completely
                    Double_t U,               // Voltage
                    Piezo &pzo                // Piezo element definition
                    )
{
    // Temporary variables (anchor distance and suspension length)
    Double_t l_f = exc.GetLength();
    Double_t l_s = sus.GetLength();

    // Calculate factors according to the model
    Double_t K_U = pzo.c_e/pzo.c_EI * pzo.W / pzo.L;
    Double_t K_a = 1/pzo.c_EI * pzo.W / TMath::Power(pzo.L, 3.0);

    Double_t K_f = exc.GetK();
    Double_t Kp_f = exc.GetKprime();

    Double_t K_s = sus.GetK()*ignore;
    Double_t Kp_s = (2*sus.GetKprime() + sus.GetTprime())*ignore;

    Double_t xi = (Kp_f+4*Kp_s*l_s/l_f * coupling)/(Kp_f+2*Kp_s*l_s/l_f * coupling);

    // calculate deflection and slope according to the model
    Double_t s = U*2*K_U/( K_f*xi + (2+2*coupling)*K_s + 2*K_a);
    Double_t sp = s / ( (Kp_f/K_f + 2*l_s/l_f*Kp_s/K_f) );

    // Initialize safety
    safety = 0.0;

    Double_t stmp;

    // Actuator force
    Double_t Fa = U*K_U-s*K_a;

    // Check stress
    Int_t type = Beam::UNDEFINED;
    if ((stmp = sus.StressFactor(Beam::BUCKLING, Fa)) > safety) { safety = stmp; type = Beam::BUCKLING; }
```

```
if ((stmp = sus.StressFactor(Beam::TENSILE, Fa)) > safety) { safety = stmp; type = Beam::TENSILE; }
if ((stmp = sus.StressFactor(Beam::COMPRESSIVE, Fa)) > safety) { safety = stmp; type = Beam::COMPRESSIVE; }

Double_t M = -sp*l_s*4*Kp_s;
if ((stmp = sus.StressFactor(Beam::BENDING, M)) > safety) { safety = stmp; type = Beam::BENDING; }

// Done.
return sp*L_f+s;
};
```

Bibliography

Das Manifest. *Gehirn & Geist*, 2004. <http://www.gehirnundgeist.de/manifest>.

Handbook of Optics, 2 edition, 1995.

Govind P. Agrawal. *Nonlinear Fiber Optics*. Optics and Photonics. Academic Press, 2 edition, 1995.

A.D. Aguirre, P. Hsiung, T.H. Ko, I. Hartl, and J.G. Fujimoto. High-resolution optical coherence microscopy for high-speed, in vivo cellular imaging. *Optics Letters*, 28(21):2064–2066, 2003.

J. Alda, S. M. Wang, and E. Bernabeu. Analytical expression for the complex radius of curvature tensor-q for generalized gaussian beams. *Optics Communications*, 80(5-6):350–352, 1991.

A. Bartels and H. Kurz. Generation of a broadband continuum by a Ti : sapphire femtosecond oscillator with a 1-GHz repetition rate. *Optics Letters*, 27(20):1839 – 1841, OCT 15 2002.

A. Bartels, T. Dekorsy, and H. Kurz. Femtosecond Ti : sapphire ring laser with a 2-GHz repetition rate and its application in time-resolved spectroscopy. *Optics Letters*, 24(14):996 – 998, JUL 15 1999.

M. J. Bastiaans. Abcd law for partially coherent gaussian light, propagating through 1st-order optical-systems. *Optical and Quantum Electronics*, 24(9): S1011–S1019, 1992.

T. Brabec, C. Spielmann, and F. Krausz. Mode locking in solitary lasers. *Optics Letters*, 16(24):1961–1963, 1991.

T. Brabec, C. Spielmann, and F. Krausz. Limits of pulse shortening in solitary lasers. *Optics Letters*, 17(10):748–750, 1992.

- L. Brand, C. Eggeling, C. Zander, K.H. Drexhage, and C.A.M. Seidel. Single-molecule identification of Coumarin-120 by time-resolved fluorescence detection: Comparison of one- and two-photon excitation in solution. *Journal of Physical Chemistry A*, 101(24):4313 – 4321, JUN 12 1997.
- A. Budó. *Theoretische Mechanik*, volume 25 of *Hochschulbücher für Physik*. Deutscher Verlag der Wissenschaft, 12 edition, 1990.
- Z. Cheng, F. Krausz, and C. Spielmann. Compression of 2 mj kilohertz laser pulses to 17.5 fs by pairing double-prism compressor: analysis and performance. *Optics Communications*, 201(1-3):145–155, 2002.
- R. H. Christie, W. R. Zipfel, R. M. Williams, W. W. Webb, and B. T. Hyman. In vivo multiphoton imaging of amyloid deposition in transgenic mice. *The Journal of Neuroscience*, 58(5):560–560, 1999.
- S.W. Clark, F.Ö. Illday, and F.W. Wise. Fiber delivery of femtosecond pulses from a ti:sapphire laser. *Optics Letters*, 26(17):1320–1322, 2001.
- Nathalie Cotillon-Williams and Jean-Marc Edeline. Evoked oscillations in the thalamo-cortical auditory system are present in anesthetized but not in unanesthetized rats. *Journal of Neurophysiology*, 89:1968–1984, 2003.
- Handbook of Chemistry and Physics*. CRC Press, 84 edition, 2003–2004.
- W. Denk, J. H. Strickler, and W. W. Webb. 2-photon laser scanning fluorescence microscopy. 248(4951):73–76, 1990.
- W. Denk, K. R. Delaney, A. Gelperin, D. Kleinfeld, B. W. Strowbridge, D. W. Tank, and R. Yuste. Anatomical and functional imaging of neurons using 2-photon laser-scanning microscopy. 54(2):151–162, 1994.
- W. Denk, D.W. Piston, and W.W. Webb. *Handbook for biophysical imaging and optoelectronics*, chapter Two-Photon Molecular Excitation in Laser-Scanning Microscopy. Plenum Press, New York, 1995.
- P.S. Dittrich and P. Schwille. Photobleaching and stabilization of fluorophores used for single-molecule analysis with one- and two-photon excitation. *Applied Physics B-Lasers and Optics*, 73:829–837, 2001.

- F. J. Duarte. Generalized multiple-prism dispersion theory for pulse-compression in ultrafast dye-lasers (vol 19, pg 223, 1987). *Optical And Quantum Electronics*, 27(2):134–134, 1995.
- F. J. Duarte. Multiple-prism arrays in laser optics. *American Journal of Physics*, 68(2):162–166, 2000a.
- F. J. Duarte. Comment on "analytical expressions of group-delay dispersion and cubic phase for four-prism sequence used at other than brewster's angle. *Optics And Laser Technology*, 32(3):211–211, 2000b.
- C. Eggeling, J. Widengren, R. Rigler, and C.A.M. Seidel. Photobleaching of fluorescent dyes under conditions used for single-molecule detection: Evidence of two-step photolysis. *Analytical Chemistry*, 70(13):2651 – 2659, JUL 1 1998.
- Mauro Fà, Gaimpaolo Mereu, Veronica Ghiglieri, Alessandra Meloni, Paola Salis, and Gian Luigi Gessa. Electrophysiological and pharmacological characteristics of nigral dopaminergic neurons in the conscious head-restrained rat. *Synapse*, 48:1–9, 2003.
- Marcus Feierabend. *Coherence-gated wave-front sensing in strongly scattering samples*. PhD thesis, Univ. of Heidelberg, Germany, 2004.
- B. H. Gähwiler, M. Capogna, D. Debanne, R. A. McKinney, and S. M. Thompson. Organotypic slice cultures: a technique has come of age. *Trends In Neurosciences*, 20(10):471–477, 1997.
- S. Gatz and J. Hermann. Geometrical threshold zones and gaussian modes in lasers with radially varying gain. *Optics Letters*, 19(21):1696–1698, 1994.
- Maria Göppert-Mayer. *Über Elementarakte mit zwei Quantensprüngen*. Göttinger dissertation, John Hopkins University, 7 December 1930.
- J. P. Gordon and R. L. Fork. Optical-resonator with negative dispersion. *Optics Letters*, 9(5):153–155, 1984.
- M. Gumbleton and D. J. Stephens. Coming out of the dark: the evolving role of fluorescence imaging in drug delivery research. *Advanced Drug Delivery Reviews*, 57(1):5–15, 2005.

- F. Helmchen. Miniaturization of fluorescence microscopes using fibre optics. *Experimental Physiology*, 87(6):737–745, 2002.
- F. Helmchen and W. Denk. New developments in multiphoton microscopy. 12(5):593–601, 2002.
- F. Helmchen and J. Waters. Ca^{2+} imaging in the mammalian brain in vivo. *Eur J Pharmacol*, 447(2-3):119–29, 2002.
- F. Helmchen, M.S. Fee, D.W. Tank, and W. Denk. A two-photon fiber-scanning microscope for cortical imaging in awake, behaving rodents. *Biophysical Journal*, 78(1):2625, 2000.
- F. Helmchen, M.S. Fee, D.W. Tank, and W. Denk. A miniature head-mounted two-photon microscope. high-resolution brain imaging in freely moving animals. *Neuron*, 31(6):903–12, 2001.
- F. Helmchen, D.W. Tank, and W. Denk. Enhanced two-photon excitation through optical fiber by single-mode propagation in a large core. *Appl Opt*, 41(15):2930–4, 2002.
- D. Huang, M. Ulman, L.H. Acioli, H.A. Haus, and J.G. Fujimoto. Self-focusing-induced saturable loss for laser mode-locking. *Optics Letters*, 17(7):511 – 513, APR 1 1992.
- J. C. Jung, A. D. Mehta, E. Aksay, R. Stepnoski, and M. J. Schnitzer. In vivo mammalian brain imaging using one- and two-photon fluorescence microendoscopy. *J Neurophysiol*, 92(5):3121–33, 2004.
- W. Kaiser and C. Garret. Two-photon excitation in $\text{CaF}_2:\text{Eu}^{2+}$. *Physical Review Letters*, 7:229–231, 1961.
- V. L. Kalashnikov, V. P. Kalosha, V. P. Mikhailov, and I. G. Poloyko. Self-mode locking of 4-mirror-cavity solid-state lasers by Kerr self-focusing. *Journal of the Optical Society of America B-Optical Physics*, 12(3):462–467, 1995.
- D. M. Kane. Ti-sapphire laser cavity mode and pump-laser mode calculations. *Applied Optics*, 33(18):3849–3856, 1994.
- J. Knittel, L. Schnieder, G. Buess, B. Messerschmidt, and T. Possner. Endoscope-compatible confocal microscope using a gradient index-lens system. *Optics Communications*, 188:265–273, 2001.

- H. Kogelnik. On the propagation of gaussian beams of light through lenslike media includeing those with a loss or gain variation. *Applied Optics*, 4(12): 1562–1569, 1965.
- F. Kroupa and K. Nejezchleb. Bending of piezo-electric actuators. *Ceramics - Silikaty*, 42(1):29–38, 1998.
- Jouko Kurki. Basic properties of optical fibers. <http://opetus.stadia.fi/kurki/Courses/OpticalTransmissionSystems/fibbas.pdf>.
- B. E. Lemoff and C. P. J. Barty. Generation of high-peak-power 20-fs pulses from a regeneratively initiated, self-mode-locked ti-sapphire laser. *Optics Letters*, 17(19):1367–1369, 1992.
- C.W. Lim, L.H. He, and A.K. Soh. Three-dimensional electromechanical responses of a parallel piezoelectric bimorph. *International Journal of Solids and Structures*, 38:2833–2849, 2001.
- K.H. Lin, Y. Lai, and W.F. Hsieh. Simple analytical method of cavity design for astigmatism-compensated kerr-lens mode-locked ring lasers and its applications. *Journal of the Optical Society of America B-Optical Physics*, 12(3):368, 1995.
- J. Lippman and A. Dunaevsky. Dendritic spine morphogenesis and plasticity. *Journal of Neurobiology*, 64(1):47, 2005.
- B. D. Lu, G. Y. Feng, and B. W. Cai. Complex ray representation of the astigmatic gaussian-beam propagation. *Optical and Quantum Electronics*, 25(4):275–284, 1993.
- Amy L. Lytle, Erez Gershgoren, Ra’anan I. Tobey, Margaret M. Murnane, Henry C. Kapteyn, and Dirk Müller. Use of a simple cavity geometry for low and high repetition rate modelocked ti:sapphire lasers. *Optics Express*, 12(7):1409–1416, 2004.
- V. Magni, G. Cerullo, and S. Desilvestri. Closed-form gaussian-beam analysis of resonators containing a kerr medium for femtosecond lasers. *Optics Communications*, 101(5-6):365–370, 1993a.
- V. Magni, G. Cerullo, and S. Desilvestri. Abcd matrix analysis of propagation of gaussian beams through kerr media. *Optics Communications*, 96(4-6): 348–355, 1993b.

- V. Magni, G. Cerullo, S. De Silvestri, and A. Monguzzi. Astigmatism in gaussian-beam self-focusing and in resonators for kerr-lens mode locking. *JOSA-B*, 12(3):476, 1995.
- A. Marcano and I. Urdaneta. Fluorescence quantum yield of rhodamine 101 in the presence of absorption saturation. *Applied Physics B-Lasers and Optics*, 72(2):207 – 213, JAN 2001.
- A. May, R. Jakobs, C. Ell, and J. F. Riemann. New endoscopic treatment methods. *Internist*, 42(4):494–+, 2001.
- A. D. Mehta, J. C. Jung, B. A. Flusberg, and M. J. Schnitzer. Fiber optic in vivo imaging in the mammalian nervous system. *Current Opinion in Neurobiology*, 14(5):617–628, 2004.
- Metall [1990]. *Tabellenbuch Metall*, 1990.
- U. Michel, I. Malik, S. Ebert, M. Bähr, and S. Kügler. Long-term in vivo and in vitro aav-2-mediated rns interference in rat ganglion cells and cultured primary neurons. *Biochemical and Biophysical Research Communications*, 326: 307–312, 2005.
- M.U. Müller. CfNt. Max-Planck-Institute for medical Research, 2000-2005. Microscope control software.
- W. Nasalski. Complex ray-tracing of nonlinear propagation. *Optics Communications*, 119(1-2):218–226, 1995.
- K. Ohki, S. Chung, Y.H. Ch’ng, P. Kara, and R.C. Reid. Functional imaging with cellular resolution reveals precise micro-architecture in visual cortex. *Nature*, 433(7026):597–603, 2005.
- D. Onciul. Abcd propagation law for misaligned general astigmatic gaussian beams. *Journal of Optics-Nouvelle Revue D Optique*, 23(4):163–165, 1992.
- G.H. Patterson and D.W. Piston. Photobleaching in two-photon excitation microscopy. *Biophys J*, 78(4):2159–62, 2000.
- P. Poirazi and B. W. Mel. Towards the memory capacity of neurons with active dendrites. *Neurocomputing*, 26-7:237–245, 1999.
- M. A. Porras, J. Alda, and E. Bernabeu. Gaussian beams passing through apertured abcd optical-systems. *Optik*, 94(1):23–32, 1993.

- B. Proctor and F. Wise. Quartz prism sequence for reduction of cubic phase in a mode-locked TiAl_2O_3 laser. *Optics Letters*, 17(18):1295–1297, 1992.
- B. Proctor and F. Wise. Generation of 13-fs pulses from a mode-locked TiAl_2O_3 laser with reduced 3rd-order dispersion. *Applied Physics Letters*, 62(5):470–472, 1993.
- ROOT. <http://root.cern.ch>. An Object Oriented Data Analysis Framework.
- B. Sakmann and E. Neher. Patch clamp techniques for studying ionic channels in excitable membranes. *Annual Review of Physiology*, 46:455–472, 1984.
- F. Salin, J. Squier, and M. Piché. Mode-locking of TiAl_2O_3 lasers and self-focusing - a gaussian approximation. *Optics Letters*, 16(21):1674–1676, 1991.
- P. Schwille, U. Haupts, S. Maiti, and W.W. Webb. Molecular dynamics in living cells observed by fluorescence correlation spectroscopy with one- and two-photon excitation. *Biophys J*, 77(4):2251–65, 1999.
- P. Selinger. potrace. <http://potrace.sourceforge.net>, v1.7. Transforms bitmaps into vector graphics.
- R. E. Sherriff. Analytic expressions for group-delay dispersion and cubic dispersion in arbitrary prism sequences. *Journal of the Optical Society of America B-Optical Physics*, 15(3):1224–1230, 1998.
- Anthony E. Siegman. *Lasers*. University Science Books, Mill Valley, California, 1986.
- L. Stoppini, P. A. Buchs, and D. Muller. A simple method for organotypic cultures of nervous-tissue. *Journal Of Neuroscience Methods*, 37(2):173–182, 1991.
- C. Stosiek, O. Garaschuk, K. Holthoff, and A. Konnerth. In vivo two-photon calcium imaging of neuronal networks. *PNAS*, 100(12):7319–7324, 2003.
- K. Svoboda, W. Denk, D. Kleinfeld, and D. Tank. In vivo dendritic calcium dynamics in neocortical pyramidal neurons. *Nature*, 385(6612):161–165, 1997.

- Y. P. Tan, I. Llano, A. Hopt, F. Wurriehausen, and E. Neher. Fast scanning and efficient photodetection in a simple two-photon microscope. 92(1-2): 123–135, 1999.
- T. Tari and P. Richter. Correction of astigmatism and ellipticity of an astigmatic gaussian laser-beam by symmetrical lenses. *Optical and Quantum Electronics*, 24(9):S865–S872, 1992.
- P. Theer, M.T. Hasan, and W. Denk. Two-photon imaging to a depth of 1000 μm in living brains by use of a Ti : Al₂O₃ regenerative amplifier. *Optics Letters*, 28(12):1022 – 1024, JUN 15 2003.
- Gillian M. Tozer, Simon M. Ameer-Beg, Jennifer Baker, Paul R. Barber, Sally A. Hill, Richard J. Hodgkiss, Rosalind Locke, Vivien E. Prise, Ian Wilson, and Borivoj Vojnovic. Intravital imaging of tumour vascular networks using multi-photon fluorescence microscopy. *Advanced Drug Delivery Reviews*, 57(1):135, 2005.
- J. Tritthardt. Entwicklung der Aufnahmeelektronik eines Laser-Scanning-Mikroskops. Master’s thesis, FernUniversität in Hagen, 2005.
- R. Truner and T. Jones. Techniques for imaging neuroscience. *British Medical Bulletin*, 65(3):3–20, 2003.
- K. Vedam. The elastic and photoelastic constants of fused quartz. *Phys. Rev.*, 78:472–473, 1950.
- Del Mar Ventures. <http://www.sciner.com/Opticsland/FS.htm>.
- Wei Hua Wang, Ping Wen, Li Min Wang, Yong Zhang, Ming Xiang Pan, De Qian Zhao, and Ru Ju Wang. Equation of state of bulk metallic glasses studied by an ultrasonic method. *Applied Physics Letters*, 79(24), 2001.
- J. Waters, M. Larkum, B. Sakmann, and F. Helmchen. Supralinear Ca^{2+} influx into dendritic tufts of layer 2/3 neocortical pyramidal neurons in vitro and in vivo. *Journal of Neuroscience*, 23(224):8558–8567, 2003.
- T. Xie, H. Xie, G. K. Fedder, and Y. Pan. Endoscopic optical coherence tomography with a modified microelectromechanical systems mirror for detection of bladder cancers. *Applied Optics*, 42(31):6422, 2003.

- C. Xu, W. Zipfel, J.B. Shear, R.M. Williams, and W.W. Webb. Multiphoton fluorescence excitation: New spectral windows for biological nonlinear microscopy. *Proc. Natl. Acad. Sci. USA*, 93:10763–10768, 1996.
- Chris Xu and Watt W. Webb. Measurement of two-photon excitation cross sections of molecular fluophores with data from 690 to 1050nm. *J. Opt. Soc. Am. B*, 13(3):481ff., March 1996.
- R. Yuste and D.W. Tank. Dendritic integration in mammalian neurons, a century after cajal. *Neuron*, 16:701, 1996.
- Ruobing Zhang, Jing Ma, Dongqing Pang, Jinghua Sun, and Qingyue Wang. Spatial chirp and angular dispersion of laser crystal for a four-mirror cavity kerr-lens mode-locked laser. *Applied Optics*, 43(10):2184, 2004.
- D. M. Zhao, Q. Lin, and S. M. Wang. Symmetrizing transformation of general astigmatic gaussian beams. *Optical and Quantum Electronics*, 26(9):903–910, 1994.